WARSAW UNIVERSITY
OF TECHNOLOGY

**Faculty of Electronics
and Information Technology**

Ph.D THESIS

Bartłomiej Salski, M.Sc.

**Application of semi-analytical algorithms
in the finite-difference time-domain modeling
of electromagnetic radiation and scattering problems**

Supervisor
Professor Wojciech Gwarek, Ph.D., D.Sc.

Warsaw, 2010

Abstract

This dissertation is focused on the semi-analytical finite-difference time-domain (FDTD) modeling of electromagnetic radiation and scattering problems. A combination of analytical and numerical methods may lead to decreased computational effort at no cost to the accuracy of the obtained results.

Chapter 3 deals with electromagnetic modeling of periodic structures using the FDTD method supplemented with periodic boundary conditions, derived from the analytical Floquet theorem. A developed algorithm is then applied to the analysis of one-, two-, and three-dimensional eigenvalue problems of periodic structures. As an extension of the algorithm's applicability to deterministic problems, methods and computational models for the analysis of a diffraction of plane wave obliquely incident on periodic structure are introduced and investigated. For the purpose of final evaluation of the introduced methods, models with a Gaussian beam incident on a periodic structure are introduced and validated.

Chapter 4 of this dissertation depicts the author's consideration on the possibility of applying the FDTD method to the modeling of imaging phenomenon, which is widely used in optical microscopes. A coupling of the FDTD method with the algorithms based on approximate methods dedicated to optical diffraction modeling is introduced and validated. The elaborated method leads to increased accuracy of the overall modeling of an optical path in modern microscopes.

Chapter 5 is focused on the transformation of electromagnetic fields in a near zone of axisymmetrical structures. The method introduced and derived by the author of this dissertation enables a significant reduction in computational effort of the already existing FDTD schemes for axisymmetrical problems which have no common symmetry axis for all the consituent elements, such as off-axis feeded Cassegrain antenna.

Streszczenie

Praca poświęcona jest częściowo analitycznemu modelowaniu elektromagnetycznemu zagadnień promieniowania oraz dyfrakcji fali elektromagnetycznej metodą różnic skończonych w dziedzinie czasu (ang. finite-difference time-domain). Kombinacja metod analitycznych z metodami numerycznymi może prowadzić do zmniejszenia nakładów obliczeniowych bez dodatkowych kosztów w postaci zmniejszonej dokładności otrzymywanych wyników obliczeń.

Rozdział 3 rozprawy dotyczy modelowania elektromagnetycznego struktur periodycznych metodą różnic skończonych w dziedzinie czasu, uzupełnioną o periodyczne warunki brzegowe wyprowadzone z analitycznego twierdzenia Floquet'a. Algorytm ten zastosowany jest następnie do analizy problemów własnych jedno-, dwu- oraz trójwymiarowych struktur periodycznych. W ramach problemów deterministycznych, wprowadzone i opisane są także metody i modele obliczeniowe dyfrakcji fali płaskiej padającej pod dowolnym kątem na strukturę periodyczną. W celu weryfikacji opisanych dotychczas metod, wprowadzone zostają modele do obliczeń padania fali elektromagnetycznej o przestrzennym rozkładzie Gaussa na strukturę periodyczną.

Rozdział 4 rozprawy przedstawia rozważania autora na temat możliwości zastosowania metody różnic skończonych w dziedzinie czasu do modelowania zjawiska obrazowania, szeroko stosowanego w mikroskopach optycznych. Zaproponowana i zweryfikowana została możliwość sprzężenia metody różnic skończonych w dziedzinie czasu z algorytmem opartym na aproksymacyjnych metodach modelowania dyfrakcji optycznej. Opracowana metoda pozwala na zwiększenie dokładności modelowania toru optycznego we współczesnych mikroskopach.

Rozdział 5 poświęcony jest przekształceniu pola elektromagnetycznego w strefie bliskiej dla problemów osiowosymetrycznych. Metoda - wyprowadzona i zweryfikowana przez autora pracy - pozwala na znaczne zwiększenie efektywności obliczeń elektromagnetycznych struktur osiowosymetrycznych, takich jak antena typu Cassegrain, której poszczególne elementy nie posiadają wspólnej osi symetrii.

Acknowledgments

I would like to express my sincere gratitude and appreciation to Professor Wojciech Gwarek for his continuing support and valuable advice during these over four years of my studies toward this dissertation. It has been an excellent opportunity for me to gain experience in computational electromagnetics, which I will always be grateful for.

This dissertation would not come into existence without the advisory role of Dr. Malgorzata Celuch, and numerous scientific conversations we had throughout my research studies. I really appreciate this support and wish to thank for all the fruitful comments.

Contents

List of Figures

List of Tables

List of Publications

Magazines

[1]. B.Salski, W.K.Gwarek, "Near-to-Near Transformation in axisymmetrical antenna problems", IEEE Trans. Antenna Propagat., vol.55, No.8, Aug.2007, pp.2157-2162.

[2]. B. Salski, W. Gwarek, M. Celuch, ”Electromagnetic FDTD modeling of optical problems,” *Elektronika – konstrukcje, technologie, zastosowania*, no. 4, pp. 53-55, 2009.

[3]. B. Salski and W. K. Gwarek, "Hybrid finite-difference time-domain Fresnel modeling of microscopy imaging", *Applied Optics*, vol. 48, issue 11, pp. 2133-2138, 2009.

[4]. B. Salski, M. Celuch, W. Gwarek, ”FDTD for nanoscale and optical problems,” *Microwave Magazine*, accepted for publication, April, 2010.

Conferences

[1]. J.Antoniuk, B.Salski, W.K.Gwarek, "Slotted waveguide as excitation systems of microwave ovens", 12th Conf. on Microwave Technique COMITE-2003, Pardubice, the Czech Republic, Sept.2003, pp.85-88.

[2]. P.Kopyt, B.Salski, W.K.Gwarek, "Resonator-based method for estimation of complex permittivity of materials", 12th Conf. on Microwave Technique COMITE-2003, Pardubice, the Czech Republic, Sept.2003, pp.117-120.

[3]. B.Salski, M.Celuch, W.K.Gwarek, "Evaluation of FDTD regimes for scattering from periodic structures", 23rd Annual Review of Progress in Applied Computational Electromagnetics, Verona, March 2007, pp.1815-1822.

[4]. B.Salski, W.K.Gwarek, M.Celuch, "Comparison of FDTD excitation models for scatterometry of periodic reticles", 2007 IEEE AP-S Intl.Symp., Honolulu, June 2007, pp. 1673-1676.

[5]. B.Salski, M.Celuch, W.Gwarek, "Enhancements to FDTD modeling for optical metrology applications", SPIE Optical metrology - 18th Intl. Congress on Photonics in Europe, Munich, June 2007.

[6]. D.Kandel, M.Adel, B.Dinu, B.Golovanevsky, P.Izikson, V.Levinski, I.Vakshtein, P.Leray, M.Vasconi, B.Salski, "Differential signal scatterometry overlay metrology: an accuracy investigation", *Optical Measurement Systems for Industrial Inspection V, Proceedings of SPIE*, vol. 6616, 2007.

[7]. B.Salski, M.Celuch, W.K. Gwarek, "Review of Complex Looped FDTD and its new applications", 24th Annual Review of Progress in Applied Computational Electromagnetics, Niagara Falls, March - April 2008.

[8]. P. Leray, S. Cheng, D. Kandel, M. Adel, A. Marchelli, I. Vakshtein, M. Vasconi and B. Salski, "Diffraction based overlay metrology: accuracy and performance on front end stack", *Metrology, Inspection, and Process Control for Microlithography XXII, Proceedings of SPIE*, vol. 6922, 2008.

[9]. B. Salski, M. Celuch, W. Gwarek, "FDTD modelling of finite spot scatterometry", 17th International Conference on Microwaves, Radar and Wireless Communications: MIKON 2008, Wroclaw, May 2008.

[10]. B. Salski and W. K. Gwarek, "Hybrid FDTD-Fresnel Modeling of Microscope Imaging", to be presented at the International Conference on *Recent Advances in Microwave Theory and Applications* MICROWAVE-08 in Jaipur, Rajastan, India, November 21-24, 2008.

[11]. B. Salski and W. K. Gwarek, "Hybrid FDTD-Fresnel modeling of the scanning confocal microscopy", *Proceedings of SPIE Scanning Microscopy 2009*, vol. 7378, 2009.

[12]. P. Leray, S. Cheng, D. Laidler, D. Kandel, M. Adel, B. Dinu, M. Polli, M. Vasconi, B. Salski, "Overlay metrology for double patterning processes," *Metrology, Inspection, and Process Control for Microlithography XXIII, Proceedings of SPIE*, vol. 7272, 2009.

[13]. B. Salski, M. Celuch, W. Gwarek, "Electromagnetic simulations of periodic structures with FDTD tools," *Progress in Electromagnetic Research Symposium*, Moscow, Aug. 2009.

Symbols

E	electric field
H	magnetic field
D	electric flux denisty
B	magnetic flux density
J	electric current density
ε_0	free-space permittivity
μ_0	free-space permeability
ρ	electric charge density
c	electromagnetic wave velocity in a free-space
I	electric current
K	magnetic current
A	vector potential
γ	propagation constant
α	attenuation constant
β	phase constant
β_f	longitudinal phase constant
η	intrinsic impedance of vacuum
k	propagation vector
ψ	Floquet phase shift per period
λ	wavelength
f	frequency
ε_{eff}	effective permittivity
w_0	Gaussian beam spot radius
j	square root of –1 (notation common in electronics)
i	square root of –1 (notation common in physics)
$\mathfrak{I}$	Fourier transform

Acronyms and abbreviations

CAD	computer aided design
R&D	research and development
EM	electromagnetic
FDTD	finite-difference time-domain
FEM	finite element method
MoM	method of moments
CL-FDTD	complex-looped FDTD
NTN	near-to-near
PBC	perodic boundary conditions
1D	one-dimensional
2D	two-dimensional
3D	three-dimensional
V2D	vector 2D
ABC	absorbing boundary
PML	perfectly matching layer
TEM	transverse electromagnetic
TF	total field
SF	scattered field
NTF	near to far
BOR	body of revolution
TE	transverse electric
TM	transverse magnetic
ASM	array scanning method
PEC	perfect electric conductor
PMC	perfect magnetic conductor
PBG	photonic bandgap
GaAs	Gallium Arsenide
IC	integrated circuit
LSI	large scale integration
FSS	frequency selective structure
FETD	FEM time domain

RCWA	rigorous coupled wave analysis
AOI	angle of incidence
PLW	plane wave
DFT	direct Fourier transform
FFT	fast Fourier transform
ASP	angular scattering pattern
SNR	signal to noise ratio
CD	critical dimension
GBW	Gaussian beam wall
NA	numerical aperture
PSF	point spread function
FWHM	full width at half maximum
DOF	depth of field
bcc	body centered cubic
fcc	face centered cubic
WG	waveguide

Chapter 1

Introduction

1.1 Motivation and Objectives

During the last several years computer aided design (CAD) has become an essential tool in the engineering practice as well as in the research and development (R&D) activities. It is hard to imagine a professional design work without specialized software applications supported with modern computing units. It is mainly an outcome of dynamic growth that can be observed in many branches of science, but also a result of an increasing complexity of modern devices. Old-fashioned cut-and-try techniques were found highly ineffective, so in the recent years a lot of effort has been focused on the development of numerical methods and algorithms to apply in various scientific disciplines.

The subject of this thesis concerns CAD modeling of electromagnetic (EM) phenomena. In particular, the dissertation is focused on one of the most recognized numerical methods in electromagnetics, namely the finite-difference time-domain (FDTD) method, originally introduced in electromagnetics by Kane Yee in 1966. Some details about the FDTD method will be recalled in Chapter 2. It should be emphasized, however, that an increasing confidence in EM modeling stimulates growing market requirements, which are often beyond computational capabilities of the state-of-the-art computer platforms. In consequence, a lot of effort is continuously undertaken by many scientists to solve or at least alleviate that mismatch. One of the possible solutions to the huge demand of computational speed and effectiveness lies in investing in more powerful processing units. On the other hand, there can be observed an increasing popularity of hybrid EM modeling, which combines different modeling methods, enabling a reduction in computational effort for specific EM problems. Some of these approaches may be called partially analytical, in reference to the algorithms that combine classical numerical methods, like FDTD, FEM, MoM, etc., with analytical formulae. This dissertation addresses some of partially analytical methods coupled with the FDTD method.

The motivation of this thesis follows from the demand to extend the applicability of the FDTD method to the analysis of radiation and scattering problems, which were formerly highly ineffective, or even impossible to handle without deterioration of accuracy. The following thesis is posed and will be proven:

> **The partially analytical FDTD methods can substantially speed up the computation of electromagnetic radiation and scattering problems without deterioration of accuracy.**

In this dissertation, three auxiliary statements will also be addressed and confirmed:

1. **Electromagnetic modeling of plane wave scattering from periodic structures can be made computationally more effective by applying FDTD with Floquet theorem (CL-FDTD) and a number of specialized models for excitation and parameter extraction.**

2. **Approximate optical modeling of lens imaging systems based on a Fresnel diffraction theory can be successfully supported with the rigorous FDTD modeling, improving modeling accuracy.**

3. **The alternative partially analytical method of near-to-near field transformation for axisymmetrical problems, requiring less computational efforts than the direct integration technique, can be developed.**

The study presented in this dissertation extends computational capabilities of the FDTD method for new domains of problems, introducing simplified computational models based on analytical transformations or approximate assumptions.

1.2 Thesis Overview

Chapter 2 presents a brief outline of the FDTD method, emphasizing its major advantages over the other modeling methods, but also pointing out its inherent limitations.

Chapter 3 covers the issue of the FDTD modeling of periodic structures. Implementation of 1D, 2D and 3D periodic boundary conditions (PBC) is presented and its applicability for analysis of eigen-problems is studied. Next, modeling of a plane wave scattering from periodic structures using the FDTD algorithm with PBC is investigated. A near-to-far transformation is adapted in the periodic FDTD algorithm to extract a radiation/scattering pattern of an infinite periodic problem in a finite FDTD model. Extended studies of selective frequency properties of PBC are covered. A waveguide model in the classic FDTD algorithm is also studied as an alternative for the periodic FDTD algorithm to the analysis of plane wave scattering from periodic structures. Finally, a Gaussian beam illumination of an infinite periodic structure is discussed to show the prospective limitations of the periodic FDTD approach.

Chapter 4 presents original study by the author of this thesis on the applicability of the FDTD method to modeling of an imaging phenomenon, which plays an important role in optical microscopes when a target's size becomes comparable to operating wavelengths. The issue of the potential application of the FDTD method coupled with a particular approximate optical approach to enhance capabilities of the overall algorithm of the far-field microscope imaging is then addressed.

Chapter 5 is focused on the near-to-near (NTN) transformation technique for the axisymmetrical problems, originally developed by the author of this thesis.

1.3 Original Contribution

This thesis presents the author’s original contribution in the following areas:

- development, implementation and evaluation of 2D and 3D periodic boundary conditions in 3D CL-FDTD algorithm (Chapter 3);
- development, implementation and evaluation of 1D and 2D periodic boundary conditions in V2D CL-FDTD algorithm (Chapter 3);
- development, implementation and evaluation of plane wave source in a 3D CL-FDTD algorithm (Chapter 3);
- development, implementation and evaluation of near-to-far transformation in a 3D CL-FDTD algorithm (Chapter 3);

- investigation of practical frequency bandwidth of the CL-FDTD algorithm (Chapter 3);
- evaluation of a waveguide model for plane wave scattering from periodic structures in the classic FDTD algorithm (Chapter 3);
- development, implementation and evaluation of V2DS CL-FDTD algorithm (Chapter 3);
- development, implementation and evaluation of a waveguide model of the plane wave scattering from periodic structures in CL-FDTD algorithm (Chapter 3);
- simulations of a Gaussian beam illumination of an infinite periodic structure (Chapter 3);
- development, implementation and evaluation of a hybrid FDTD-Fresnel algorithm applicable to the modeling of wide-field microscope tools (Chapter 4);
- development, implementation and evaluation of a hybrid FDTD-Fresnel algorithm applicable to the modeling of confocal microscope tools (Chapter 4);
- derivation, development and evaluation of near-to-near transformation for axisymmetrical structures (Chapter 5).

Chapter 2

Finite-Difference Time-Domain – Overview of the Method

2.1 Principles of the Method

Electromagnetism is a notion that bonds time-varying electric and magnetic fields together into inseparable quantities. Yet, up to the middle of the 19th century, scientists recognized both electric and magnetic fields as independent of each other. Afterwards, at the time when electricity and magnetism started to be extensively studied, Ampere's and Faraday's laws were the first that strictly related the motion of both physical quantities. After the unification of the contemporary understanding of electromagnetism made by James Clerk Maxwell, he proposed a set of 20 differential equations with 20 variables that linked all electric and magnetic components together. Eventually, by applying vector notation, all these formulae have been reduced to the following elegant set of 5 vector differential equations with 5 vector quantities:

$$\vec{\nabla} \times \vec{H} = \varepsilon_0 \frac{\partial \vec{E}}{\partial t} + \vec{J} \tag{2.1}$$

$$\vec{\nabla} \times \vec{E} = -\mu_0 \frac{\partial \vec{H}}{\partial t} \tag{2.2}$$

$$\vec{\nabla} \cdot \vec{B} = 0 \tag{2.3}$$

$$\vec{\nabla} \cdot \vec{D} = \rho \tag{2.4}$$

$$\vec{\nabla} \cdot \vec{J} = -\frac{\partial \rho}{\partial t} \tag{2.5}$$

where

H	-	magnetic field,
E	-	electric field,
J	-	electric current density,
B	-	magnetic flux density,
D	-	electric flux density,
ρ	-	electric charge density,
ε_0	-	free-space permittivity,
μ_0	-	free-space permeability.

The Ampere's (Eq.**2**.1) and Faraday's (Eq.**2**.2) formulae are known as electrodynamics equations, as they describe time-varying properties of an electromagnetic field. Gauss laws (Eq.**2**.3,4), which refer to static magnetic and static electric fields, respectively, consider these fields as separated from each other.

The time-dependent Maxwell's curl equations (Eq.**2**.1,2) were set into a finite difference scheme originally by Kane Yee in 1966 [**1**]. The special arrangement of electric and magnetic field components proposed by Yee is commonly called a Yee cell (see Fig.2.1). Such distribution of electromagnetic (EM) components allows solving the Maxwell's curl equations in the following discretized form, with second-order accuracy:

$$H_{x,i,j,k}^{n+0.5} = H_{x,i,j,k}^{n-0.5} + (E_{y,i,j,k+0.5}^{n} - E_{y,i,j,k-0.5}^{n})\frac{\Delta t}{\mu_0 \Delta z} + (E_{z,i,j-0.5,k}^{n} - E_{z,i,j+0.5,k}^{n})\frac{\Delta t}{\mu_0 \Delta y} \quad (\mathbf{2}.6)$$

$$H_{y,i,j,k}^{n+0.5} = H_{y,i,j,k}^{n-0.5} + (E_{z,i+0.5,j,k}^{n} - E_{z,i-0.5,j,k}^{n})\frac{\Delta t}{\mu_0 \Delta x} + (E_{x,i,j,k-0.5}^{n} - E_{x,i,j,k+0.5}^{n})\frac{\Delta t}{\mu_0 \Delta z} \quad (\mathbf{2}.7)$$

$$H_{z,i,j,k}^{n+0.5} = H_{z,i,j,k}^{n-0.5} + (E_{x,i,j+0.5,k}^{n} - E_{x,i,j-0.5,k}^{n})\frac{\Delta t}{\mu_0 \Delta y} + (E_{y,i-0.5,j,k}^{n} - E_{y,i+0.5,j,k}^{n})\frac{\Delta t}{\mu_0 \Delta x} \quad (\mathbf{2}.8)$$

$$E_{x,i,j,k}^{n+1} = E_{x,i,j,k}^{n} + (H_{z,i,j+0.5,k}^{n+0.5} - H_{z,i,j-0.5,k}^{n+0.5})\frac{\Delta t}{\varepsilon_0 \Delta y} + (H_{y,i,j,k-0.5}^{n+0.5} - H_{y,i,j,k+0.5}^{n+0.5})\frac{\Delta t}{\varepsilon_0 \Delta z} \quad (\mathbf{2}.9)$$

$$E_{y,i,j,k}^{n+1} = E_{y,i,j,k}^{n} + (H_{x,i,j,k+0.5}^{n+0.5} - H_{x,i,j,k-0.5}^{n+0.5})\frac{\Delta t}{\varepsilon_0 \Delta z} + (H_{z,i-0.5,j,k}^{n+0.5} - H_{z,i+0.5,j,k}^{n+0.5})\frac{\Delta t}{\varepsilon_0 \Delta x} \quad (\mathbf{2}.10)$$

$$E_{z,i,j,k}^{n+1} = E_{z,i,j,k}^{n} + (H_{y,i+0.5,j,k}^{n+0.5} - H_{y,i-0.5,j,k}^{n+0.5}) \frac{\Delta t}{\varepsilon_0 \Delta x} + (H_{x,i,j-0.5,k}^{n+0.5} - H_{x,i,j+0.5,k}^{n+0.5}) \frac{\Delta t}{\varepsilon_0 \Delta y} \quad (2.11)$$

where

Δt	-	time step,
n	-	time step index,
Δx, Δy, Δz	-	Yee cell dimensions,
(i,j,k)	-	Yee cell indices.

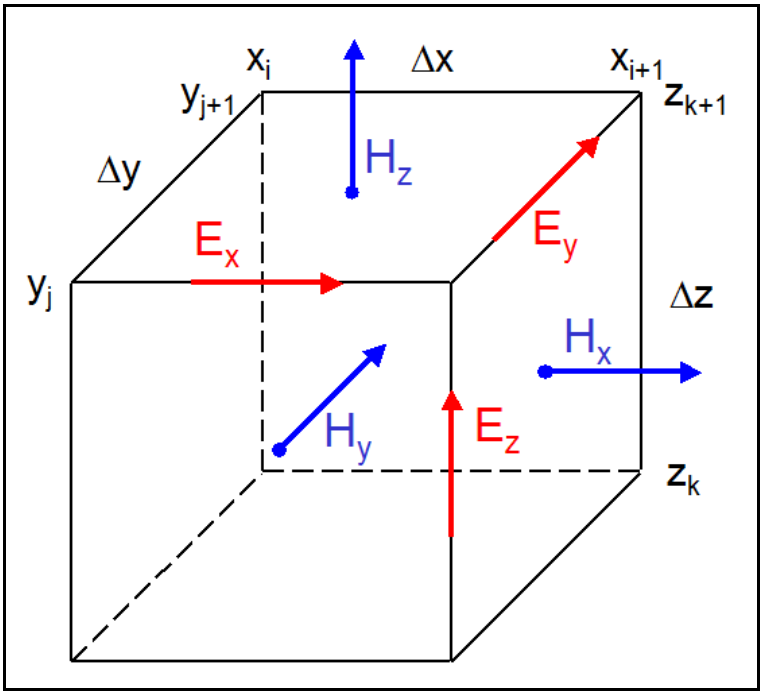

Fig.2.1. Yee cell.

The above set of discrete equations is the basis for the finite-difference time-domain (FDTD) computational scheme. As it can be noticed, electric and magnetic field components are computed in consecutive time instants, every half of a time step Δt, forming a so-called leapfrog time-stepping algorithm. The FDTD algorithm does not explicitly enforce the Gauss laws; nevertheless, as it has been pointed out in [**2**], the FDTD formulae are divergence-free with respect to *D* and *B* fields (compare Eq.**2**.3,4). It indicates that the FDTD algorithm, in its original form, is dedicated to the modeling of charge-free problems.

Relation between the spatial grid size and the time step are relevant to stability of the FDTD method. To keep the algorithm stable, a so-called Courant stability criterion must be satisfied:

$$r \geq \sqrt{3} \tag{2.12}$$

where

$$r = \frac{1}{c\,\Delta t}\sqrt{\frac{3}{\Delta x^{-2} + \Delta y^{-2} + \Delta z^{-2}}} \tag{2.13}$$

is a stability coefficient.

For the specified spatial grid, the time step has to be small enough to maintain the algorithm stable. Otherwise, an extensively large time step might result in the numerical speed of the FDTD algorithm being slower than the physical velocity of the considered EM wave, producing a runaway of a numerically propagating amplitude at the wavefront.

Another inherent property of the FDTD method related to the spatial discretization refers to the numerical dispersion, which results in limited accuracy of the FDTD algorithm. It is the reason why the phase velocity of a numerically propagated wave differs from the physical velocity of a wave and this discrepancy is frequency-dependent. In principle, inaccuracy due to the numerical dispersion is inversely proportional to the square of the spatial grid size. The rule of thumb is to set at least 10 FDTD cells per wavelength to keep the numerical dispersion below about 1.5%, though it is often required to set even more than 20-30 cells per wavelength.

Regarding computational capabilities, the FDTD method requires $A*N^4$ floating point operations, where N stands for the number of Yee cells along one side of the considered cube. Since each Yee cell consists of 6 EM components, the total number of variables stored in operating memory is approximately $6*N^3$. For instance, assuming that each EM component occupies 4 bytes, the cube comprising 100x100x100 FDTD cells requires at least 24MB, though an additional memory is needed for post-processing variables and some environmental data. However, refinement of the FDTD spatial grid by 2 requires $2^3 = 8$ times more operating

memory, i.e. 192MB. Additionally, the algorithm time step reduces twice, so the total computation time increases $2^4 = 16$ times. Thus, it can be easily noticed that a reasonable manipulation of the FDTD cell size can save a lot of computational resources. The aforementioned example indicates that the trade-off between accuracy and simulation time plays an important role in EM modeling with the FDTD method.

The basic FDTD algorithm can be enhanced with additional tools that extend its scope of applicability, such as:

1. Absorbing boundary conditions (ABC).

   The FDTD model with ABC applied at the outer boundaries allows considering the problem of EM radiation out to a free-space, truncating the size of the model. Two types of ABC are commonly known: Mur [**3**] and perfectly matching layer (PML) [**4**]. There are several versions of each of the ABC algorithms. A major property of the Mur ABC is that it can be accurately matched to a wave incoming at a particular direction, by changing the effective permittivity of the Mur absorption. Absorption of a wave incoming at angles different than the matched one is deteriorated to some extent. Consequently, it may happen that propagation of an electromagnetic wave at grazing angles can produce instability of the Mur ABC algorithm in resonant structures. Implementation of the so-called Mur superabsorption [**5**] can substantially alleviate the problem since the superabsorption is much less sensitive to variation of an incidence angle. As regards PML, it introduces additional unphysical quantities and encompasses a few FDTD layers, shrinking the effective volume of a scenario. However, the advantage of PML is that it is not so much angle-dependent and can be placed close to radiating sources without the risk of instability.

2. Mode excitation.

   It is possible to introduce a surface that excites a particular distribution of electric and magnetic tangential field components. Usually, it refers to the modes excited in rectangular/cylindrical waveguides or TEM lines but it can be also applied in arbitrarily shaped waveguides with inhomogeneous filling [**6**].

Furthermore, if an algorithm that extracts scattering parameters at each of the ports applied in a circuit is implemented, power distribution between the modes can be monitored [**7**],[**8**].

3. Total-field/scattered-field (TF/SF) sources.

   Such sources have different properties than the mode sources. Originally, they have been developed to excite an obliquely incident plane wave inside a limited volume [**9**], called a total field (TF) region. If no scattering objects are placed within the TF region, there will be no field radiation outside the considered volume, called the scattered field (SF) region. On the other hand, if there is an obstacle inside the TF region, only the scattered part of an EM wave outside the TF box in the SF region will be observed. This is a very useful technique in antenna analysis. It can be also used to excite other waves, like a Gaussian beam [**10**] or a lens source [**11**].

4. Near-to-far (NTF) transformation

   A near-to-far transformation is a post-processing that monitors EM fields at a specified surface (usually a cube surrounding a radiating object) and calculates their contribution to the far field radiation at a given direction. It is widely applied in antenna design [**12**],[**13**].

5. Conformal mesh.

   In a conformal mesh approach, the FDTD mesh is adapted to a curved geometry of objects without any loss of accuracy. The original FDTD scheme works with a simple rectangular representation of geometry, so curves are discretized in a staircase shape. It results in worse accuracy unless a very fine mesh is applied. By contrast, the conformal approach maintaining rectangular FDTD grid takes into account an arbitrary shape of media boundaries without an increased computational effort [**14**].

6. Media types.

   The FDTD method allows considering various media types, such as isotropic/anisotropic, lossless/lossy, dispersive/nondispersive, linear/nonlinear. Nonlinearity can be naturally treated in FDTD since it is a time-domain approach. However, some types of nonlinearity may be bound to problems of stability [**15**]. In the literature one can find applications to the Kerr and Raman phenomenona [**16**], as well as to diodes and transistors [**17**],[**18**]. Regarding dispersion, special models have to be applied to represent dispersion characteristics of the considered materials. Among the most common dispersive models Debye, Drude, and Lorentz can be recalled [**19**]. Once the specialized models are implemented, an FDTD simulation can provide results in the whole spectrum range after a single simulation run.

7. Periodic boundary conditions (PBCs).

   Among the useful types of boundary conditions, such as electric, magnetic, and absorbing, there are also PBCs, which allow modeling of infinite periodic structures with only one period defined. PBCs are usually applied at the opposite sides of a model to loop tangential field quantities. There are a few types of the PBC FDTD algorithms, e.g. *sin/cos* [**21**], complex looped [**22**], or split-field [**23**].

This is a brief review of the FDTD method and its major capabilities. Now, some strong and weak points of the method will be pointed out.

2.2 Advantages and Limitations

Among the major advantages of the FDTD method, the following can be mentioned:

1. Intuitive understanding of the algorithm execution.

   A time-domain approach enables watching instantaneous electromagnetic wave propagation inside the scenario during the simulation. In some cases, it

may be required to have such a possibility in order to better understand the properties of the considered circuit and to find the sources of potential problems.

2. Inherently wideband analysis.

   Unlike some other numerical methods, e.g. FEM or MoM, the FDTD method is, by definition, a wideband approach, providing a solution for a specified spectrum after a single simulation run, practically without any additional computation effort [**24**].

3. Unconditional stability.

   Provided that the Courant stability criterion is satisfied, the FDTD algorithm is unconditionally stable. Additionally, the algorithm is not sensitive to computer round-off errors, which, due to a central difference approach, are statistically suppressed.

4. Lack of spurious solutions.

   Some modeling methods bring the risk of spurious solutions, that are nonphysical in their nature and hard to distinguish from the physical ones. By contrast, the FDTD method, in its original form, is free of that risk [**25**].

However, as each modeling method applicable in electrodynamics, the FDTD method has some drawbacks and limitations. The most significant ones are the following:

I. Inherent dispersion of the algorithm (already mentioned above).

   The finite size of an FDTD cell size results in a shift of frequency characteristics. Although that effect can be reduced by applying finer meshing of the structure, the cost is in a larger demand for computational resources [**2**].

II. Long computation of high-Q structures.

Since energy in high-Q structures dissipates slowly, the time-domain approach requires adequately longer simulation time to obtain a stable result. There are methods that alleviate that problem applying specialized signal processing techniques, e.g. Prony's method [**26**],[**27**]. The analysis of high-Q structures is still challenging, due to finite resolution of the algorithm in time and space. It may be noted, however, that similar problems will appear in most of the other methods of analysis.

III. Approximation of a complex geometry.

When the object's geometrical details are very fine, as compared to the wavelength, and these details cannot be neglected, the FDTD cell size has to be reduced significantly below the size restricted by the dispersion limit. Thus, computation time increases substantially. There are at least two methods which can, in many cases, alleviate this problem: conformal meshing [**14**] and subgridding [**28**].

To summarize, a brief outline of the FDTD method has been presented. Major properties of the method have been pointed out, together with its inherent limitations. Subsequent chapters will be focused on the original contribution of the author of this thesis to the study and the development of the FDTD algorithm partially supported with analytical methods.

Chapter 3

FDTD Modeling of Electromagnetic Diffraction from Periodic Structures

3.1 Introduction

This Chapter presents the work and the original contribution of the author of this dissertation to the development of partially analytical FDTD algorithms (see definition in Chapter 1), dedicated to the modeling of electromagnetic (EM) diffraction from periodic structures. The Chapter will be mainly focused on the extensions of the Complex Looped FDTD (CL-FDTD) algorithm [**22**], which belongs to the class of algorithms based on a complex computational grid. A few modeling approaches will be considered to indicate their different capabilities.

Section 3.2 reviews state-of-the-art FDTD modeling of periodic problems, with emphasis on its applicability to scattering problems. Section 3.3 describes, in a more detailed way, the procedure of looping periodic boundary conditions (PBCs) in the CL-FDTD algorithm extended by the author to 2D and 3D periodicity. Section 3.4 presents the applicability of the CL-FDTD algorithm to electromagnetic modeling of resonant properties of periodic structures. In particular, it is shown how to extract eigenvalues and corresponding eigenfunctions of structures with 1D, 2D, and 3D periodicity. In Section 3.5, scattering of an EM wave from a periodic structure is investigated. For that purpose, several modeling scenarios are introduced, depending on the specific requirements imposed on the EM analysis. Several issues are taken into account, such as angle of incidence (perpendicular or oblique), polarization (TE or TM), beam shape (plane wave or Gaussian beam), diffraction orders (specular reflection or higher diffraction orders) and, finally, the size of a model (finite or infinite). In the first step, the approximate approach of an infinite periodic structure obliquely illuminated by an infinite plane wave will be addressed to point out the major advantages and disadvantages of the CL-FDTD algorithm. Two types of simulation models will be considered. The first one refers to an obliquely propagating traveling plane wave. The author adapted a near-to-far (NTF) transformation in the CL-FDTD algorithm to apply it for the

detection of existing diffraction orders (not only specular one). The second model is based on a waveguide approach with PBCs. As it will be shown, it is dedicated to the analysis of diffraction phenomena when only specular reflection is feasible. Finally, the last Section of this Chapter concentrates on a Gaussian beam illumination of periodic structures. For that purpose, the FDTD algorithm without periodic boundary conditions will be applied assuming the model with a large, but still finite, number of periods of the structure.

3.2 State-of-the-art in FDTD Modeling of Periodic Structures

Early studies on the FDTD algorithms dedicated to the analysis of periodic structures were strongly related to the development of the modeling methods for vector two-dimensional (V2D) or guiding problems. The class of V2D problems has been originally addressed in [**29**], where it has been pointed out that guiding circuits with the shape invariant along a specified dimension can belong to the V2D class. According to [**29**], assigning this specified dimension as the *z*-axis, the field inside such a circuit can be decomposed in the following way:

$$\vec{E}_{\perp}(x,y,z,t) = \vec{E}_{\perp}(x,y,t)\ \cos(\beta_z z + \varphi) \tag{3.1}$$

$$\vec{H}_{\perp}(x,y,z,t) = \vec{H}_{\perp}(x,y,t)\ \sin(\beta_z z + \varphi) \tag{3.2}$$

$$\vec{E}_{z}(x,y,z,t) = \vec{E}_{z}(x,y,t)\ \sin(\beta_z z + \varphi) \tag{3.3}$$

$$\vec{H}_{z}(x,y,z,t) = \vec{H}_{z}(x,y,t)\ \cos(\beta_z z + \varphi) \tag{3.4}$$

where $\perp$ in the subscript denotes tangential components (x,y) and β_z represents the phase constant.

It has also been shown that the V2D FDTD algorithm can be expressed using complex notation in the condensed and expanded nodes [**30**]-[**35**]. These studies prepared the background for the future development of the first FDTD algorithms dedicated to the modeling of periodic structures. The authors of these papers proposed a 2D version of the FDTD algorithm for full-wave analysis of guiding structures, where the phase constant β_z of a propagation mode is imposed inside the algorithm in the following manner:

$$\vec{E}_{\perp}(x, y, z + \Delta h, t) = \vec{E}_{\perp}(x, y, z, t)e^{-j\beta_z \Delta h} \quad (\mathbf{3}.5)$$

$$\vec{H}_{\perp}(x, y, z + \Delta h, t) = \vec{H}_{\perp}(x, y, z, t)e^{-j\beta_z \Delta h} \quad (\mathbf{3}.6)$$

where $\perp$ in the subscript denotes tangential components (x,y).

Due to that kind of approach, an FDTD model might be reduced – like in the V2D FDTD method [**6**] – to one FDTD layer, representing structure's cross-section with all six electromagnetic components taken into account. In consequence, the method allows both *E* and *H* modes to appear simultaneously in one simulation run.

The concept of a constant phase shift in the frequency domain was adapted in [**20**] and [**21**] to the FDTD modeling of periodic structures, though the latter one misses all the mathematical formalism. It is indicated that the length of the model can be reduced to a single period with periodic boundary conditions imposed at the edges of the model. However, in order to deal with that fact, according to Eq.**3**.5,6, a complex phasor has to be introduced in the time domain.

The authors of [**21**] proposed to carry on two simulations of the same structure, simultaneously. The first FDTD grid is excited with a sine, whereas the other one with a cosine. Hence, *sin/cos* is a common name of the method. After each iteration of the algorithm, both grids are coupled at PBCs (see Eq.**3**.5,6). Such an approach allows carrying on the time-domain simulation of a periodic structure despite the complex form of the Floquet theorem applied at the PBCs. However, it should be pointed out that the definition of the two FDTD grids results in a doubled memory occupation and at least the same level of decrease in the speed of the algorithm.

Another significant step forward in better understanding and development of the FDTD algorithms dedicated to periodic problems was published in [**20**], and extended in [**22**]. Although [**21**] presented quite similar approach with spatial complex notation applied directly in the time domain, [**22**] provides all methodology in a systematic and comprehensive way, using mathematical formalism of the Floquet theorem.

The authors of [**22**] studied propagation of an EM wave along a periodic structure. Assuming that the structure is periodic along the *z*-axis, they concluded that in order to satisfy the Floquet theorem, the following periodic boundary conditions must be imposed:

$$\vec{E}_{\perp}(x,y,z+L,t) = \vec{E}_{\perp}(x,y,z,t)\, e^{j\psi} \tag{3.7}$$

$$\vec{H}_{\perp}(x,y,z,t) = \vec{H}_{\perp}(x,y,z+L,t)\, e^{-j\psi} \tag{3.8}$$

where $\perp$ stands for the components transverse to periodicity, and $\psi = \beta_{z0} L$ is a fundamental Floquet phase shift per period *L*.

Since the complex-looped FDTD (CL-FDTD) method introduced in [**20**] does not introduce the changes inside the FDTD algorithm executed on both real and imaginary FDTD grids, it allows propagation of an EM plane wave at an arbitrary incidence angle without the risk of unstable behavior of the algorithm. However, a major drawback is that the method is frequency selective. Thus, in order to analyze illumination of a structure at a particular angle of incidence within a specified spectrum, several simulations must be executed independently.

Almost in the same time, some other articles concerning that issue were published but the authors referred to a slightly different application, namely to the perpendicular (broadside) illumination of a periodic structure [**36**]. In this specific case, EM fields are looped at periodic boundaries in a simple manner with a zero phase shift (compare Eq.**3**.5,6), which is invariable with frequency. Thus, a broadband advantage of the FDTD method is maintained, though the applicability is definitely limited to only one illumination angle.

Now, let us consider another approach to the FDTD modeling of periodic structures, commonly called "split-field update technique". This method was originally introduced in [**23**], but the major interest appeared a few years later - [**37**],[**38**],[**39**],[**40**]. The aim of this algorithm is to cope with the oblique incidence of a pulse-driven plane wave onto a periodic structure. Looping of field quantities at the periodic boundaries is not trivial for the oblique incidence since the knowledge about the field values in different time instants is needed. To overcome this issue, the authors of the "split-field update technique" proposed to exchange the classic EM field quantities:

$$\vec{E} = \vec{E}_0 \, e^{jk_x x + jk_y y - jk_z z} \tag{3.9}$$

$$\vec{H} = \vec{H}_0 \, e^{jk_x x + jk_y y - jk_z z} \tag{3.10}$$

with the new ones:

$$\vec{P} = \vec{E} \, e^{-jk_x x - jk_y y} = \vec{E}_0 \, e^{-jk_z z} \tag{3.11}$$

$$\vec{Q} = \vec{H} \, e^{-jk_x x - jk_y y} = \vec{H}_0 \, e^{-jk_z z} \tag{3.12}$$

where (k_x, k_y, k_z) is the propagation vector of an incident plane wave.

In the newly created *P*&*Q* domain the wave is normally incident along the *z*-axis. Application of PBCs becomes trivial since there is no phase shift of *P* and *Q* quantities in the *xy*-plane. The original Maxwell curl equations have to be transformed to the new *P*&*Q* domain and a new leapfrog FDTD algorithm has to be applied. The advantage is that in contrast to the *sin/cos* [**21**] or CL-FDTD [**22**] methods, "split-field update technique" operates on one grid. Thus, memory requirements and computational effort are about twice less. Nevertheless, a time step in this algorithm decreases with increasing incident angle and simulation becomes unstable for grazing angles.

While further developing the *sin/cos* and CL-FDTD algorithms, A.Aminian and Y.Rahmat-Samii proposed an extension, called Spectral FDTD (SFDTD) [**41**]. In principle, [**41**] is an extension of [**22**] to the excitation of a wideband traveling plane wave with a constant phase shift along periodicity. In consequence, an incident angle varies with frequency. Thus, for each frequency, the structure is scanned at a different angle of incidence.

The last issue discussed in this Section refers to the FDTD modeling of a finite-size source over an infinitely periodic structure such as, for instance, a point source located above a periodic grating or a Gaussian beam illuminating a periodic structure. The article published by R.Qiang et al. [**42**] should be mentioned here, as it seems to be the first publicly available study of this issue in relation to the FDTD method. It has been further explained in [**43**]. The authors apply the expansion of an arbitrary EM source into a series of plane wave sources

with a varying propagation vector. Thus, the original finite-size source is substituted with an integral of plane wave sources. In the literature, two names of that approach can be found: spectral expansion [**43**], or array scanning method (ASM) [**44**]. Such an approach may be very useful if the considered problem requires too much operating memory than can be provided. In such a case, one simulation of the scenario consisting of many periods of the analyzed structure can be substituted with a dozen or more periodic simulations with plane wave illumination of a varying incidence angle.

To summarize, the FDTD modeling of periodic problems has been developed since late 1980's and much has been done so far. The next Chapter will be focused on the author's contribution to the CL-FDTD algorithm, especially in terms of scattering problems. Section 3.3 presents periodic boundary conditions (PBCs) implemented in all three spatial dimensions. Section 3.4 shows applicability of PBCs to EM modeling of eigenvalue periodic problems. Section 3.5 focuses on application of the enhanced CL-FDTD algorithm to the modeling of EM wave scattering from periodic structures.

3.3 Periodic Boundary Conditions

Periodic boundary conditions for the CL-FDTD algorithm have been originally proposed in [**20**] and specified for the structure periodic along the *z*-axis. Nevertheless, since the authors of [**20**] did not emphasize the implementation details of a looping mechanism, this issue will be discussed first to avoid ambiguity. Fig.3.1 depicts the operation scheme of the PBC algorithm, assuming that L is a period of the structure along the *z*-axis. Appropriate equations for the PBC are given in [**20**] and in [**22**].

First of all, it can be noticed that, in comparison to the scenario with perfect electric conductor (PEC) boundaries, one additional sublayer has been added and two others have been modified, respectively:

- first sublayer: H_x, H_y;
- second sublayer: E_x, E_y, H_z;
- last sublayer: E_x, E_y.

The whole circuit, including the modified second sublayer with E_x, E_y, H_z, is updated at each iteration of the leapfrog FDTD algorithm, whereas the boundary sublayers (the first and the

last) are updated with the PBC looping algorithm. Consequently, the last sublayer with E_x, E_y components follows from the corresponding components from the second layer shifted by the complex coefficient $exp(-j\psi_z)$, whereas the first sublayer with H_x, H_y is coupled to the last but one sublayer with the phase shift of the opposite sign $exp(+j\psi_z)$.

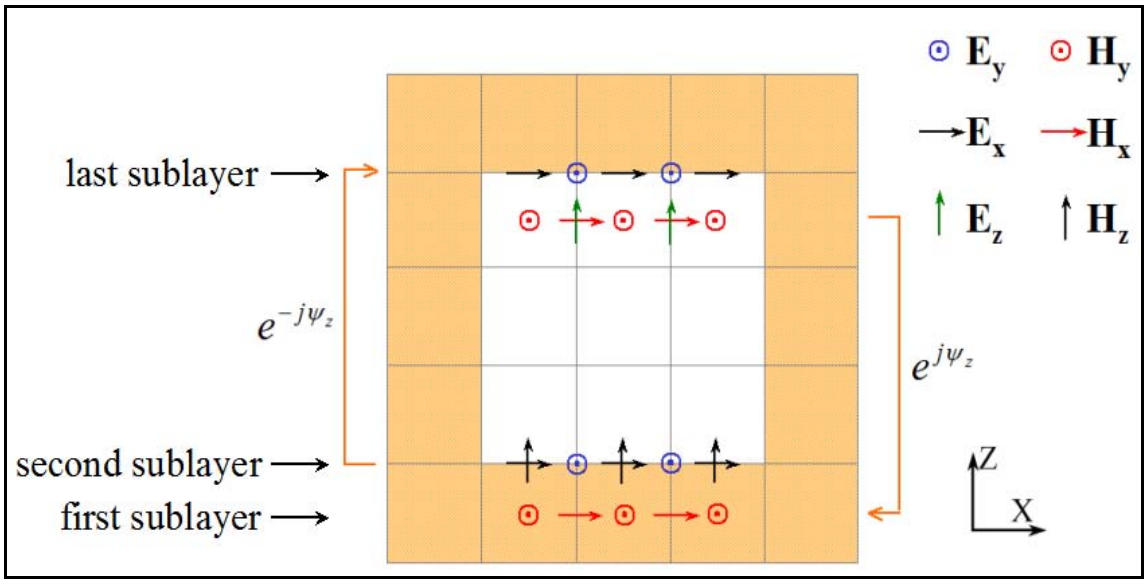

Fig.3.1. Periodic boundary conditions along the *z*-axis in the CL-FDTD algorithm.

It should be clearly pointed out that the term 'FDTD grid' refers, in fact, to the grid of complex numbers. It indicates that each EM component in the CL-FDTD algorithm is composed of a real and an imaginary part. In practice, both the real and the imaginary grids are computed independently and coupled at the PBCs. However, similarly to the interpretation of complex notation applied in the time domain, each part of the complex FDTD grid contains description of physical properties of the modeled problem. Typically, the real part is considered in a physical interpretation. Since benchmark examples have already been discussed in [**22**], now a description of the PBCs along the *x*-axis will be presented, which has been developed and verified by the author of this thesis.

Fig.3.2 depicts the operation scheme of the PBC loop along the *x*-axis. Comparing to the scenario with PEC boundaries, one additional sublayer has been added and two others have been modified, respectively:

- first column: H_y, H_z;
- second column: E_y, E_z, H_x;
- last column: E_y, E_z.

The electric components E_y, E_z are looped forward and the magnetic H_y, H_z backward, in a similar manner as it has been shown for the periodicity along the *z*-axis.

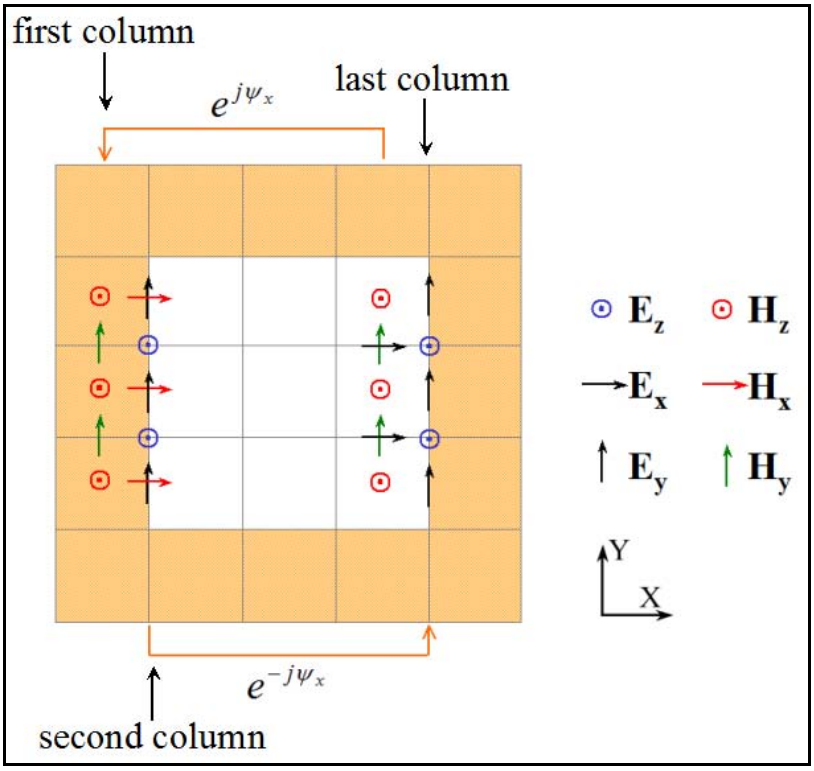

Fig.3.2. Periodic boundary conditions along the *x*-axis in the CL-FDTD algorithm.

Looping the PBCs along the *y*-axis looks very similar to the aforementioned periodicity along the *x*-axis, so its detailed description is skipped here. Hence, a problem of 2D periodicity in the *xy*-plane will now be considered. This time two parameters are applied, i.e. phase shifts along the *x*- and the *y*-axis:

$$\vec{E}_{y,z}\left(x+L_x,y,z,t\right)=\vec{E}_{y,z}\left(x,y,z,t\right)\,e^{-j\psi_x} \tag{3.13}$$

$$\vec{H}_{y,z}\left(x,y,z,t\right)=\vec{H}_{y,z}\left(x+L_x,y,z,t\right)\,e^{j\psi_x} \tag{3.14}$$

$$\vec{E}_{x,z}\left(x,y+L_y,z,t\right)=\vec{E}_{x,z}\left(x,y,z,t\right)\,e^{-j\psi_y} \tag{3.15}$$

$$\vec{H}_{x,z}\left(x,y,z,t\right)=\vec{H}_{x,z}\left(x,y+L_y,z,t\right)\,e^{j\psi_y} \tag{3.16}$$

Fig.3.3 illustrates the looping mechanism composed of the individual PBCs along the *x*- and *y*-axis with some slight changes. Additional H_x, H_y and E_z components, which were not

needed in the case of 1D periodicity along the *x*- or *y*-axis, are indicated with 4 thick circles in Fig.3.3. These surplus components are necessary to properly model periodicity at the corners of the circuit. Both the additional electric field components E_z at the bottom-right and top-left corners are updated from the same value at the bottom-left corner, but with different phase shifts. Similarly, the additional magnetic field component H_x at the bottom–left corner is updated backward from the corresponding component at the top-left corner. The last of the additional magnetic field components H_y located at the bottom-left corner is also updated backwards from the corresponding components in the bottom-right corner. The electric component E_z at the top-right corner of the circuit is not needed since it does not contribute to any other EM component of the circuit.

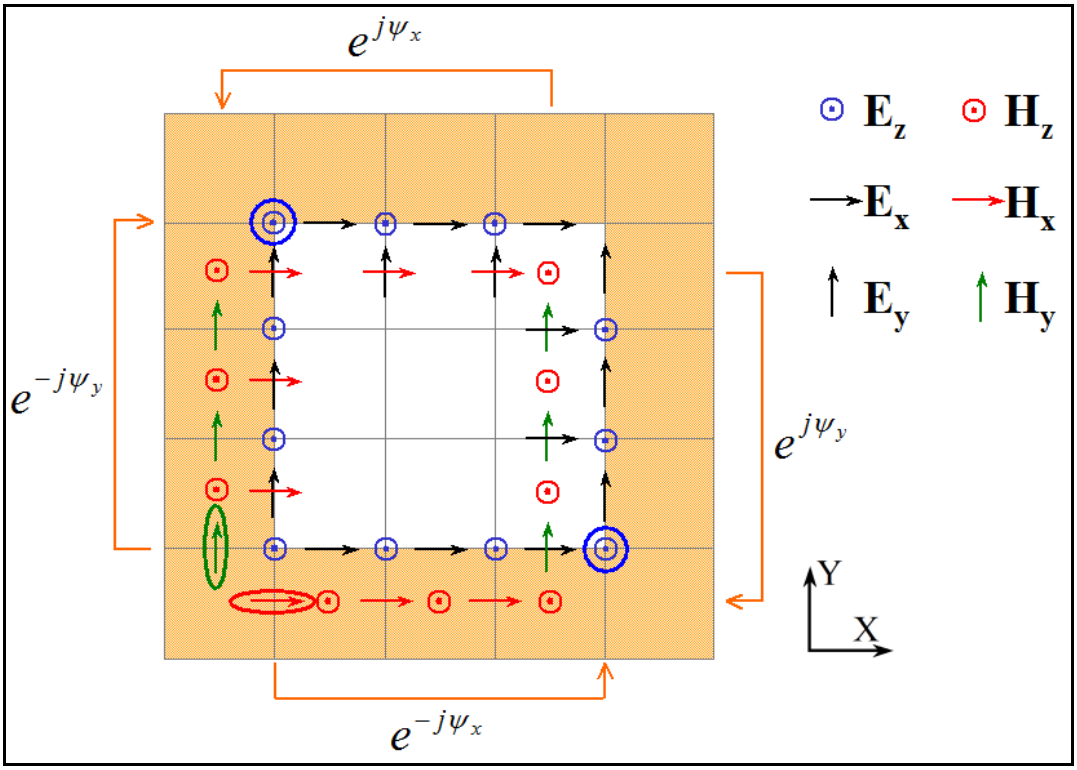

Fig.3.3. Periodic boundary conditions in the *xy*-plane in the CL-FDTD algorithm.

The rest of 2D periodic boundary conditions are quite straightforward and will not be discussed here. Regarding 3D periodic boundary conditions, it is composed of those for *xy*- and *z*-periodicity as shown in Figs.3.1,3. Implementation details are given in Appendix 1. Next Section will be focused on the applicability of the CL-FDTD algorithm to the investigation of resonant modes in periodic structures.

3.4 Eigenvalue Periodic Problems

Eigenvalue problem is a notion often used not only in the formalism of linear algebra, but also in the engineering practice. However, before concentrating on the eigenvalue problem in electrodynamics, some algebra terms will be reminded.

Let us assume that ***F*** is a linear operator. A scalar λ is said to be the eigenvalue of ***F*** if there is a nonzero vector ***r*** that satisfies the following equation:

$$F\,\vec{r} = \lambda\,\vec{r} \tag{3.17}$$

Vector ***r*** that satisfies the above equation is called the eigenvector of operator ***F***, whereas a whole set of eigenvalues is sometimes called the spectrum of operator ***F***. In practice, Eq.**3**.17 informs that operator ***F*** does not change the direction of vector ***r***, but only rescales it by λ. Depending on the scientific discipline concerned, vector ***r*** may be understood as a space, function, resonant mode, quantum state etc., whereas λ denotes a scalar number, resonant frequency or energy level of quantum state.

In particular, in electrodynamics operator ***F*** is often understood as a D'Alembert operator $\nabla^2 - \partial^2 \big/ \partial t^2$, and vector ***r*** as a resonant mode of an investigated circuit. In consequence, the eigenvalue indicates a resonant frequency or a propagation constant.

A procedure of collecting eigenmodes and eigenfrequencies during EM simulation with the CL-FDTD algorithm often proceeds as follows:

1. define a periodic structure and specify a fundamental phase shift per period;
2. excite the circuit with a wideband pulse;
3. execute the Fourier transform of the circuit impulse response (e.g. electric current injected by the source) and search for the resonances that indicate eigenfrequencies;
4. run another simulation with a sinusoidal excitation at one of the found eigenfrequencies to observe the eigenmode field distribution.

The aforementioned procedure is generally applicable to various kinds of eigenproblems' searching. In the further investigation, two types of problems will be considered. The first concerns 3D eigenvalue periodic problems, whereas the second refers to eigenvalue periodic problems in the structures that belong to the already mentioned V2D class [**6**]. This analysis will be useful in the modeling of a plane wave scattering from infinite periodic structures.

3.4.**1 3D Eigenvalue Periodic Problems**

Some practical examples of 3D eigenvalue periodic problems will now be considered, in order to verify the accuracy of the method. A trivial scenario composed of an empty air region terminated with a perfect electric conductor (PEC) along the *y*- and *z*-axis and with PBCs imposed along the *x*-axis will be considered first. Dimensions of the air cube are 50mm x 20mm x 10mm. The aim is to find the modes that can appear in such a waveguiding structure with no phase shift along the periodic side (ψ_x = 0 rad). Thus, let us put an excitation point inside the volume and drive an E_z component with a delta pulse on the real FDTD grid. It is quite easy to predict that the eigenmode should be observed at f = 7.5GHz. Fig.3.4 shows a spectrum of the injected current with some resonances indicated. Indeed, the first mode is at f = 7.49GHz, but other eigenfrequencies can also be observed. It follows from the fact that the imposed phase shift per period $\psi_x = \beta_x L_x$ is satisfied not only for the fundamental propagation constant β_{x0}, but also for other modes usually called spatial harmonics satisfying the following relation:

$$\beta_{xn} = \beta_{x0} \pm \frac{n 2\pi}{L_x} \tag{**3**.18}$$

Fig.3.5,6 show distribution of the relevant electric and magnetic components for the modes at f = 7.49GHz and 9.6GHz, respectively. It can be observed that there is no field variation along periodicity (*x*-axis) at the first frequency, whereas electric (magnetic) field has a sine (cosine) shape along the *y*-axis, due to the imposed PEC boundaries. Actually, the snapshots of these components indicate it is a resonant mode E_{010}. Regarding the second frequency, exactly one period is distributed along periodicity (*x*-axis) and the field distribution resembles E_{210} mode.

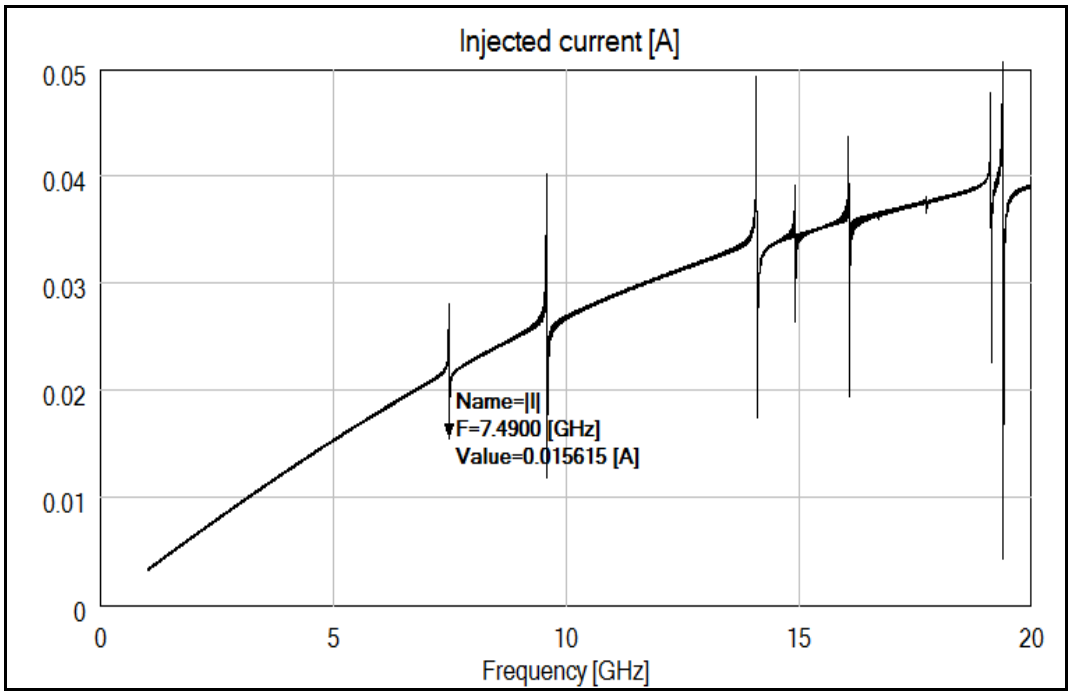

Fig.3.4. Spectrum of the current injected into an empty air cube (ψ_x = 0 rad, 50mm x 20mm x 10mm).

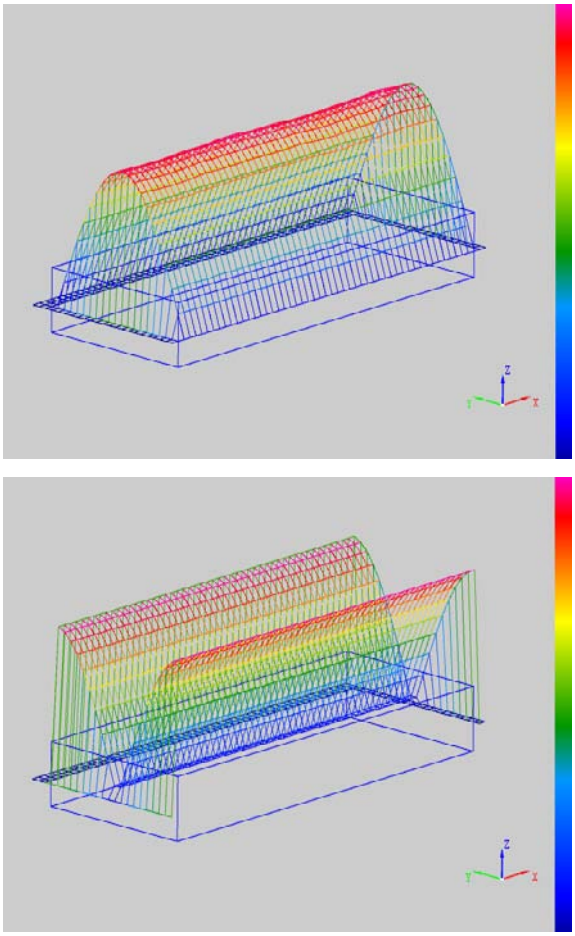

Fig.3.5. Distribution of E_z (left) and H_x (right) components in the *xy*-plane of the real FDTD grid at f = 7.49GHz (ψ_x = 0 rad, 50mm x 20mm x 10mm).

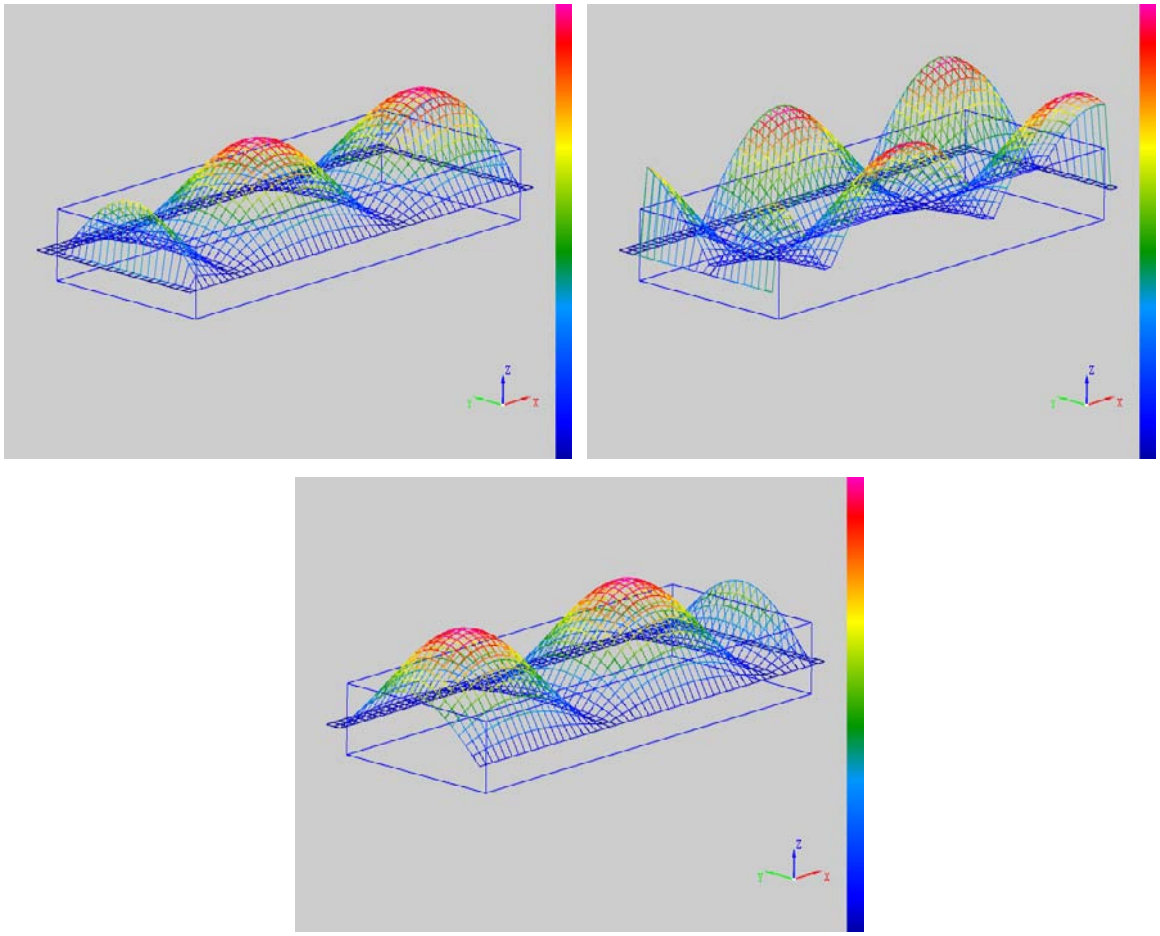

Fig.3.6. Distribution of E_z (left), H_x (right) and H_y (bottom) components in the *xy*-plane of the real FDTD grid at f = 9.6GHz (ψ_x = 0 rad, 50mm x 20mm x 10mm).

Let us now consider an example with a 2D periodicity. Recently, there has been a wide and still growing interest in the so-called photonic crystals (PhCs), as they are a specific arrangement of dielectric media resembling a solid crystal, but in a different scale. In practice, most of PhCs find their application within an optical spectrum as structures with 2D periodicity. Thus, let us consider the following example of the PhC composed of a rectangular lattice of infinitely long GaAs rods (ε_r = 11.56) with a radius r = 1μm and a lattice constant a = 10μm [**45**] (see Fig.3.7). The aim is to extract a photonic bandgap (PBG) diagram for TM polarization in the first irreducible Brillouin zone[1]. The model is reduced to one rod only with PBCs imposed at the lateral boundaries, whereas due to the TM polarization the model is truncated in the *xy*-plane to one FDTD layer between PEC boundaries.

[1] See Appendix 2.

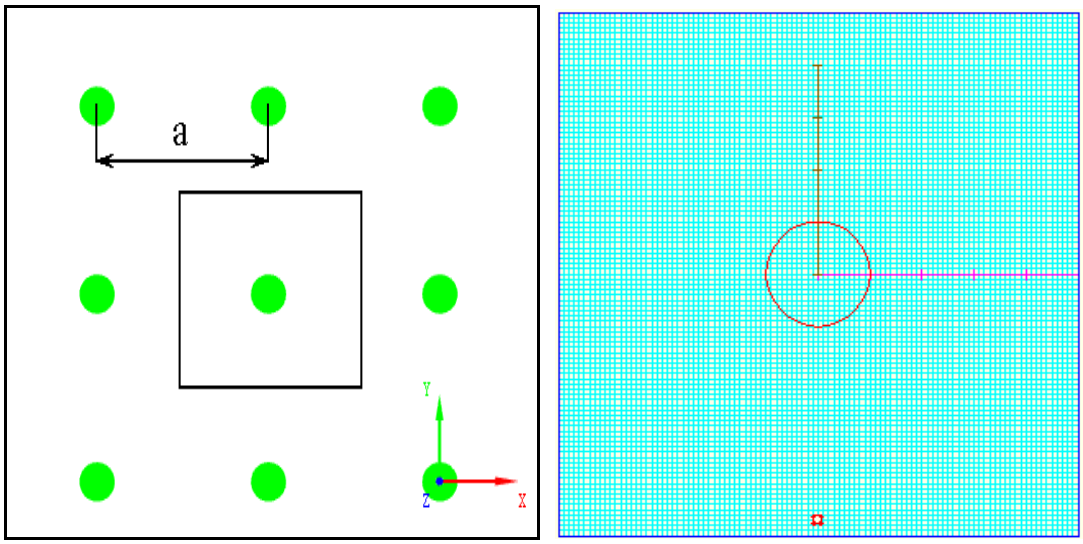

Fig.3.7. Rectangular lattice of GaAs rods (left) and its CL-FDTD model (right).

Fig.3.8 illustrates the distribution of electric and magnetic field components of the fundamental mode observed at f = 23.08 GHz, for the Floquet phase shifts equal to $\psi_x = \psi_y = \pi/2$ rad. It can be clearly seen that the symmetry axis of both distributions is inclined by 45^0 from x-axis, what exactly corresponds to the equal Floquet phase shifts along both periods.

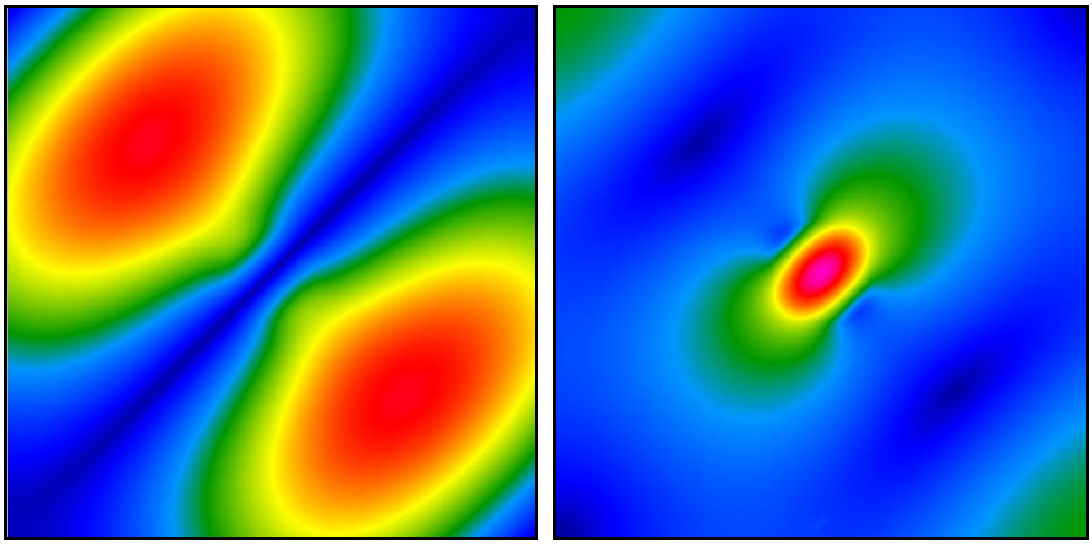

Fig.3.8. Envelope of electric (left) and magnetic (right) field components on the real FDTD grid at f = 23.08 THz ($\psi_x = \psi_y = \pi/2$ rad).

Extraction of the whole PBG diagram requires performing several simulations for various phase shifts ψ_x and ψ_y within the first irreducible Brillouin zone. Fig.3.9 shows the obtained PBG diagram for TM polarization and it is clearly visible that there is a relatively narrow bandgap for a/λ = 0.42 ... 0.49 (f = 12.7 … 14.8 THz). It indicates that the considered

photonic crystal is opaque for a TM-polarized wave within that spectrum range, regardless of the direction of the EM wave in the *xy*-plane. A comparison of the obtained PBG diagram with the one obtained in [**45**] shows a good agreement. However, the results after [**45**] are not shown in Fig. 3.9 to maintain legibility of the Figure.

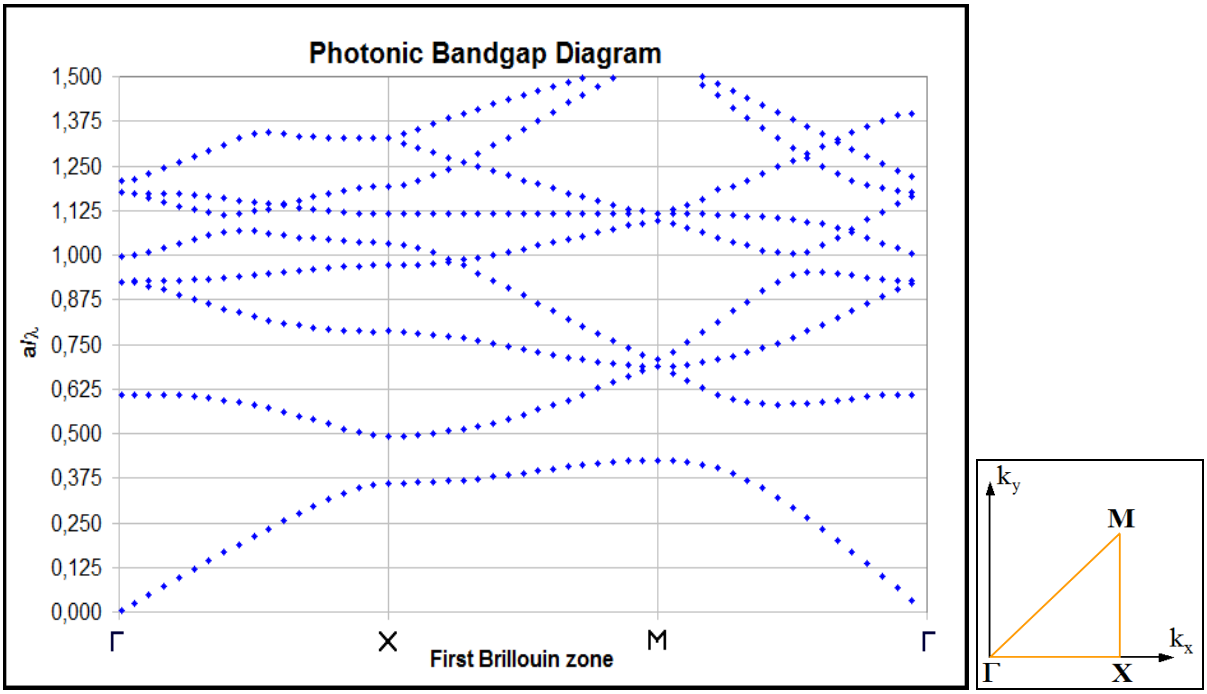

Fig.3.9. PBG diagram (left) in the first irreducible Brillouin zone (right) of the PhC lattice shown in Fig.3.7.

This time, a 3D rectangular photonic crystal lattice composed of silica balls (ε_r = 2.25) of a radius r = 0.15μm uniformly distributed in the vacuum will be considered (see Fig.3.10). A lattice constant is equal to a = 1μm. Let us assume that the aim is to find the fundamental mode with zero phase shifts along three axes ($\psi_x = \psi_y = \psi_z = 0$ rad). It should be emphasized that searching for the Floquet modes in a relatively large circuit might be a rather difficult task. It stems from the fact that location as well as polarization of an excitation source has an impact on its coupling with the searched modes. Thus, it is recommended to run a few simulations for different positions of the source and for various polarizations. It should significantly reduce the risk of missing some of the modes. Nevertheless, all of these efforts may still be insufficient since the point source may not be able to pump energy effectively into the circuit and, in consequence, long computing time will be needed to distinguish eigenfreqeuncies on the spectrum of the impulse response. Therefore, sometimes it is recommended to use a matrix of point sources to increase the coupling of the source with the

circuit and, in consequence, speed up the simulation. To find the Floquet modes, 5 x 5 x 5 matrix of E_z sources is set near one of the corners of the model. The rest of the procedure follows in a similar manner as in the previous example. Fig.3.11,12 show the distribution of electric and magnetic components in the *xy*- and *xz*-planes for the mode found at f = 590 THz. Symmetrical distribution of the EM components can be noticed with the electric field concentrated inside the balls and the magnetic field focused on the balls' rim. Such distribution satisfies the imposed phase shifts per period.

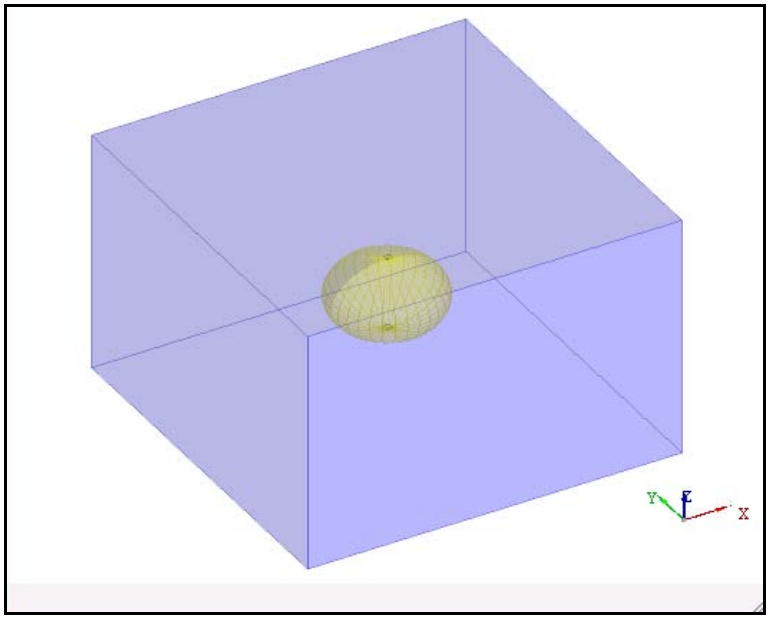

Fig.3.10. Photonic crystal lattice (a = 1μm) made of silica balls (ε_r = 2.25, r = 0.15μm) located in a vacuum.

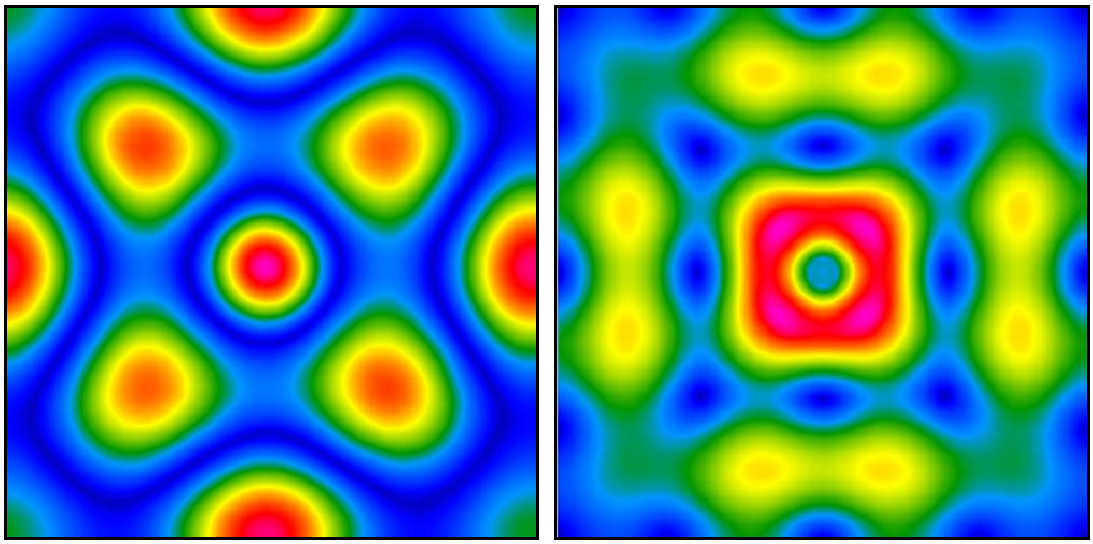

Fig.3.11. Electric (left) and magnetic (right) field components in the *xy*-plane at f = 590 THz.

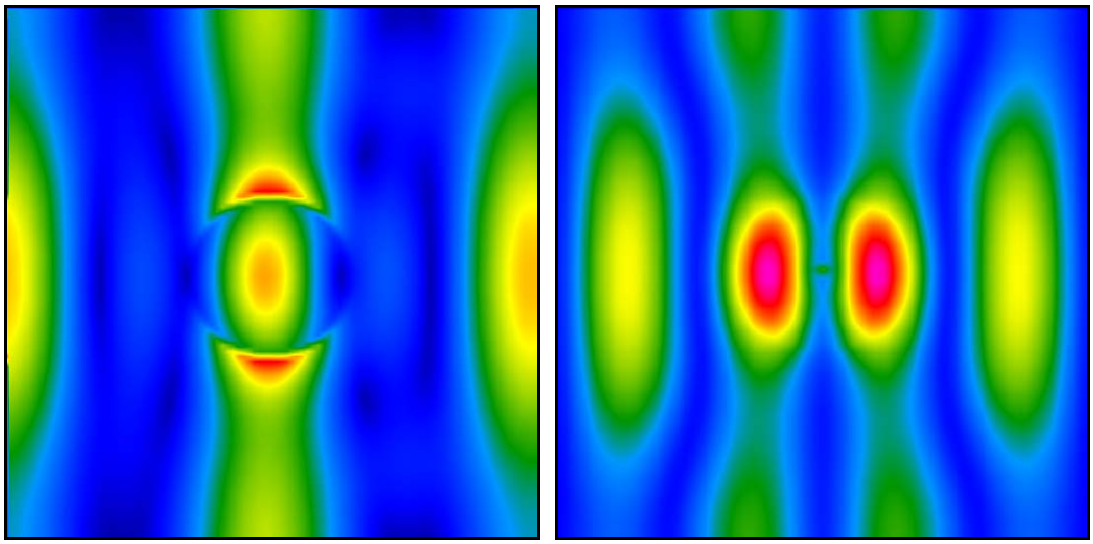

Fig.3.12. Electric (left) and magnetic (right) field components in the *xz*-plane at *f* = 590 THz.

The goal of the next example is to evaluate 3D periodic boundary conditions implemented in the CL-FDTD algorithm. It will be validated against the plane wave expansion method as one of the computational techniques for the analysis of dispersive properties of photonic crystals [**46**]. The example is taken from [**47**], where the authors consider a three-dimensional body centered cubic (bcc) lattice[2] processed in a dielectric material with a relative permittivity ε_r = 25. Let us set the lattice constant to a = 0.6 μm. The bcc shape is made using an air cube with a side length 0.75a, cut in its center and in each corner of a dielectric bulk (see Fig.3.13).

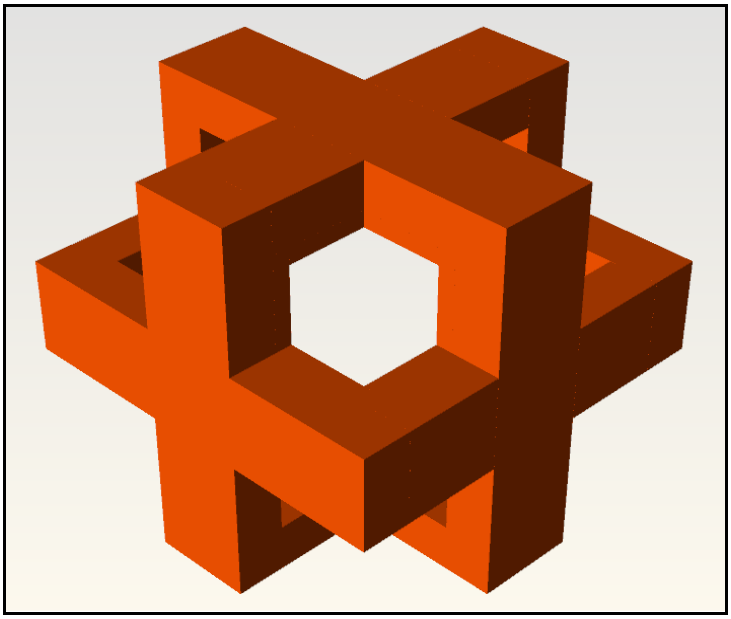

Fig.3.13. Single cell of the rectangular body centered cubic lattice (ε_r = 25, a = 0.6μm).

[2] See Appendix 2.

The cell size in the CL-FDTD model of the considered bcc lattice is set to 20nm. Periodic boundary conditions are applied along three Cartesian axes. The procedure for PBG diagram collection is exactly the same as recalled during the analysis of the structure shown in Fig.3.8. Special care must be taken with the location of the excitation source. Its improper location may result in weak coupling with some of the lattice modes. Therefore, the analysis has been performed twice, with different locations of the point source in order to double-check whether all the modes were found. Fig.3.14 shows the obtained PBG diagram of the bcc lattice. It may be noticed that a complete band gap occurs for a/λ = 0.374…0.382. Comparison against the results from [**47**] shows a good agreement, though it was not plotted to maintain legibility of the Figure.

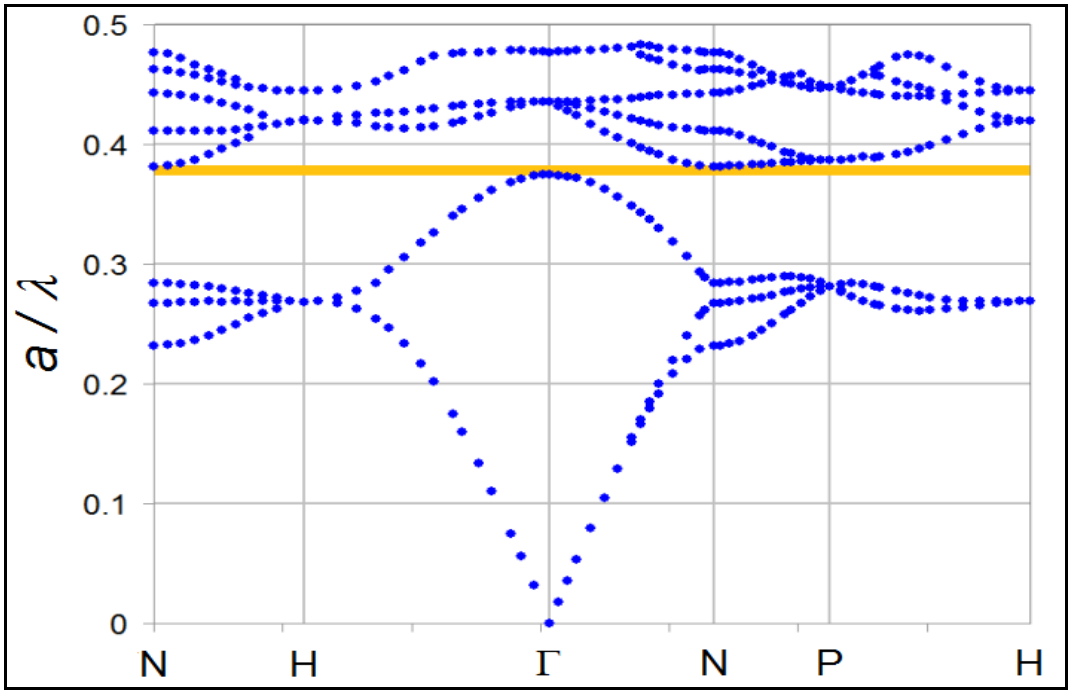

Fig.3.14. PBG diagram (left) in the first irreducible Brillouin zone (right) of the body centered cubic lattice shown in Fig.3.13.

To summarize this Section, periodic boundary conditions introduced in the CL-FDTD algorithm along the three Cartesian axes enable the investigation of Floquet modes in periodic structures. Author's contribution includes the extension of PBCs presented in [**20**] for 1D to 2D and further 3D periodicity. Presented examples confirm the validity of the implemented algorithms.

3.4.2 V2D Eigenvalue Periodic Problems

The issue of electromagnetic problems belonging to V2D class has been briefly addressed at the beginning of Chapter 3.2. The V2D FDTD algorithm is often useful for preliminary computation at input and output ports of the circuit. The obtained solution can further be coupled to a whole 3D circuit as an excitation source, or a load matched to the particular mode. Such an approach significantly simplifies the analysis as well as the understanding of the phenomenon of wave propagation in the waveguiding structures. In general, the procedure is as follows:

1. Wideband simulations are performed for all input and output ports defined in the circuit. For that purpose, each port – understood as the cross-section layer of the waveguide feed or load – is modeled as a V2D circuit and the distribution of the propagating mode is searched for a fixed longitudinal phase constant β_f assumed by the user. In case of typical waveguides such as the rectangular one, dispersive behavior of the modes is analytically known, so the whole procedure for the mode searching can be fully automated, like in QuickWave-3D software package [**48**].
2. Once the frequency associated with the particular mode is found, the V2D port is excited with a sinusoidal signal to determine the distribution of electromagnetic components tangential to the port plane, commonly called "mode template".
3. Afterwards, the original 3D circuit is excited with the already pre-processed mode template multiplied by the user-defined time-varying signal (sinus, pulse, Gauss, etc.).
4. Eventually, during the simulation run, a scattering matrix is iteratively calculated at the reference planes shifted a few FDTD cells into the circuit with respect to the considered ports.

The advantage of using the aforementioned procedure is the possibility to excite and scan each waveguide mode independently. Thus, one may analyze and control the power distribution on all modes and between them.

The goal of this work is not to investigate the mode template generation in its classical form since it was thoroughly developed some years ago [**6**]. The aim is rather to show that the mode template computation may be extended to V2D FDTD circuits with periodic boundary

conditions applied. As it will be further shown, it will be a useful tool in the modeling of EM wave scattering from periodic structures.

The algorithm of looping periodic boundary conditions is exactly the same as for 3D FDTD circuits (see Chapter **3**.2). Let us first consider 22mm x 10mm rectangular air-box set in the *xy*-plane and discretized with 0.5mm FDTD cell size, assuming that the modes with zero longitudinal phase constant (β_f = 0 rad/mm) and zero phase shift per period along the *x*-axis (ψ_x = 0 rad) are searched for. The model is terminated with PEC boundaries along the *y*-axis. Such boundary conditions clearly indicate that the only possible propagation is along periodicity, that is *x*-axis. Thus, exciting the circuit with E_y polarized point source, the associated H_z magnetic field component can be expected.

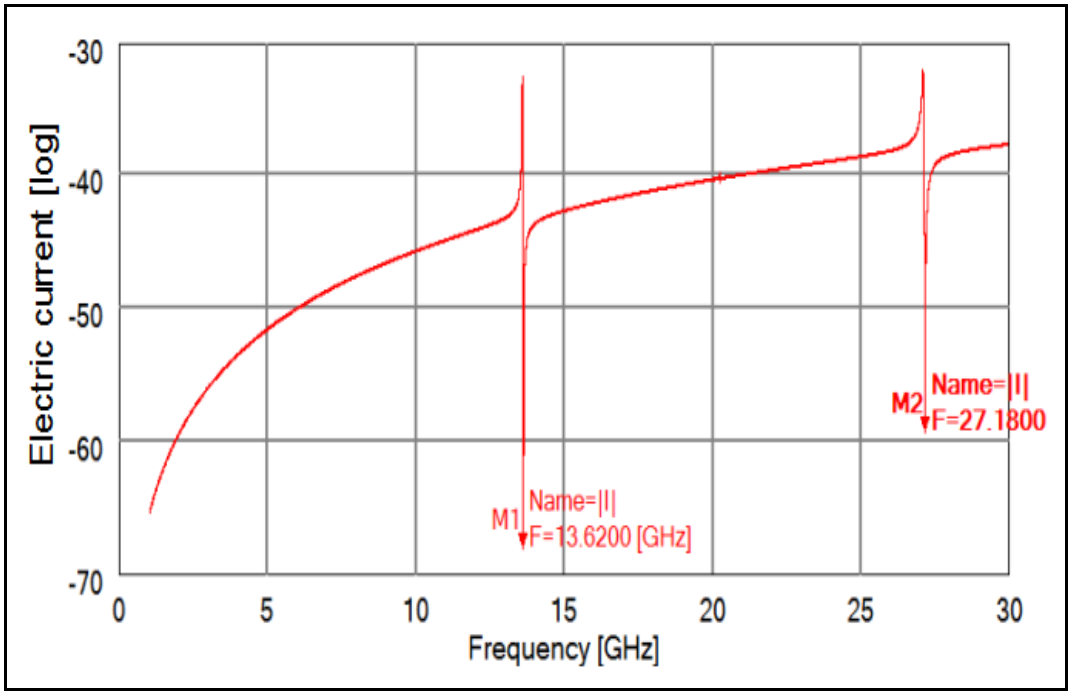

Fig.3.15. Spectrum of the electric current injected into a rectangular air-box (ψ_x = 0 rad, β_f = 0 rad/mm).

Due to the chosen source polarization and the boundary conditions imposed on the circuit, the first propagating mode can be expected to be of TEM kind operating at the wavelength equal to the period of the circuit, that is λ_0 = 22 mm (f_0 = 13.64 GHz). Indeed, spectrum of the impulse response of the considered scenario, shown in Fig.3.15, confirms with 0.15% accuracy the theoretical prediction, whereas field distribution of relevant components snapped at this frequency ensures that this is a TEM mode propagating along the *x*-axis (see Fig.3.16). Similarly, the next mode is supposed to propagate at f_1 = 27.27 GHz corresponding to the

wavelength twice shorter than the circuit period, i.e. λ_1 = 11 mm. Obviously, it also satisfies periodic boundary conditions but with a phase shift $\psi_x = 0 + 2\pi$. The discrepancy between the obtained result and theoretical calculation is somewhat larger than for the previous mode and amounts to 0.33% – apparently due to inherent dispersion of the FDTD algorithm increasing with frequency.

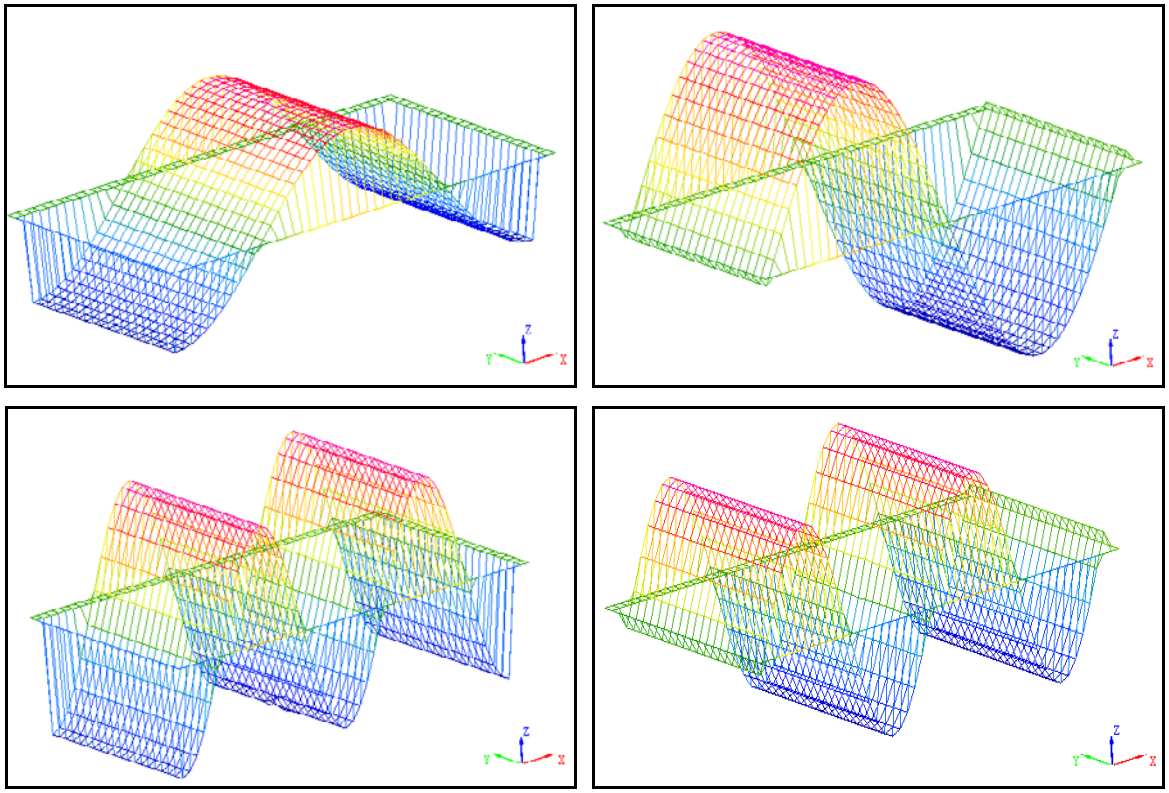

Fig.3.16. Snapshots of the electric E_y (left column) and magnetic H_z (right column) components at both f_1 = 13.62GHz (top row) and f_2 = 27.18GHz (bottom row) modes indicated in Fig.3.15.

Such a canonical example was introduced to test validity of the V2D FDTD algorithm coupled with periodic boundary conditions. Yet, it is still needed to be verified how it will operate for a nonzero longitudinal phase constant. Let us consider the same geometry, but this time the objective is to obtain an oblique propagation of E_y polarized plane wave at $\alpha = 60^0$ angle counted from the longitudinal *z*-axis. The operating frequency is equal to f = 20 GHz. The well-known relation:

$$\beta^2 = \beta_x^2 + \beta_y^2 + \beta_z^2 \tag{3.19}$$

can be used to determine both the longitudinal phase constant β_f and the phase shift per period ψ_x. In the considered case, there is no phase variation along the *y*-axis, so $\beta_y = 0$ rad/mm. The longitudinal phase constant β_f used in the V2D FDTD algorithm corresponds directly to β_z, whereas the fundamental phase shift per period is given by $\psi_x = \beta_x L_x$. Thus, knowing the frequency and the incident angle, it can be determined that:

$$\beta_f = \beta_z = \beta\cos(\alpha) = 0.20944 \; rad/mm \tag{3.20}$$

$$\psi_x = \beta_x L_x = \beta\sin(\alpha) L_x = 7.9807 \; rad \tag{3.21}$$

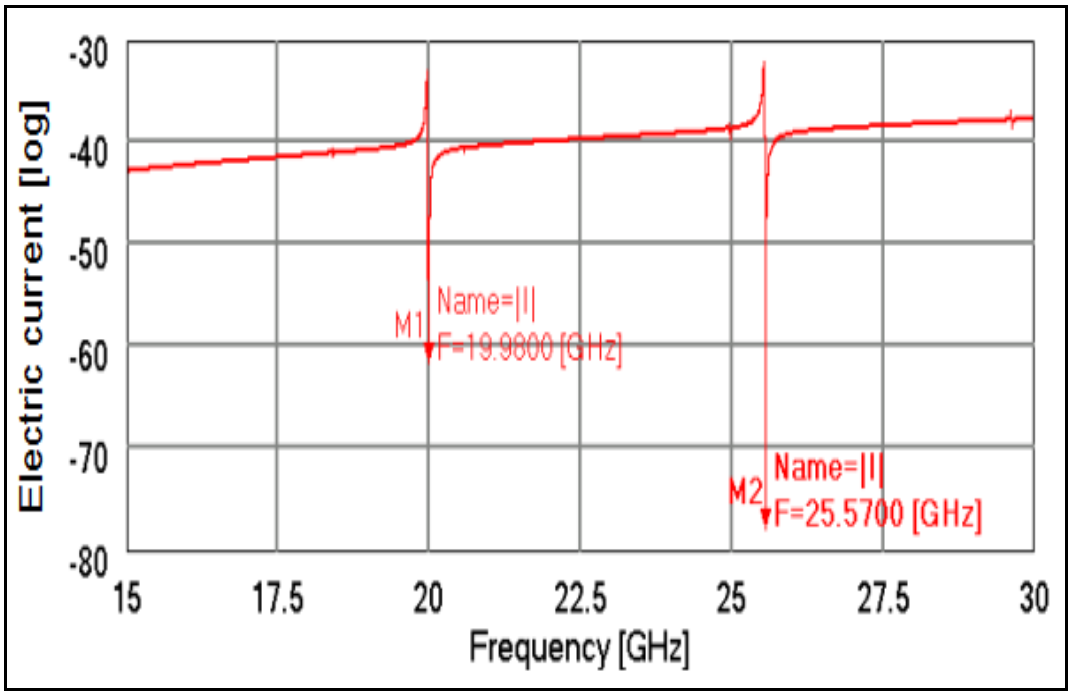

Fig.3.17. Spectrum of the electric current injected into a rectangular air-box (ψ_x = 7.9807 rad, β_f = 0.20944 rad/mm).

Fig.3.17 indicates resonance at the frequency f = 19.98 GHz (λ = 15.01 mm), which is 0.1% lower than anticipated. The distribution of the electric field component E_y at that frequency is shown in Fig.3.18. The measured wavelength along the *x*-axis is equal to λ_x = 17.4 mm, so by applying Eq.**3**.21, it can be derived that the angle of incidence equals to $\alpha = 59.6^0$. In fact, major contribution to the obtained discrepancy of 0.67% follows from the uncertainty of the wavelength measurement due to finite discretization of the FDTD model. Dispersion of the FDTD algorithm is at least one order of magnitude smaller since 30 FDTD cells per considered wavelength have been applied.

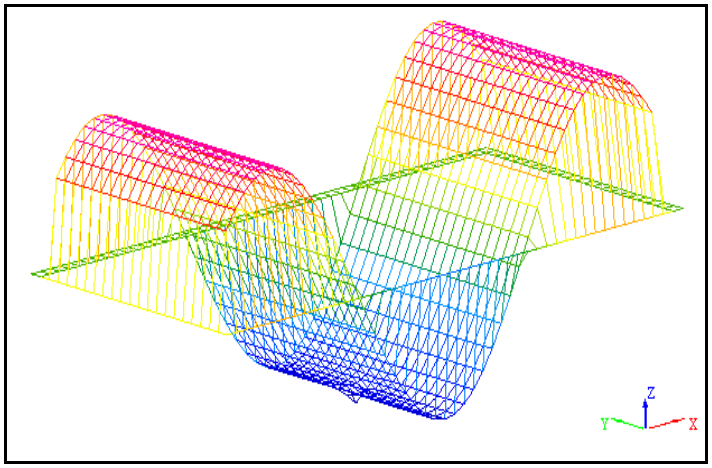

Fig.3.18. Snapshot of the electric component E_y at f_1 = 19.98GHz for the mode indicated in Fig.3.17.

The analysis presented above confirms the possibility of using periodic boundary conditions in a V2D FDTD model. The investigation of this will be recalled again in the next Chapter, when modeling of the scattering from periodic structures will be addressed.

3.5 FDTD Modeling of Scattering from Periodic Structures

The next issue has been under thorough investigation by the author of this dissertation during his studies and concerns the phenomenon of electromagnetic wave diffraction on a periodic structure. In principle, this is no longer an eigenvalue problem but a deterministic one since the structure is exposed to an independent external source of EM radiation. The author's interest in this subject results from the recent dynamic development of sophisticated metrology methods based on the diffraction phenomenon, where the FDTD method has found its application. As an example, let us recall here a scatterometry technique [**49**] commonly applied to the measurement and control of characteristic features during the lithography process of integrated circuits (IC) of large-scale integration (LSI). Another example refers to the frequency selective structures (FSS) exploited as selective-angle antennas or reflective surfaces [**50**]. Let us point out an advantage of the CL-FDTD algorithm in the modeling of the aforementioned scattering problems. Solutions for some practical scenarios will be shown in comparison to the other numerical methods, such as Finite Element Method Time-Domain (FETD) [**51**] or Rigorous Coupled Wave Analysis (RCWA) [**52**].

In general, the problem of electromagnetic wave scattering from a periodic structure may be split into four separate cases:

1. infinite structure and infinite spot,
2. finite structure and infinite spot,
3. infinite structure and finite spot,
4. finite structure and finite spot.

To be precise, the assumption imposed in the fourth case is always true in the real problems, but often leads to impractically large requirements for computer resources. Therefore, other approaches may be some interesting alternatives provided that the achieved speedup is not at the cost of accuracy of the final solution. For the purpose of this thesis, all mentioned approaches will be addressed to assess their computational capabilities and a range of applicabilities, except the third one since it has already been investigated in [**42**],[**43**].

Let us first specify some useful notions. Fig.3.19 illustrates a definition of two polarizations which will be exploited in the modeling of scattering phenomenon:

- TE (σ) with an electric field transverse to an incidence plane,
- TM (π) with a magnetic field transverse to an incidence plane.

It should be emphasized that the aforementioned notation of an EM wave polarization used for the scattering problems, often applied in the scatterometry, differs from the definition known in the analysis of eigenvalue and waveguiding problems.

Both incident (α_{inc}) and reflection (α_m) angles are measured from the normal (see the dashed line in Fig.3.19). It is often assumed in the analysis of diffraction gratings, such as the one shown in Fig.3.19, that the angles on the left-hand side of the normal are positive, whereas those on the right-hand side are negative. Let us recall that if a ray illuminates a periodic structure at a particular angle of incidence it may be reflected not only at the specular angle $\alpha_0 = -\alpha_{inc}$, also called 0^{th} diffraction order. There may also occur non-evanescent higher diffraction orders (m = 1, 2…). A reflection angle of the m^{th} diffraction order can be determined reminding that, in general:

$$\sin(\alpha_m) = \frac{\beta_{xm}}{\beta} \tag{3.22}$$

where $\beta_{x\,m}$ denotes the phase constant component along the x-axis of the m^{th} diffraction order.

Then, following Eq.**3**.18, a Bragg condition can be obtained:

$$\sin(\alpha_{inc}) + \sin(\alpha_m) = m\frac{\lambda}{L} \tag{**3**.23}$$

provided that $\beta \geq \beta_{x\,m}$.

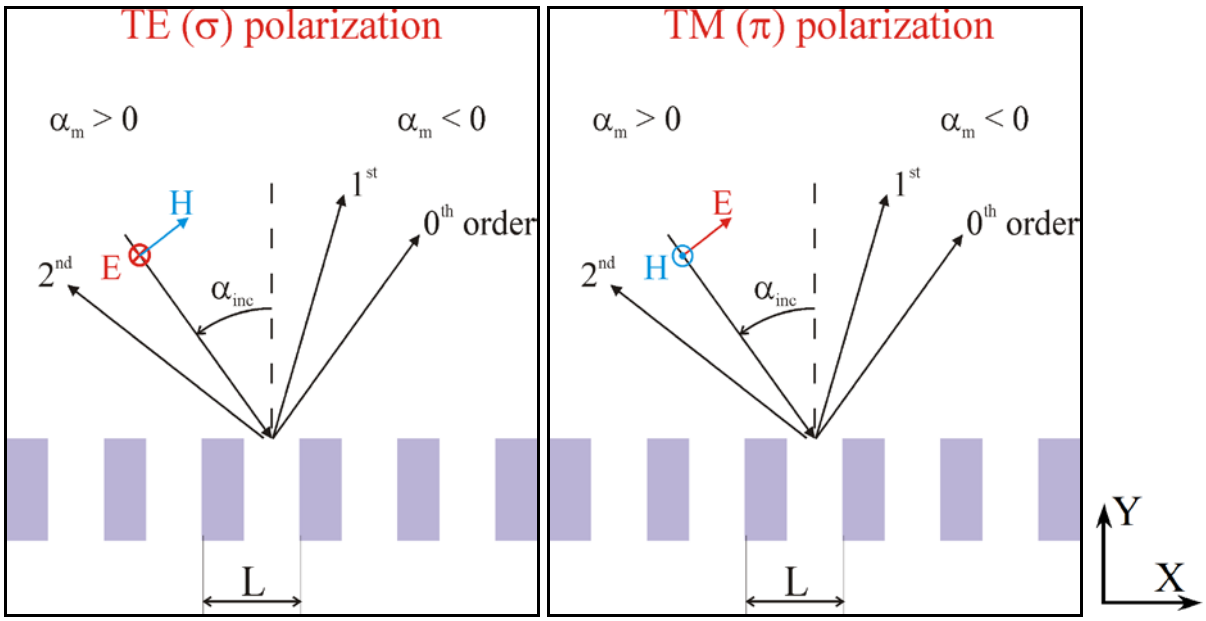

Fig.3.**19. TE (left) and TM (right) polarization of an incident wave.**

It will be later shown that the aforementioned equation may be derived directly from the Floquet theorem. Eq.**3**.23 refers to the 1D case and indicates that higher diffraction orders can appear when the operating wavelength λ is short enough and becomes comparable with the fundamental period of the structure L. Moreover, as the angle of incidence increases, more diffraction orders may be observed. Let us recall, as an example, scattering of light ray from a solid crystal bulk. Only specular reflection can be observed since the lattice constant (L < 0.5nm) is of the order of magnitude smaller than the shortest wavelength in the visible spectrum region (λ > 400nm). However, when using X-ray with the wavelengths comparable

to the lattice constant of a crystal, higher diffraction orders will be observed. Observation of these higher diffraction orders is often used to determine the lattice constant of crystals.

In Section **3**.5.1, an approximate case will be considered, namely an infinitely periodic structure illuminated with an unbounded plane wave at a particular angle of incidence (AOI) and of a specified polarization. A few FDTD models, useful in analysis of that case. will be proposed. Subsequently, Section **3**.5.2 will be focused on a more realistic case, that is, on the illumination of a periodic structure with a Gaussian beam. Obtained solutions will be cross-compared with the ones obtained for the infinite case.

3.5.**1 Plane Wave Illumination of Periodic Structures**

3.**5.1.1 Plane Wave Source over Infinitely Periodic Structure**

To begin with, let us make a remark that although illumination of an infinitely periodic structure with an unbounded plane wave is a rather unrealistic problem, this kind of approach is often successfully exploited for at least two reasons. Firstly, due to limited capabilities of state-of-the-art computing machines, periodic structures are often too large to be directly modeled in an efficient way. Secondly, sometimes the illumination area (spot) covers tens or even hundreds of the fundamental periods of the structure. An approximation of such a problem by an infinitely periodic structure illuminated with an unbounded plane wave leads to a relatively small error. It will be shown under what circumstances such an approximate approach may be reasonably employed.

The objective is to generate a purely traveling plane wave, exposing an infinitely long periodic structure at a particular angle of incidence. The method that generates the plane wave has to be properly coupled to the periodic boundary conditions implemented in the CL-FDTD algorithm. First, let us consider a structure periodic only along the *x*-axis (see Fig.3.20). Complex notation of an incident plane wave is given as follows:

$$\begin{aligned}\underline{\vec{E}}(x,y) &= \vec{E}_{re}(x,y) + j\,\vec{E}_{im}(x,y) = \vec{E}_0\, e^{j(\omega t - \hat{k}\vec{r})} = \vec{E}_0\, e^{j(\omega t - k_x x - k_y y)} = \\ &= \vec{E}_0 \cos(\omega t - k_x x - k_y y) + j\,\vec{E}_0 \sin(\omega t - k_x x - k_y y)\end{aligned} \tag{3.24}$$

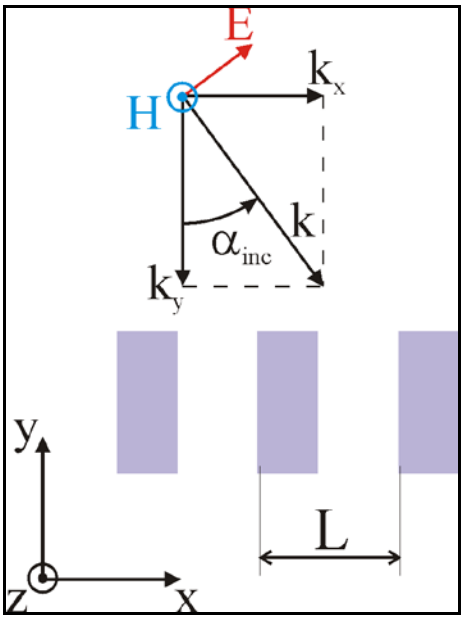

Fig.3.20. Oblique incidence of a plane wave in the *xy*-plane on the structure periodic along the *x*-axis.

Eq.3.24 indicates that in order to obtain a purely traveling plane wave, an imaginary FDTD grid has to be excited in quadrature to the real one. Thus, the following delay between the excitation of both grids has to be imposed:

$$\Delta t = \frac{T_0}{4} = \frac{1}{4 f_0} \tag{3.25}$$

In consequence, on both grids the plane waves shifted by the quarter of wavelength should be observed. Fig.3.21 shows the proposed FDTD model of plane wave generation in a scenario with periodic boundary conditions. The model is truncated with Mur superabsorption at the top and at the bottom. Below the top superabsorption, there is a wall defined along the whole length of the model, where the plane wave is supposed to be excited downwards. Furthermore, below the plane wave wall (PLW) in a total field region, another wall is set, sometimes called a “Huygens surface”, where near to far (NTF) field transformation is to be performed. It allows watching both incident and scattered rays. In QuickWave-3D commercial software package [**48**] used for that analysis, the direct Fourier transform (DFT) is applied instead of the fast Fourier transform (FFT), commonly used for the NTF transformation. As a result of that kind of approach, the user can easily control convergence of the solution as the simulation continues. If the aim is to consider the TE (TM) polarization,

the FDTD model can be reduced to one layer of cells placed between PEC (PMC) boundaries. Such a simplification of the model is allowed only if both the geometry of the structure, and an EM field are invariable in the direction perpendicular to the incidence plane.

The appropriate value of the Floquet phase shift per period imposed at the PBCs has to be synchronized with the excited plane wave. It can be easily noticed that the following assumption has to be satisfied:

$$\psi_x = k_x L = k \sin(\alpha_{inc}) L \tag{3.26}$$

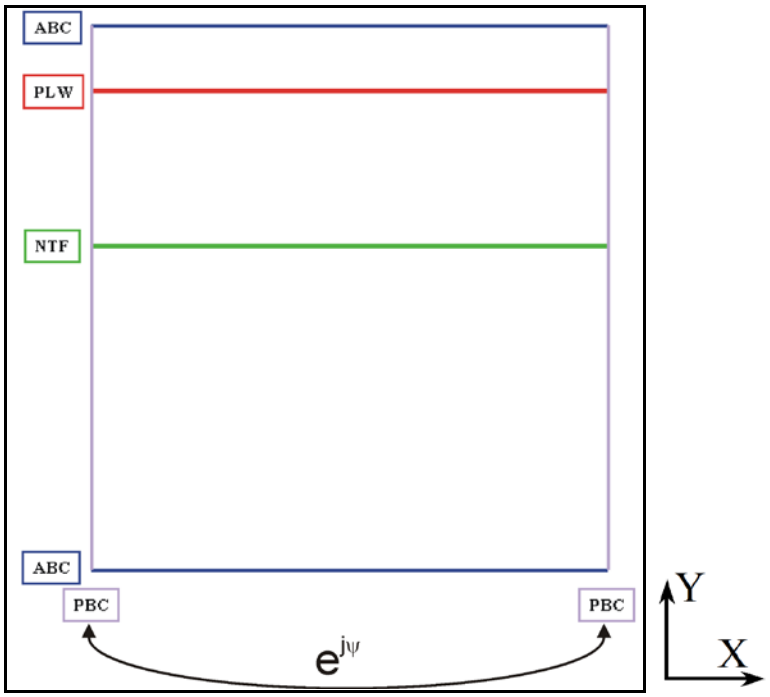

Fig.3.21. FDTD model for an oblique plane wave incidence on the structure periodic along the *x*-axis.

In order to evaluate the considered model, let us assume that the aim is to generate a plane wave at f = 10 GHz, incident at $\alpha = 30^0$, in the L = 40 mm long vacuum box. At this stage, no obstacles are placed inside the model to observe undisturbed plane wave propagation, so only incident ray is expected to appear in the far field scattering pattern obtained by the NTF transformation. According to Eq.3.25, an imaginary FDTD grid has to be excited with a delay equal to dt = 0.025 ns with respect to the real FDTD grid. As regards periodic boundary conditions (see Eq.3.26), the Floquet phase shift per period has to be set to ψ_x = 4.188 rad. Eventually, a traveling plane wave can be generated in the model, shown in Fig.3.21. Fig.3.22

shows the electric field distribution on both the real and imaginary FDTD grids snapped at the same time instant. Looking carefully on both snapshots, it can be noticed that the plane waves are indeed shifted by the quarter of the wavelength with respect to each other. Nevertheless, it should be emphasized that the CL-FDTD method is frequency selective, in a sense that a wideband excitation will not produce a traveling plane wave in the whole band due to the unsatisfied Floquet phase condition for the frequencies different than the matched one. This is the main limitation of the method. More discussion of these issues will be presented later in this thesis.

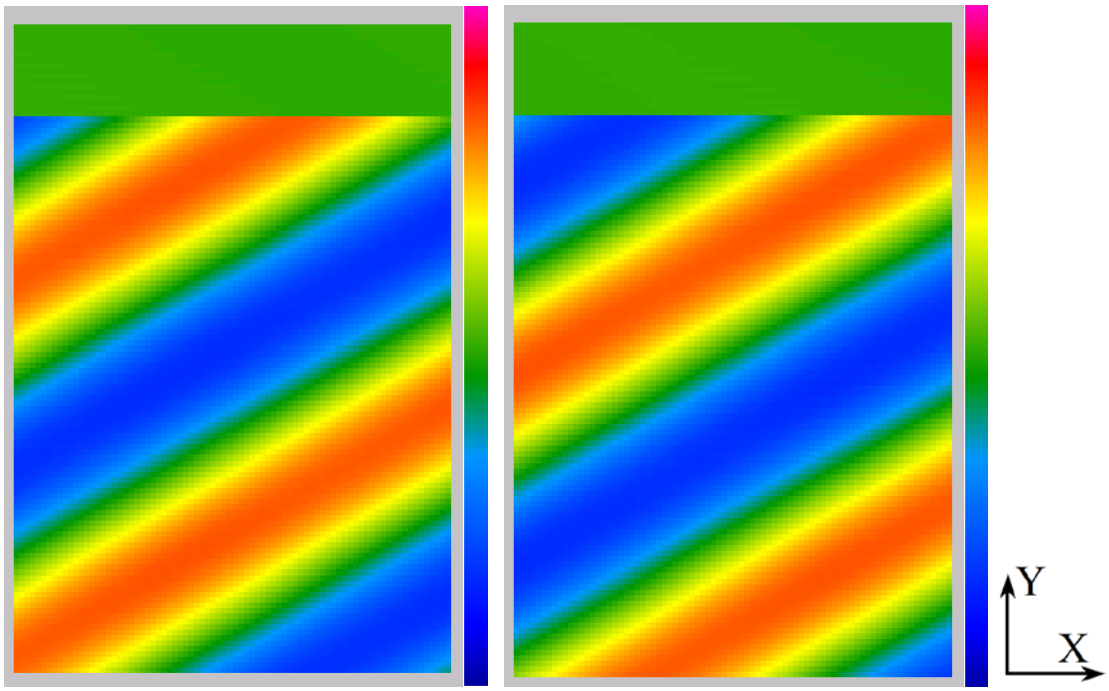

Fig.3.22. Plane wave illumination at the real (left) and imaginary (right) FDTD grids at f = 10GHz, incident at $\alpha_{inc} = 30^0$, snapped at the same time instant.

Now, in order to evaluate the diffraction of a plane wave from a periodic structure we can place it inside the proposed model. However, one should be aware that – according to Fig.3.21 – reflection coefficient is extracted with the aid of the NTF transformation. Thus, there is still the issue, how to understand the scattering pattern obtained from NTF computation. In principle, a far-field radiation beam of an infinite plane wave is of Dirac delta shape since the angle of incidence of such infinite beam is exactly defined. However, due to the fact that an NTF surface is exactly equal the length of the FDTD model, calculated beams will be significantly broadened. From a mathematical point of view, obtained beam is a convolution of a window function and the Dirac delta. In that case, the window function

reflects the spatial length of the NTF surface applied in the model shown in Fig.3.21. Therefore, it should be determined whether a finite length of the NTF surface disturbs the extraction of incident and reflected beams in the scattering pattern.

Let us assume that the aim is to excite a plane wave at a particular frequency *f*, incident at the angle α_{inc}, in the periodic model of length *L*. Following Eq.3.26, a proper Floquet phase shift per period ψ_x can be set. Thus, a generated plane wave has the following form (compare Eq.3.24):

$$\underline{\vec{E}}(x,y) = e^{j(\omega t - \beta_{x0}x - \beta_{y0}y)} \tag{3.27}$$

where

$$\beta_{x0} = \beta \sin(\alpha_{inc}) \tag{3.28}$$

$$\beta_{y0} = -\beta \cos(\alpha_{inc}) \tag{3.29}$$

The far-field scattering pattern is calculated at the NTF level in the following way:

$$\underline{\vec{E}}(\alpha) = \int_{-L/2}^{L/2} \underline{\vec{E}}(x,y) e^{-j\beta \sin(\alpha)x} dx \tag{3.30}$$

Substituting Eqs.3.27-29 to Eq.3.30 and solving the given integral, the following formula can be obtained:

$$\underline{\vec{E}}(\alpha) = e^{j(\omega t - \beta_{y0} y)} L \frac{\sin(w)}{w} \tag{3.31}$$

where

$$w = \pi \frac{L}{\lambda} [\sin(\alpha_{inc}) + \sin(\alpha)] \tag{3.32}$$

Eventually, it can be noticed from Eq.3.**31**,**32** that zeros of the far-field scattering pattern are obtained if and only if the following relation is satisfied:

$$\sin(\alpha_{inc}) + \sin(\alpha) = m\frac{\lambda}{L} \tag{**3**.33}$$

where $m = \pm 1, \pm 2, \ldots$

In principle, the above formula states a Bragg condition and enables us to evaluate higher diffraction orders (compare Eq.**3**.23). It proves that the incident beam in the scattering pattern, though broadened, does not disturb values at higher diffraction angles since they appear exactly at the minima of the incident beam extracted using NTF transformation. The same investigation may be performed to make sure that the higher diffraction rays do not interfere with each other as well. To conclude, it has been formally proven that as long as NTF transformation is computed over a length equal to the multiple of the fundamental period of the structure, only discrete points in the scattering pattern which satisfy Eq.**3**.33 are calculated without any interference. Moreover, increase of NTF length L results in narrower beams and raising maxima. In consequence, NTF transformation executed in CL-FDTD model provides – within numerical accuracy of the method – exact values of the far-field electric field intensities at both incident and reflected angles.

To confirm the considerations carried out above, let us look at the angular scattering pattern processed by NTF transformation, shown in a logarithmic scale in Fig.3.23, and obtained for the empty air region already considered in Fig.3.22. The allowed diffraction angles are marked with vertical dashed lines. The angular variable ϕ used in the figures below is the azimuth angle in the *xy*-plane counted counterclockwise from the *x*-axis. It can be expected that an illumination beam appears at $\phi = 300^0$, what corresponds to $\alpha_{inc} = 30^0$, using the notion defined in Fig.3.20. It can be also noticed that, although the center of the incident beam is not exactly at 300^0, all minima fit exactly to the angles of potentially allowed higher diffraction orders. In particular, there is a significant minimum at $\phi = 60^0$, which corresponds to a specular reflection angle. If any obstacle is put inside the model, another beam centered at $\phi = 60^0$ will appear, but it will surely not disturb the value of the incident beam at $\phi = 300^0$.

Consequently, reflection coefficient, understood as the ratio of electric field intensities at 60^0 and 300^0 angles, will be calculated correctly.

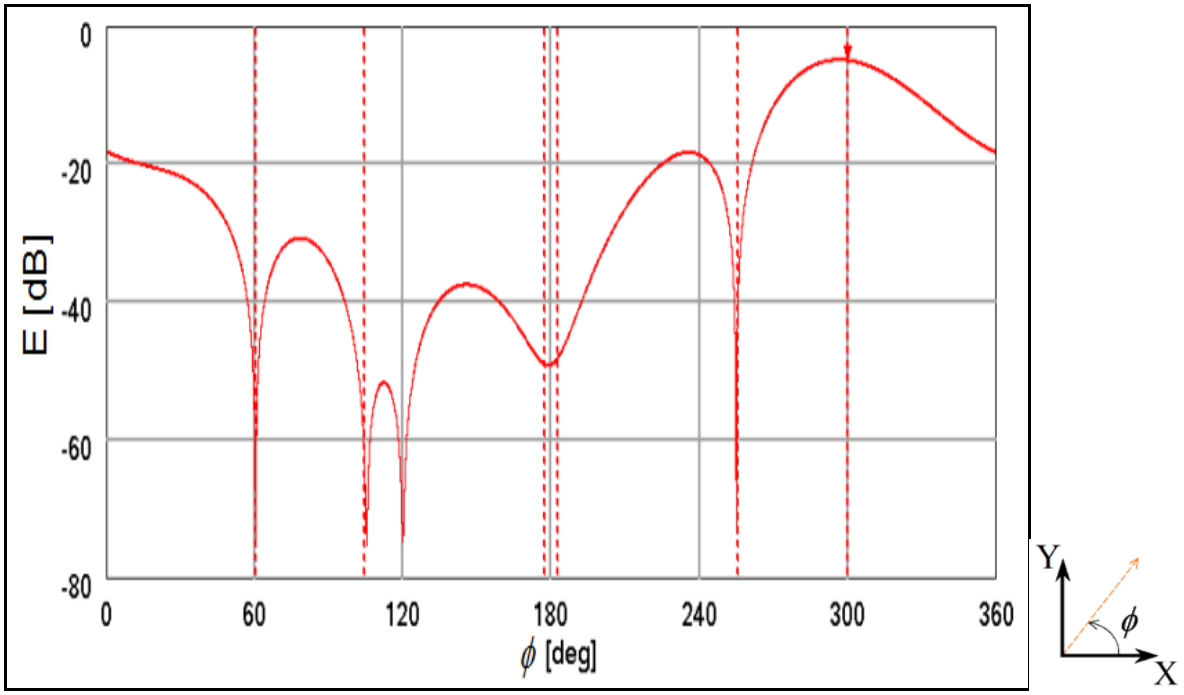

Fig.3.23. Scattering pattern shown in a logarithmic scale for the plane wave incident at α_{inc} = 30^0 (ϕ_{inc} = 300^0) in an empty air region (f = 10GHz, L = 40mm).

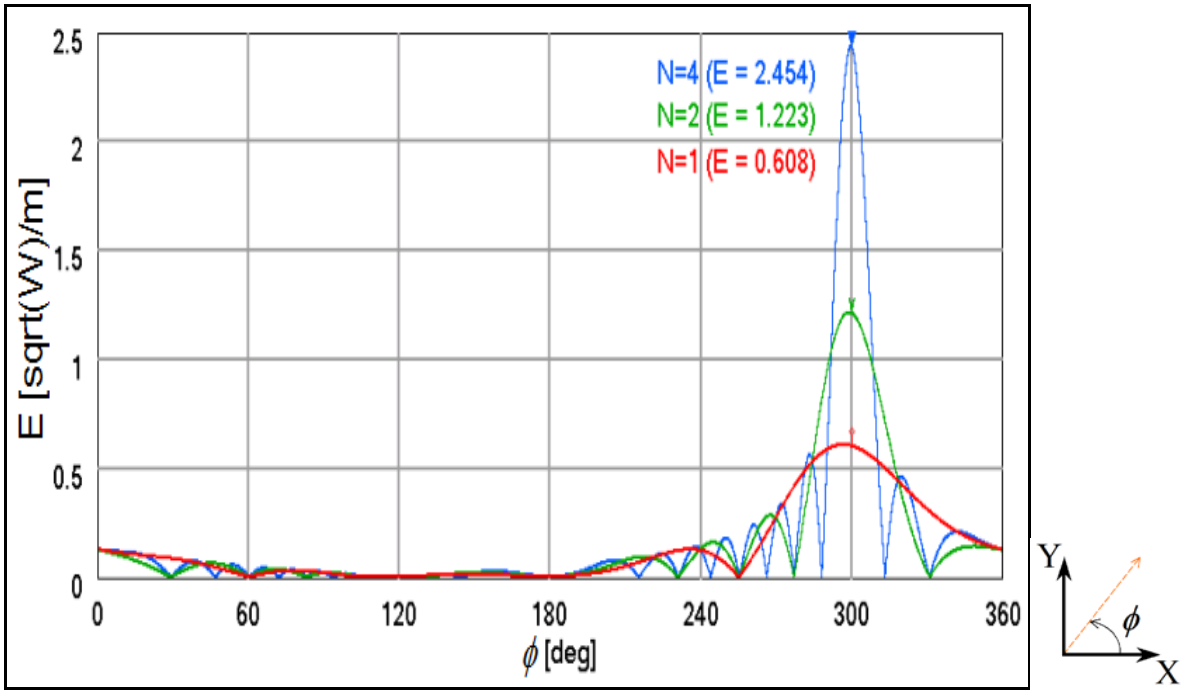

Fig.3.24. Scattering patterns for the plane wave incident at α_{inc} = 30^0 in an empty air region with a varying length L (f = 10GHz, L = N*40mm).

Table 3.1. Maximum electric field intensities of the incident beams shown in Fig.3.24.

N	$\lvert E\rvert$ @ $\phi = 300^0$ [$\sqrt{W}/m$]	$\Delta\phi_{3dB}$
1	0.608	42.2
2	1.223	21.8
4	2.454	10.9

Fig.3.24 illustrates what happens when NTF transformation is performed over one, two and four periods of the structure. Table 3.1 presents the maximum electric field intensities of incident beams with a growing number of structure periods and the corresponding 3dB beam widths. It confirms that the width of a beam is inversely proportional, and its height linearly varies with the length of NTF transformation surface. As anticipated before in this Chapter,the beam finally converges to the Dirac delta.

Let us now consider EM plane wave scattering from a particular periodic structure. Fig.3.25 shows the geometry of the scenario. It is a periodic set of crosses made of perfect electric conductor (PEC) buried in a dielectric (ε_1 = 2.56 ε_0). Fundamental period is equal to d = 100 mm. The objective is to expose the structure to a plane wave, incident at $\alpha_{inc} = 30^0$ within a range of d/λ_0 = 0 ... 1 and, afterwards, extract a specular reflection coefficient.

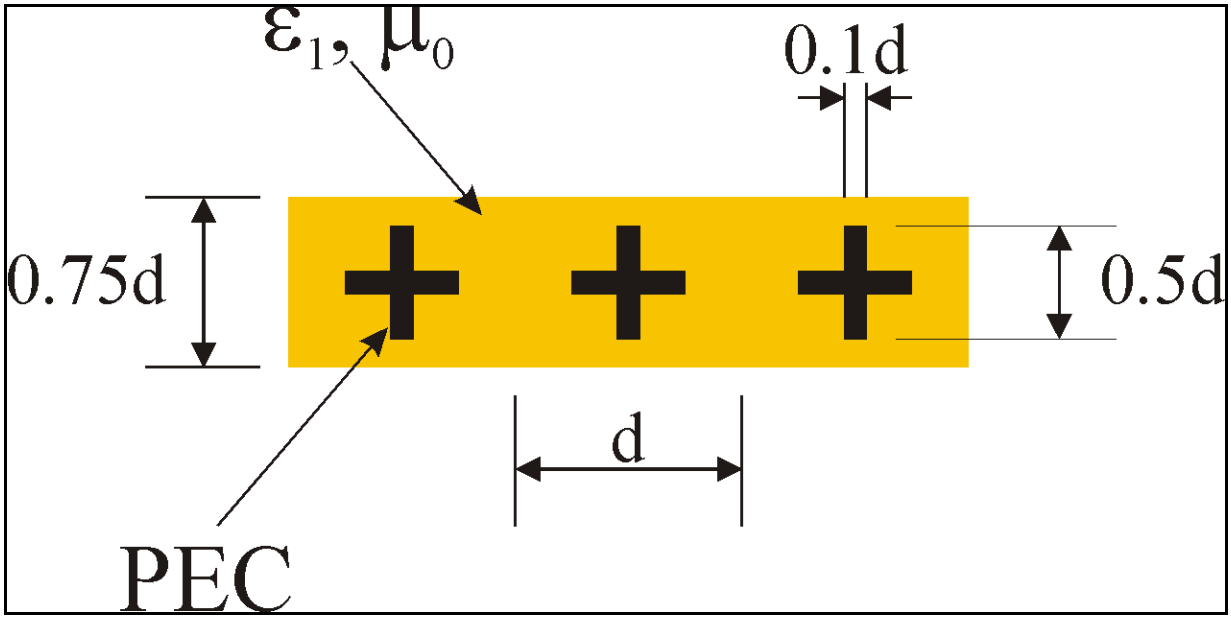

Fig.3.25. Dielectric coated PEC cross-shaped grating (d = 100 mm, ε_1 = 2.56 ε_0).

To speed up the simulation, the sinusoidal excitation is substituted with a narrowband pulse of finite duration centered at the considered frequency. Fig.3.26 shows the results of a number of FDTD simulations, marked with blue dots plotted on a red curve, obtained with the finite element time domain (FETD) method [53]. The simulation step amounts to dt = 1.667 ps, with FDTD grid size of a = 1 mm, whereas the simulation speed reaches 2000 iter/sec, resulting in the single simulation time of about t_p = 2.5 sec[3]. Total simulation time depends on the number of simulation points, but computational effort is very similar the one obtained with the FETD method. A distinct resonance can be observed at d/λ_0 = 0.83. It refers to the frequency for which the thickness of a dielectric slab (75mm) is close to the wavelength of a plane wave propagating downwards:

$$\lambda_y = \frac{2\pi}{\beta\sqrt{\varepsilon_1}\cos(\alpha_{inc})} = \frac{\lambda_0}{\sqrt{2.56}\cos(\alpha_{inc})} = \frac{d}{0.83\sqrt{2.56}\cos(\alpha_{inc})} \approx 87[mm] \qquad (3.34)$$

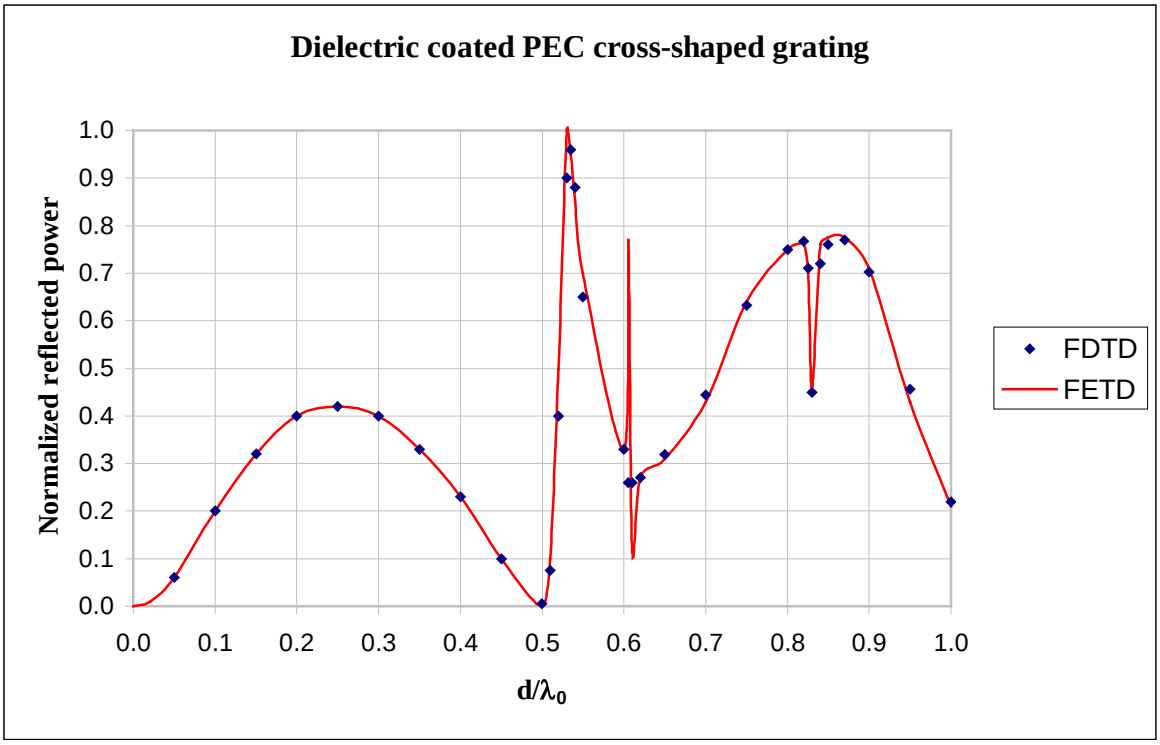

Fig.3.26. Specular power reflection from the dielectric-coated PEC cross-shaped grating (d = 100 mm, α_{inc} = 30^0) compared with the FETD method.

[3] Intel Core™2 Duo CPU 3.00GHz, 4094MB RAM, 64-bit Windows Vista Business.

It seems to be a full-wave resonance. Similarly, what can be easily verified, there is a half-wave resonance at d/λ_0 = 0.5. However, even with a very long computation and much finer meshing, it was not be possible to detect the resonance near d/λ_0 = 0.61. Supposedly, it was a spurious solution of the benchmarking FETD method which appeared in [53].

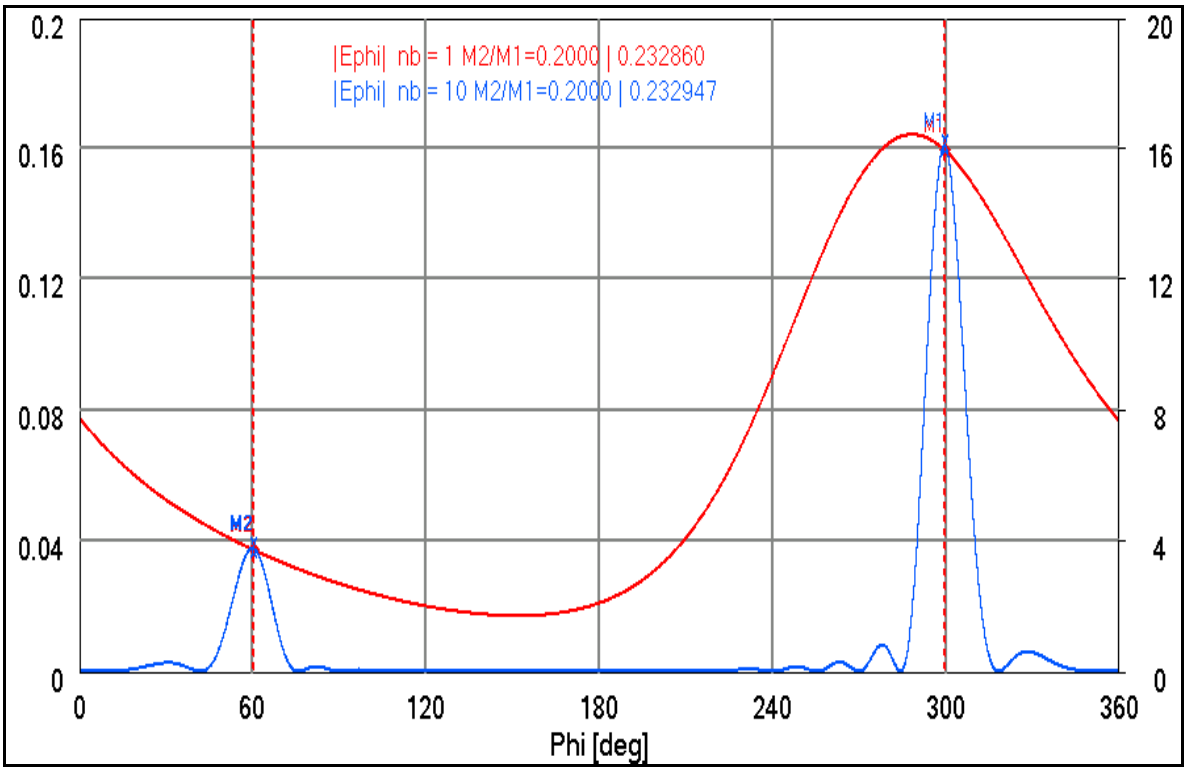

Fig.3.27. Angular scattering pattern in power scaling for the dielectric-coated PEC cross-shaped grating (d = 100 mm, $\alpha_{inc} = 30^0$, f = 1.2GHz) obtained in one (red) and ten (blue) periods model.

Table 3.2. Values taken from the angular scattering pattern shown in Fig.3.27.

N	$\lvert E\rvert^2 @ \phi = 60^0\ [W/m^2]$	$\lvert E\rvert^2 @ \phi = 300^0\ [W/m^2]$	R_P
1	0.037417	0.160685	0.23286
10	3.778596	16.220854	0.23295

Let us now observe the angular scattering pattern (ASP) for d/λ_0 = 0.4, obtained using NTF transformation performed in two models which consist of one and ten fundamental periods of the considered grating structure. Fig.3.27 clearly indicates that for the one-period model (the red curve and the left scale) – due to a relatively

short length of the model – ASP is substantially broadened, so it is hard to distinguish incident and reflected beams. Nevertheless, comparison with the ten-period case (the blue curve and the right scale) shows that, though the shape of ASP may be somewhat confusing, it provides accurate values at the diffraction angles (compare Eq.**3**.33).

The values presented in Table **3**.2 indicate that the difference between the specular power reflection coefficients obtained in both short and long models is about 0.01%, mainly due to the discrete FDTD meshing. Moreover, it can be also noticed that the intensities of incident and reflected beams are ten times higher in the model consisting of ten periods of the structure, which is a direct consequence of ten times wider domain of integration.

Now, let us return to the issue of narrowband properties of the plane wave excitation model implemented in the CL-FDTD algorithm. As it has been mentioned earlier, undisturbed traveling plane wave in a periodic structure can be obtained only for a discrete frequency. In consequence, to obtain a reflection coefficient in the specified spectrum range, as shown in Fig.3.26, several simulations have to be run for consecutive frequency points. Let us look for the possibilities of alleviating such a strict condition. The considered dielectric-coated PEC cross-shaped grating will be excited with a wideband pulse and the reflection coefficient will be extracted in the vicinity of the matched frequency, in order to assess the reflection coefficient error introduced by imperfect plane wave excitation.

Fig.3.28 presents the simulation results obtained for the dielectric-coated PEC cross-shaped grating at a few frequency sub-bands. Most of all, it can be noticed that discrepancies are not systematic, so it is hard to draw general conclusions about inaccuracy. Nevertheless, it can be concluded that the deviation from the matched frequency by more than about 2-3% is not acceptable if accuracy of the obtained result is expected to be less than 5%. In consequence, there is not much room to maneuver, especially when considering a real electromagnetic design, where the aim is usually to achieve accuracy much below 1%. It brings us back to the starting point, that is, to the single frequency approach.

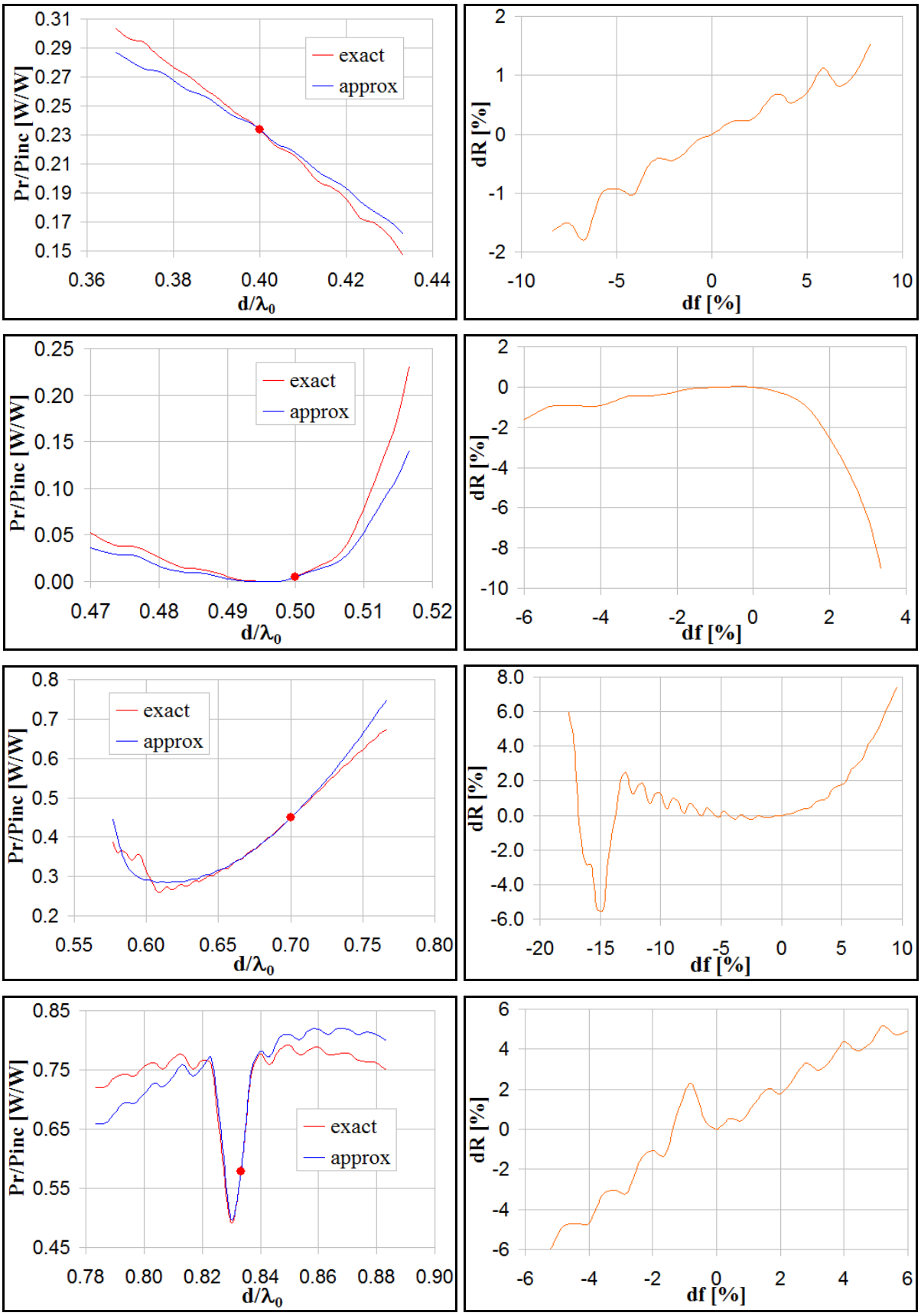

Fig.3.28. Specular reflection (blue curve), as shown in Fig.3.26, compared with a wideband data collection (red curve) matched only at a single frequency marked with dots.

Figures in the right column show relative discrepancy between both curves in the left column.

Now, let us consider another example of 1D periodic structure, showing a little different scope of potential applicability for the CL-FDTD algorithm. This time, a so-called poly-to-active stack [54], composed of two diffraction gratings and processed in different layers on a silicon wafer during a lithography process of integrated circuits (IC), will be considered (see Fig.3.29). These kinds of stacks are exploited as test targets in a scatterometry technique [49], applied to control accuracy and precision of the lithography process.

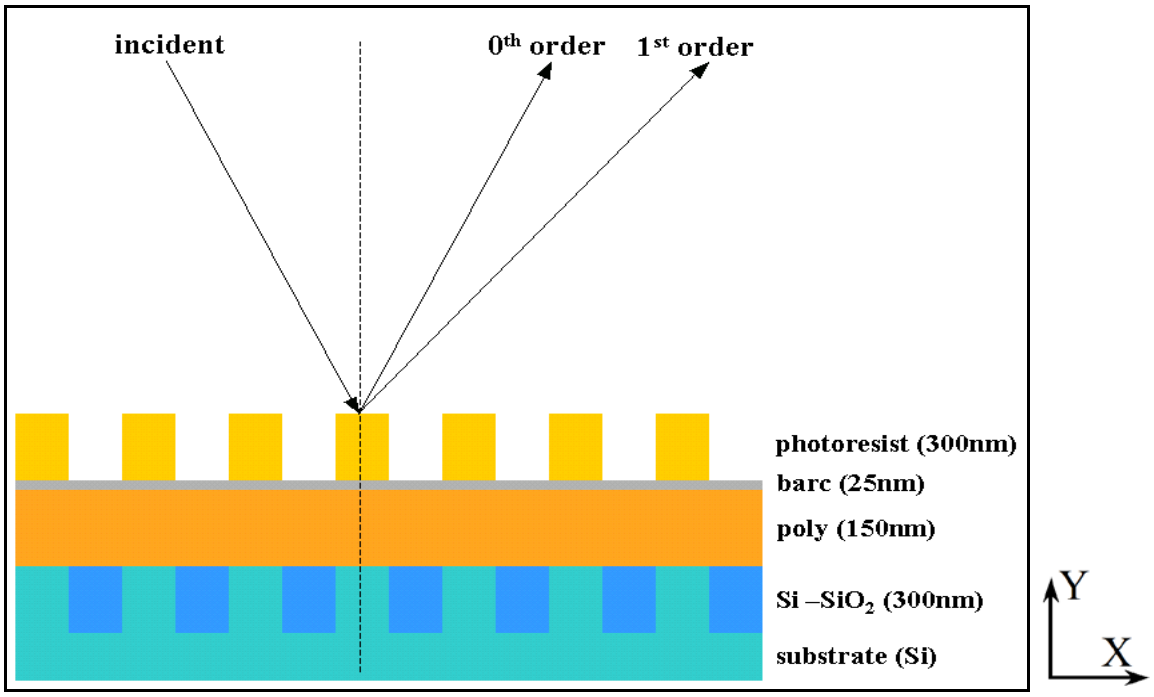

Fig.3.29. Cross-section view of a poly-to-active stack.

In principle, scatterometry is a very interesting method, which is very useful when the dimensions of features processed with the lithography are much below the resolution limit of imaging techniques. The idea of scatterometry is to expose a target to a ray of bright light incident at a particular angle and, afterwards, to collect the spectrum of reflection coefficient (usually specular one), which is supposed to contain information about the geometry of the illuminated target. It may be the width of a line or a trench, the shift (overlay) between layers processed on a wafer, etc. However, to increase the signal to noise ratio (SNR) of the scatterometry technique, the target is usually periodically repeated to enhance the gain of the reflected ray. Thus, the length of the target is of the order of tens of microns – depending mainly on the diameter of the illumination spot. In the example below, a TE polarized plane wave (see Fig.3.19) incident at the angle of 25^0, on a target with the fundamental period (pitch) of 320nm, will be investigated. The width of the lines and the trenches, sometimes

denoted as the critical dimension (CD), is equal to 160 nm. Material properties have been obtained by private communication with KLA-Tencor Israel [55]. They cannot be disclosed here, however, similar data may be found in professional literature [56]. For the purpose of this analysis, an incidence plane is supposed to be perpendicular to the trenches. Moreover, since the aim is to investigate incident light of the spectrum from 500 up to 700 nm, according to Eq.**3**.23, only a specular reflection is allowed.

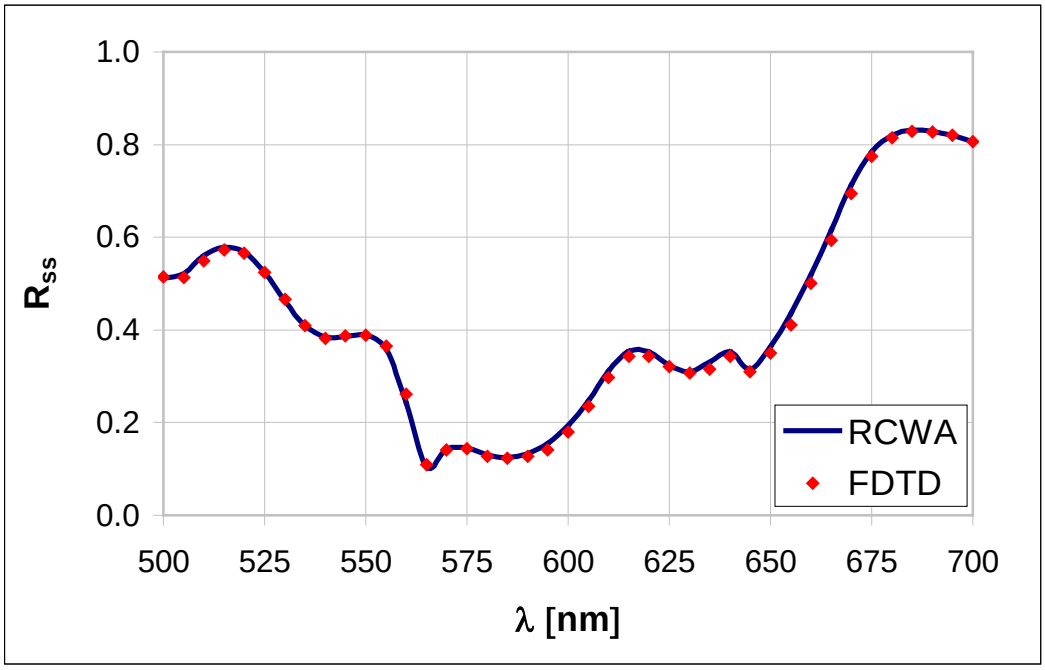

Fig.3.**30. Reflection coefficient for a TE polarized illumination incident at 25^0 on the target shown in Fig.3.29.**

Fig.3.30 depicts the reflection coefficient in the considered spectrum range obtained with the CL-FDTD algorithm, compared to the RCWA solution computed by KLA-Tencor [55]. The performed tests have shown that in this particular case the model should consist of at least two pitches to guarantee appropriate separation of incident and reflected beams in the angular scattering pattern calculated with the aid of NTF transformation. Fig.3.30 proves the mutual convergence of both methods in the whole considered spectrum – average discrepancy amounts to about 0.76%. In order to meet the challenging requirements for precision of the scatterometry technique, a 2nm FDTD cell size has been set, so as to have at least 50 cells per wavelength in the worst case (λ_0 = 500nm, poly). The simulation time step is dt = 0.004 fs. Such a fine meshing is necessary since the scatterometry technique is dedicated to the measurement of the overlay between gratings processed in different layers. The bottom

grating is often buried below some opaque material, such as poly or barc (see Fig.3.29), resulting in ill-conditioned algorithm for the overlay extraction. However, even with such a fine discretization, a simulation of one frequency point is relatively quick and the convergence is reached after 580 seconds, achieving the simulation speed of about 100 iter/sec[4]. Successful comparison of the new algorithm with the calculations performed using the RCWA method justifies the first statement of the thesis posed in Chapter 1.

The author of this thesis has been involved in a European project [57], where his aim was to develop and implement FDTD models applicable to the modeling of scatterometry of periodic structures. More details concerning this issue are omitted here and can be found in [49],[54],[58-60].

Now, let us consider an oblique incidence of a plane wave on a two-dimensionally periodic structure to verify the 2D PBC algorithm implemented by the author of this thesis[5]. First, relations between the Floquet phase shift per period in each direction and the incidence angle will be introduced. Let us apply a spherical coordinate system[6] to maintain generality of the notation. It should be emphasized that in the modeling of a plane wave scattering phenomenon, the Floquet phase shift per period along an arbitrary axis may be understood as the phase shift of the considered plane wave along one period of the FDTD model. Thus, the relevant formulae are as follows:

$$\psi_x = k_x L_x = k\,\cos(\phi)\sin(\theta)\,L_x \tag{3.35}$$

$$\psi_y = k_y L_y = k\,\sin(\phi)\sin(\theta)\,L_y \tag{3.36}$$

$$\psi_z = k_z L_z = k\,\cos(\theta)\,L_z \tag{3.37}$$

To exemplify the issue, let us consider an infinite set of 10mm x 10mm metal patches set in the *xy*-plane, located in an empty air region. The fundamental period is the same in both directions and amounts to 20mm. The goal is to illuminate these patches with a TE polarized plane wave (see Fig.3.19), of the frequency f = 20 GHz, and incident at (ϕ, θ) = (45^0, 135^0). The operating frequency imposes a delay between excitation signals of real and imaginary FDTD grids of dt = T/4 = 12.5 ps (see Eq.3.25).

[4] Intel Core™2 Duo CPU 3.00GHz, 4094MB RAM, 64-bit Windows Vista Business.
[5] See Appendix 1.
[6] See Appendix 3.

Two simulations with 1x1 and 2x2 arrays of metal patches will be performed – both with periodic boundary conditions imposed. For the purpose of this analysis, a 0.25 nm FDTD cell size has been set (60 cells/λ) to suppress potential problems with the numerical dispersion of the FDTD algorithm. Fig.3.31 depicts normalized scattering patterns obtained at the incident plane ($\theta = 45^0$). The specular reflection is accompanied by the 1st order one, appearing at (ϕ, θ) = (45^0, 339.3^0) (compare Eq.**3**.23). When inspecting the curve obtained for 1x1 model (red), one may notice a significant deformation of the beam. Nevertheless, comparison with the plot obtained for 2x2 array model (blue) once again confirms the theoretical findings presented earlier (see Eq.**3**.33) that the beam deformation due to a finite length of an NTF surface does not disturb the scattering pattern at the angles belonging to a set of diffraction orders. Comparing both characteristics plotted in Fig.3.31, the discrepancy of the reflection coefficient of the 0th order is about 0.11%, whereas for the 1st order, it amounts to 0.23% (see values in Table **3**.3).

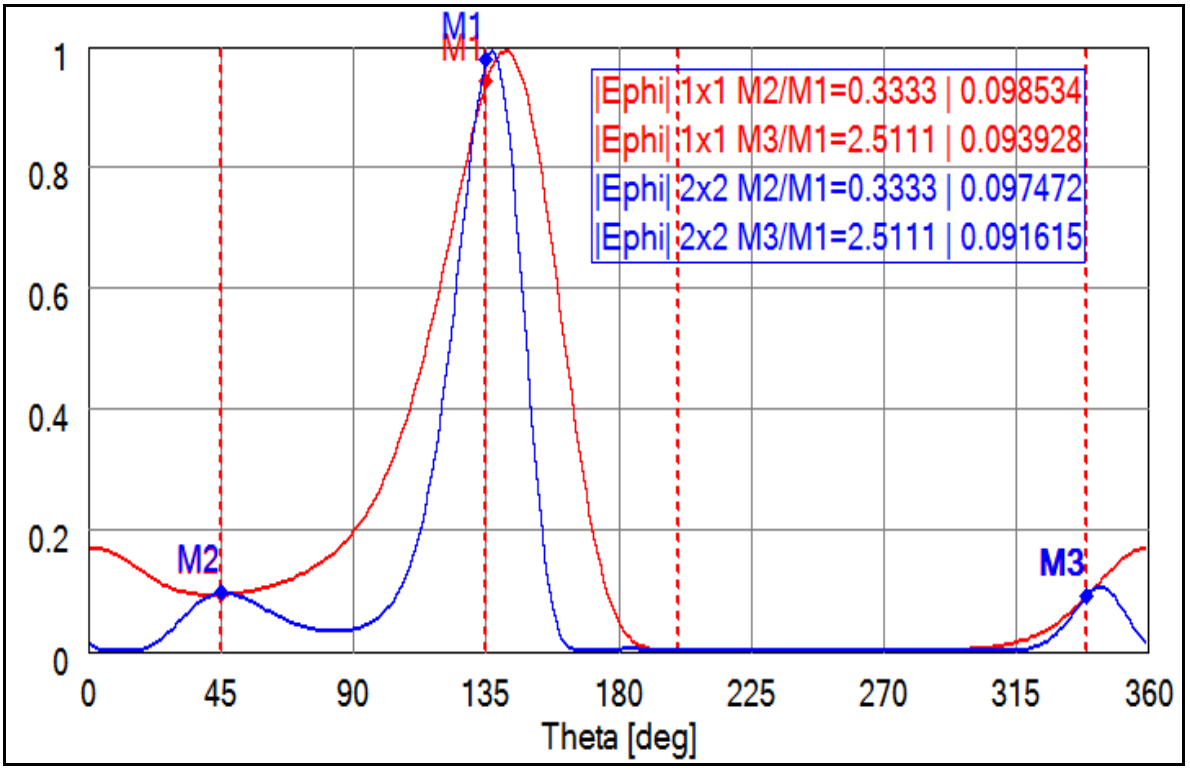

Fig.3.31. Angular scattering patterns (normalized power scaling) calculated in an incident plane for the infinite array of 10mm x 10mm metal patches modeled with 1x1 (red) and 2x2 (blue) matrix of patches.

Table 3.3. Values taken from the angular scattering patterns shown in Fig.3.31.

N	$\|E\|^2$ @ $\theta = 45^0$	$\|E\|^2$ @ $\theta = 135^0$	$\|E\|^2$ @ $\theta = 339^0$	R_P ($45^0/135^0$)	R_P ($339^0/135^0$)
1x1	0.093498	0.948897	0.089128	0.098534	0.093928
2x2	0.095949	0.984369	0.090183	0.097472	0.091615

To resume, extraction of the far-field angular scattering pattern due to a plane wave incidence has been discussed. The proposed approach allows evaluation of not only the specular diffraction from a periodic structure, but also possible higher diffraction orders. The author has successfully implemented and verified a plane wave source and a near-to-far transformation in the presence of periodic boundary conditions in the CL-FDTD algorithm, proving the first statement of the thesis posed in Chapter 1.

3.5.1.2 Waveguide Mode over Infinitely Periodic Structure

Now, let us introduce a different method applicable to the analysis of EM wave scattering from infinite periodic structures. An analogy to the wave propagation in a waveguide will be applied. Let us first remind that each $E(H)_{mn}$ mode in a rectangular waveguide has *a priori* known forward phase constant [61]:

$$\beta_{f\,mn} = \sqrt{\beta^2 - \beta_{c\,mn}^2} \tag{3.38}$$

where β stands for the phase constant in an unbounded region and $\beta_{c\,mn}$ is the cut-off of the considered mode. Each mode has a specified distribution of EM components in a waveguide cross-section, which does not depend on frequency. Such a distribution is usually called a mode template. It will be shown that such a mode template resembles a standing wave in an unbounded region.

Let us consider – without loss of generality – modes only of $E(H)_{m0}$ kind. For the sake of simplicity, notation of the indices *m0* in the subscripts below will be suppressed. Fig.3.32 illustrates decomposition of the phase vector β into the forward and transverse components. The corresponding incidence angle $|\alpha_{inc}|$ can be determined from the following formula:

$$\sin(|\alpha_{inc}|) = \frac{\beta_c}{\beta} = \frac{f_c}{f} = \sqrt{1-\varepsilon_{eff}} \tag{3.39}$$

where ε_{eff} denotes an effective permittivity and f_c is a cut-off frequency of the considered mode.

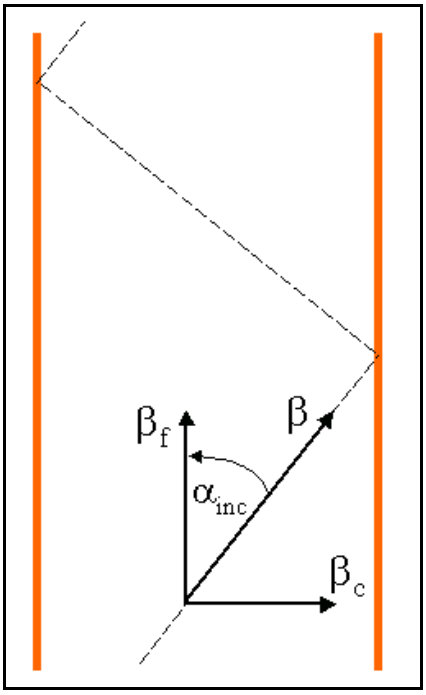

Fig.3.32. Plane wave representation of waveguide mode propagation.

Exactly the same field distribution can be obtained in any unbounded region exciting two plane waves propagating at $+\alpha_{inc}$ and $-\alpha_{inc}$ angles, producing, in consequence, standing wave distribution in the plane, transverse to the propagation. This conclusion will be employed to propose another method of simulation of the scatterometry problems. An outline of the FDTD model is shown in Fig.3.33. At the top of the model, an input port (red line) is applied to generate the waveguide mode propagating downwards, whereas the bottom of the model is truncated with a Mur superabsorption. What is original in the approach is that the electric boundary conditions at the lateral walls of the model are substituted with the periodic ones, to maintain propagation of the mode as in an unbounded region. Depending on the polarization of the excited signal, remaining boundaries are set as electric or magnetic ones.

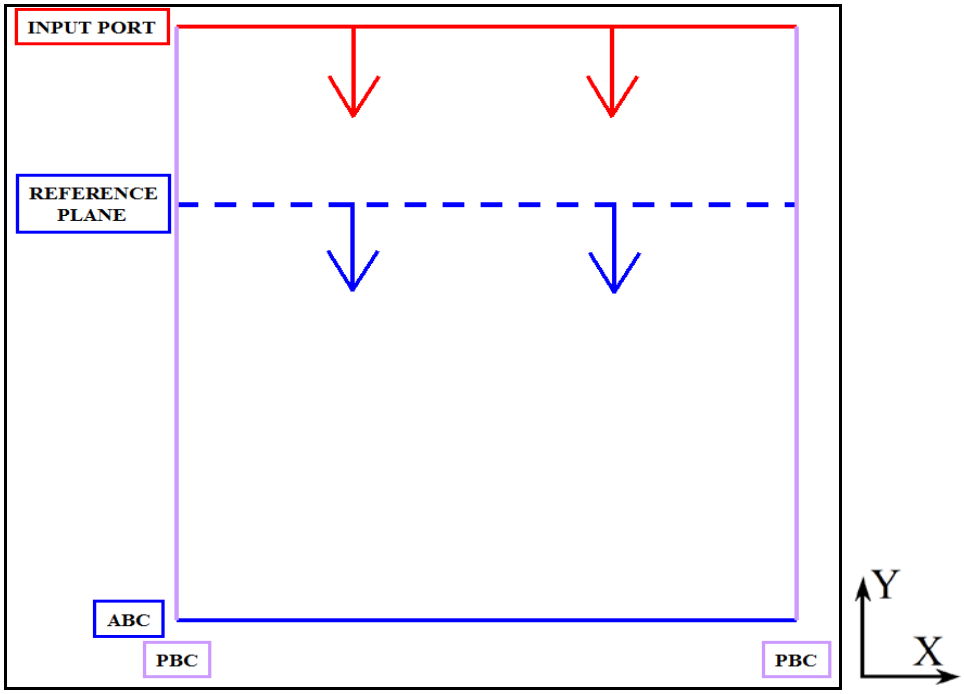

Fig.3.33. Waveguide model with PBC for the scattering of periodic structures.

According to Eq.3.26, an appropriate Floquet phase shift per period is set at the periodic boundary conditions to maintain undisturbed propagation of the mode related to the incident angle (see Eq.**3**.39). Calculation of the mode template at the input port cross-section is performed using the advantage of the V2D FDTD solver [**48**], with the following propagation constant, understood as a simulation parameter (more details can be found in Section **3.4**.2):

$$\beta_{f0} = \frac{2\pi f_0}{c}\sqrt{\varepsilon_{eff}} \tag{3.40}$$

A scattering matrix with a reflection coefficient (S_{11}) is calculated below the input port at a reference plane (a blue dashed line), in the same manner as for nonperiodic waveguide templates [**7**],[62]. If there is any scattering object inside the model, at least two specularly reflected rays are expected since the input port generates two plane waves at $\pm\alpha_{inc}$.

The proposed mode template method is relatively simple and versatile in its applicability. In QuickWave-3D software package [**48**] used by the author of this thesis, the procedure is executed automatically with no need of any user control. A user just needs to define a frequency and an effective permittivity associated with a particular incident angle. However, there is a fundamental limitation. The method proposed in this Section is useless when higher diffraction orders are not evanescent. It stems from the principal assumption which must be

satisfied to calculate a scattering matrix. The assumption is that waveguide modes are orthogonal with each other in the following sense:

$$\iint_S e_{\perp i}(x,y)\times h_{\perp j}(x,y)\,dxdy=0 \tag{3.41}$$

where $e_{\perp i}(x,y)$ and $h_{\perp j}(x,y)$ are orthonormal distributions of transverse electric and magnetic components of the i^{th} and j^{th} modes ($i\neq j$), respectively.

It may be easily proven that the above relation is not satisfied for higher diffraction orders, when the periodic boundary conditions are imposed instead of electric or magnetic ones (see Fig.3.33). It follows from the fact that orthogonality of waveguide modes is satisfied if strict (electric/magnetic) boundary conditions are imposed. Thus, the field distribution at a waveguide cross-section can be expressed as a sine/cosine series that, by definition, sets an orthogonal basis. On the contrary, periodic boundary conditions allow each mode to propagate with an arbitrary phase shift along the periodicity axis. Thus, if a higher diffraction order appears, it may be arbitrarily shifted with respect to a fundamental mode loosing orthogonality needed to separate them.

Let us check the correctness of the aforementioned method by considering an empty model L = 10 mm wide, located between PBCs. The aim is to excite a TE polarized standing wave at f = 15 GHz, with the magnitude of an incident angle equal to $|\alpha_{inc}| = 30^0$. Thus, according to Eq.**3**.23, higher diffraction orders are not supposed to appear. Eq.**3**.39 allows evaluation of the effective permittivity of the searched mode, and it amounts to ε_{eff} = 0.75. Next, according to Eq.3.26, the Floquet phase shift per period is $\psi_x = \pi/2$ rad. The mode template is computed with the V2D FDTD algorithm, with the longitudinal phase constant equal to β_f = 0.272 rad/mm (see Eq.**3**.**40**). Afterwards, the calculated mode template is coupled with the whole model shown in Fig.3.33, driving it with the pulse of a spectrum deliberately wider than usually necessary to visualize some properties of the method.

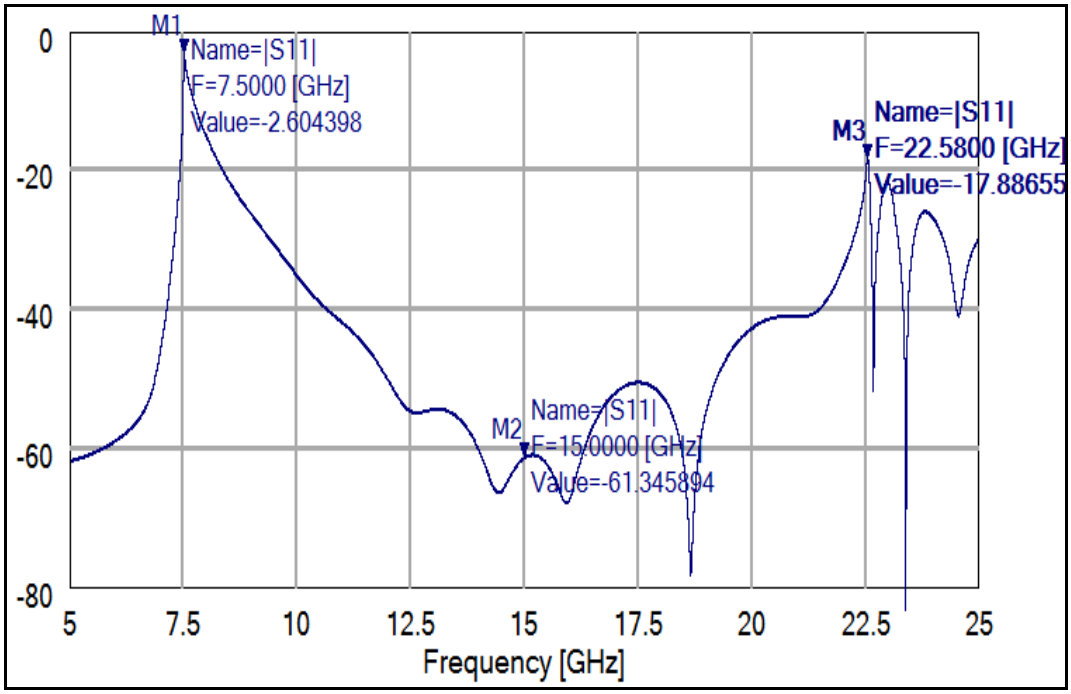

Fig.3.34. Reflection coefficient $|S_{11}|$ obtained in a periodic empty model excited with a TE mode template (L=10mm, f_c=7.5GHz, f=15GHz, ε_{eff}=0.75).

Table 3.4. Values taken from the reflection coefficient shown in Fig.3.34.

	f [GHz]	$\|S_{11}\|$ [dB]
Cut-off frequency of the fundamental mode	7.5	-2.6
Matching frequency of the fundamental mode	15	-61.3
Cut-off frequency of the second mode	22.58	-17.9

Fig.3.34 shows the magnitude of the reflection coefficient $|S_{11}|$ extracted at the reference plane. The marker values are shown in Table **3**.4. It can be noticed that, indeed, the reflection is negligibly small at f = 15 GHz (matched frequency), which proves that there is no obstacle placed inside the model which would diffract the incident wave. Nevertheless, when the frequency deviates from the matched value, the magnitude of the reflection coefficient $|S_{11}|$ increases, and at least three reasons may be specified for that. First of all, the Mur superabsorption applied at the bottom of the model is matched to a plane wave incident at $|\alpha_{inc}| = 30^0$ but, for the specified mode template (fixed effective permittivity), this angle varies with frequency (compare Eq.**3.40**). Secondly, as the frequency decreases, the considered mode is getting closer to its cut-off, which may be directly derived from Eq.**3**.39. In that case, it is equal to f_c = 7.5 GHz, which is consistent with the plot shown in Fig.3.34 since $|S_{11}|$ reaches its global maximum exactly there. Last but not least, as it has already been mentioned,

the method is only applicable to the investigation of specular reflection. Substituting Eq.**3**.39 to Eq.**3**.23 and equating the latter to unity, the following relation is obtained:

$$\sin(\alpha_1) = \frac{\lambda}{L} - \sin(\alpha_{inc}) = \frac{\lambda}{L} - \frac{f_c}{f} = \frac{c}{L f} - \frac{f_c}{f} = 1 \qquad (\mathbf{3}.42)$$

The above formula enables detection of the cut-off frequency of the 1st diffraction order. The calculated frequency f_{c1} = 22.5 GHz is in a good agreement with the reflection coefficient $|S_{11}|$ that, indeed, reaches the local maximum of about -18dB there.

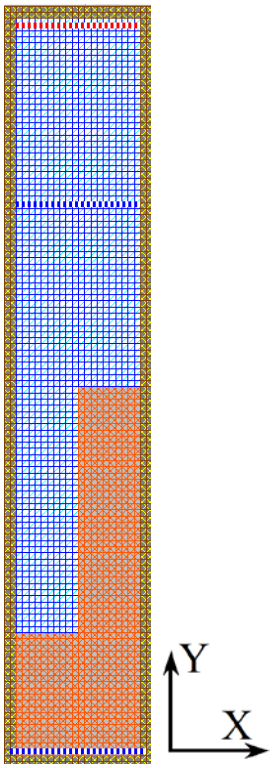

Fig.3.35. FDTD model of a dielectric grating.

Since validity of the method has just been confirmed in an empty air region, let us go further and check how it will work if an obstacle is placed inside the model. Fig.3.35 shows the scenario consisting of one period of teflon dielectric grating (ε_r = 2.2). The height of the line is 20mm, whereas the line to space ratio is exactly L/S = 0.5. The size of the FDTD cell applied during the simulation is a = 0.5 mm, satisfying dispersive requirements of the FDTD algorithm with a large surplus since about 27 cells/λ in the dielectric region are applied. Fig.3.36 shows the plot of $|S_{11}|$ around the frequency of interest, and it can be observed that

the reflection coefficient is equal to $|S_{11}| = 0.097740$ at $f = 15$ GHz. Simulation speed reaches 13700 iter/sec, providing a convergent result after just about 10 ms[7].

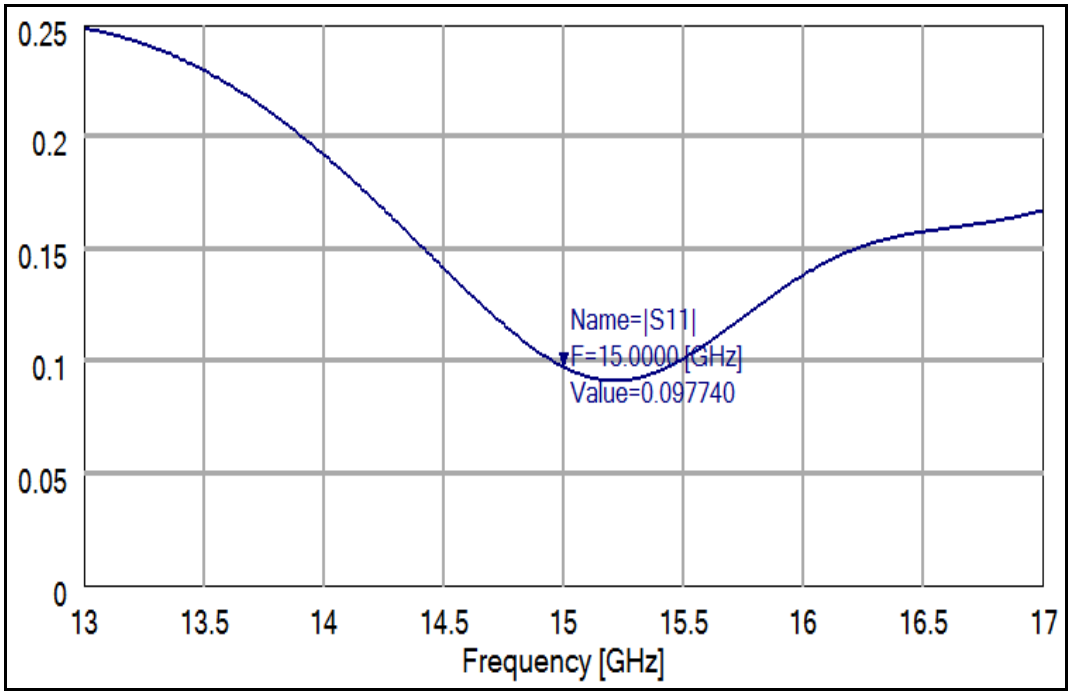

Fig.3.36. Reflection coefficient $|S_{11}|$ obtained for a dielectric grating (ε_r=2.2) excited with a TE mode template (L=10mm, f_c=7.5GHz, f=15GHz, ε_{eff}=0.75).

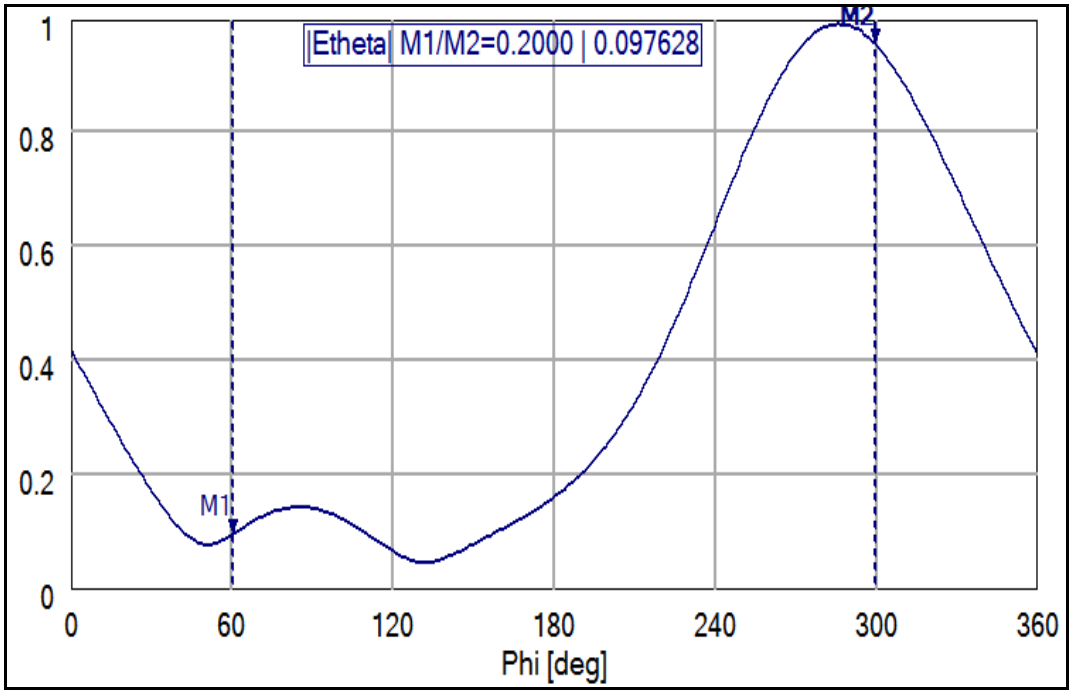

Fig.3.37. Normalized scattering pattern for the dielectric grating shown in Fig.3.35 illuminated with a TE polarized plane wave at $\alpha_{inc} = 30^0$ (f = 15GHz).

[7] Intel Core™2 Duo CPU 3.00GHz, 4094MB RAM, 64-bit Windows Vista Business.

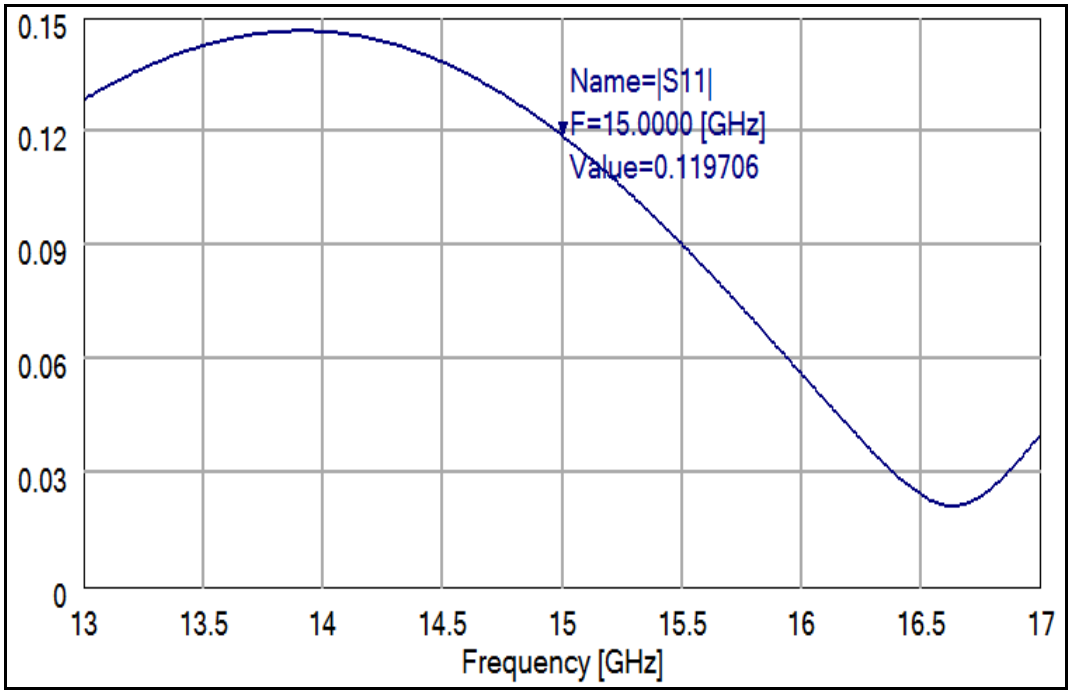

Fig.3.38. Reflection coefficient $|S_{11}|$ obtained for a dielectric grating (ε_r=2.2) excited with a TM mode template (L=10mm, f_c=7.5GHz, f=15GHz, ε_{eff}=0.75).

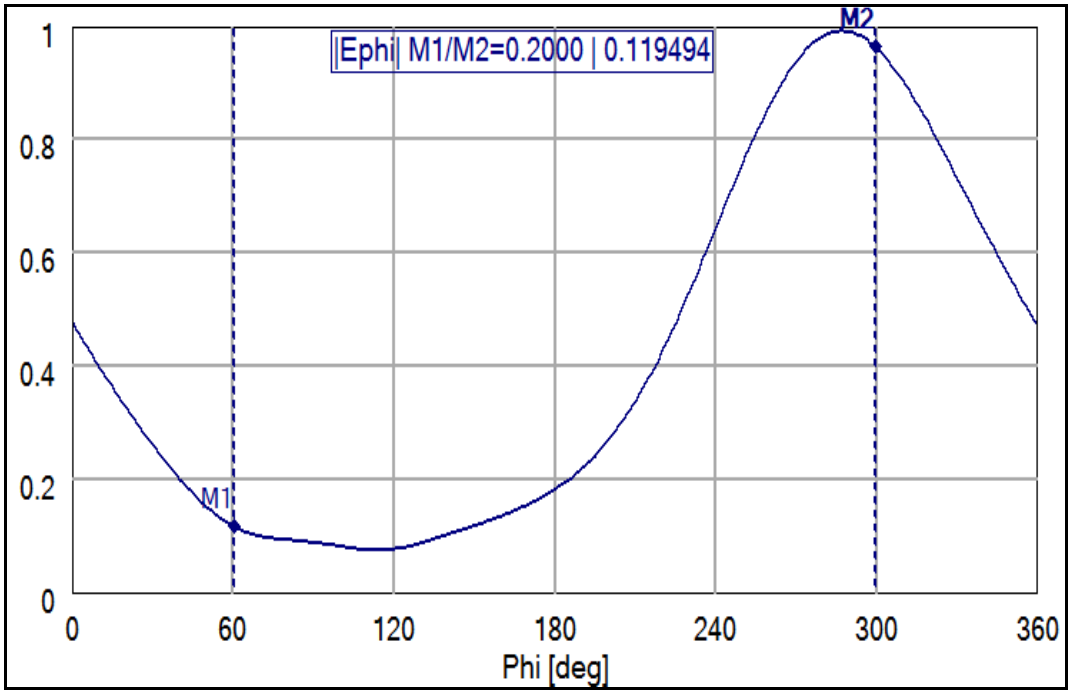

Fig.3.39. Normalized angular scattering pattern for the dielectric grating shown in Fig.3.35 illuminated with a TM polarized plane wave at α_{inc} = 30^0 (f = 15GHz).

Now, let us assess the reliability of the proposed waveguide periodic approach. A normalized angular scattering pattern has been calculated for the same dielectric grating, but this time illuminated with a purely traveling plane wave (see Fig.3.21).

As shown in Fig.3.37, the reflection coefficient is equal to 0.097628, so the discrepancy between the results obtained using both FDTD models reaches about 0.01%. This time a simulation is slightly faster, reaching 14000 iter/sec, with approximately the same computation time. However, the NTF solution stabilizes at the second significant digit, whereas $|S_{11}|$ provides five stable significant digits. Apparently, it makes the mode template method more reliable for the modeling of electrically short scenarios.

To make the analysis complete, let us consider the same problem but with a TM polarized wave. Fig.3.38,39 depict the reflection coefficient $|S_{11}|$ and the angular scattering pattern, respectively. Obtained results differ at the level of about 0.02%, however, like for the TE polarization, only two significant digits are stable in the ASP and five in $|S_{11}|$. Nevertheless, extension of the model to two periods of the grating would alleviate NTF problem at the cost of doubling computational effort.

Now, let us modify the proposed model by changing periodic boundary conditions to perfect electric conductor (see Fig.3.40). First of all, it enables the application of the classic FDTD algorithm with one simulation grid, instead of the CL-FDTD one with two grids, reducing the computational effort at least twice. However, at the same time the mode template flexibility is restricted. Due to the PEC imposed at the sidewalls of the model, only the modes that satisfy the following discrete set of phase shifts can be excited:

$$\beta_x L_x = m\pi \tag{3.43}$$

Hence, the following set of incident angles can be obtained:

$$\sin\left(\alpha_{inc\,m}\right) = \frac{\beta_x}{\beta} = \frac{m\pi}{\beta L_x} \tag{3.44}$$

where m = 1, 2, 3, …

The above formula leads to the major property of the proposed model. The length of the whole model has to be an integer multiple of the fundamental period of the modeled structure $L_x = n\, L_{xp}$. Thus, in order to obtain a particular incidence angle α_{inc} for a specified frequency, the value of the parameter m has to be selected in a way which ensures that the chosen incident angle $\hat{\alpha}_{inc\,m}$ is close enough to the intended one:

$$\sin\left(\hat{\alpha}_{inc\,m}\right) = \frac{m}{n}\frac{\pi}{\beta L_{xp}} \tag{3.45}$$

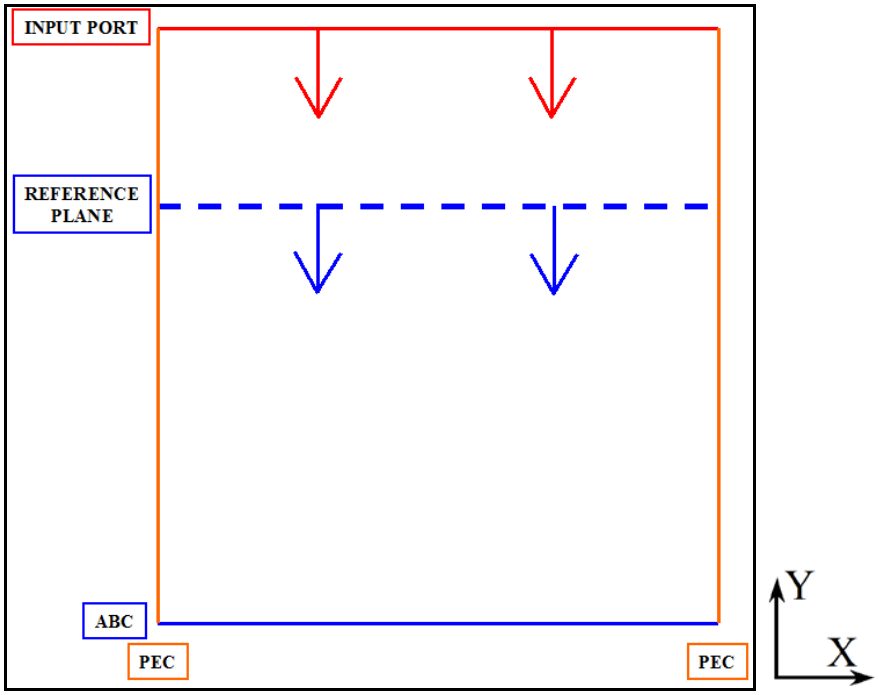

Fig.3.40. Waveguide model with PEC sides for the scattering of periodic structures.

There is a visible tendency for the step between consecutive incident angles $\hat{\alpha}_{inc\,m}$ to decrease with the increasing length of the structure ($n >> 1$). Hence, in general, a better accuracy can be obtained if the model is longer. However, as it will be shown, this requirement may be alleviated under some conditions.

Let us consider incidence of a plane wave on the dielectric coated PEC cross-shaped grating already introduced in this Chapter (see Fig.3.25). The analysis is confined to one frequency point, i.e. $d/\lambda_0 = 0.125$. First, let us check how precisely an incidence angle can be selected. Eq.**3**.45 indicates that the precision of the angle selection rises with the increasing length of

the model, and Fig.3.41 confirms this anticipation, showing that the mismatch exponentially decreases. Nevertheless, the intended angle can be fitted exactly for the following series of discrete points L_x/λ = 0.5, 1.0, 1.5, 2.0, … .

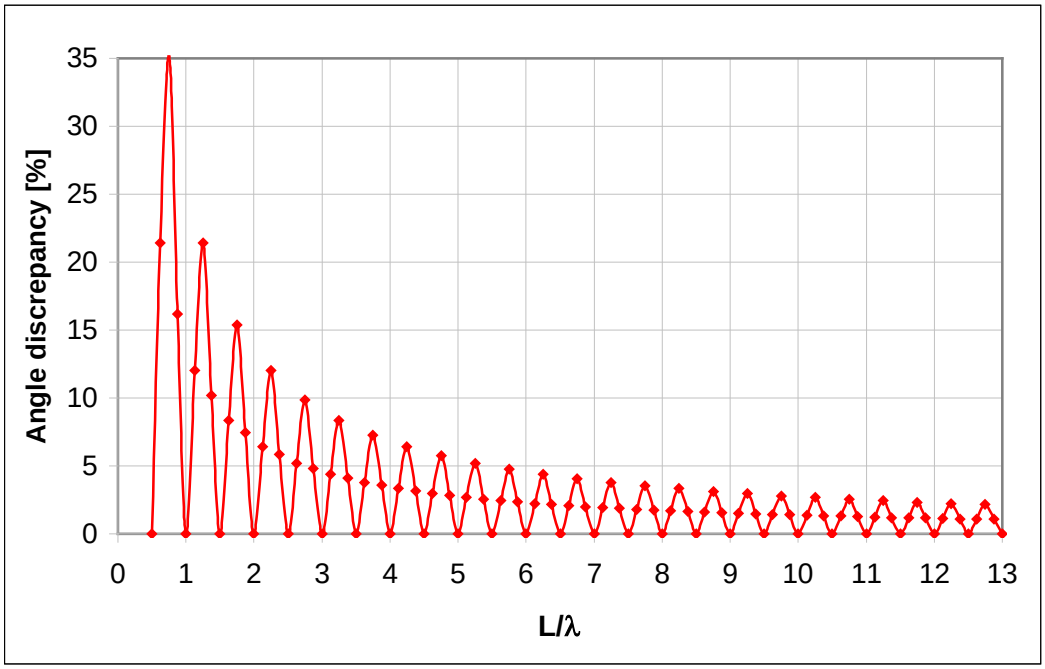

Fig.3.41. Precision magnitude of an incidence angle versus the length of the model of the dielectric coated PEC cross-shaped grating (d = 100 mm, λ = 800mm, $\alpha_{inc} = 30^0$).

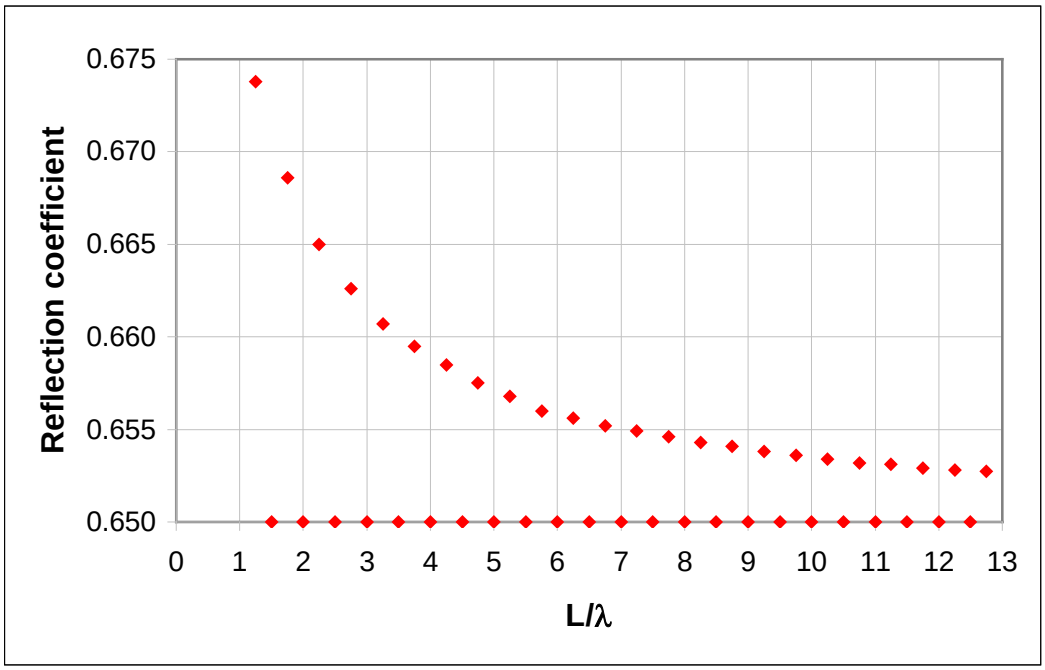

Fig.3.42. Reflection coefficient versus the length of the model of the dielectric coated PEC cross-shaped grating (d = 100 mm, λ = 800mm, $\alpha_{inc} = 30^0$).

Next, simulations have been performed for varying model length to show that the mismatch of an illumination angle has a major contribution to the accuracy of the obtained reflection coefficient. Fig.3.42 shows that the model does not have to be very long to get the accurate result provided that the intended incidence angle is exactly fitted. Reflection coefficients obtained for the unmatched points exponentially converge to the accurate value.

Another essential feature of the waveguide method with PEC lateral boundaries is the possibility to evaluate higher diffraction orders. Contrary to the already introduced waveguide model with PBCs, where waveguide-like modes are considered (see Fig.3.33), the PEC version of the model excites strictly a waveguide mode, which is orthogonal to the other modes. Moreover, if the fundamental mode is properly adjusted to the corresponding incidence angle (see Eq.**3**.45), the potential higher diffraction orders will also satisfy electric boundary conditions at the waveguide port. Therefore, if another port matched to the higher order mode is defined in the same place as the input port, it is possible to monitor the amount of power reflected at the considered higher diffraction order.

To exemplify the method, let us go back to the structure shown in Fig.3.25 illuminated in the *xy*-plane at an angle of $\alpha_{inc} = 30^0$. It will be investigated on one frequency for $d/\lambda_0 = 0.883$ (f = 2.65 GHz). According to Eq.**3**.23, the 1st diffraction order can be expected at $\alpha_1 = 39.2^0$, which corresponds to $(\phi, \theta) = (129.2^0, 90^0)$ in spherical coordinates[8]. The model with 17 fundamental periods of grating is defined since such a length of the model enables to keep a good matching of two mode templates which correspond to the 0th and the 1st diffraction orders. Following Eq.**3**.39, the effective permittivity of the fundamental mode is equal to $\varepsilon_{eff} = 0.750366$, which is equivalent to the incidence angle of $\alpha_{inc} = 29.98^0$. As regards another mode, it has the effective permittivity equal to $\varepsilon_{eff} = 0.599477$, corresponding to $\alpha_1 = 39.26^0$. Thus, intended angles are matched with the accuracy better than 0.1%.

The structure is excited with a short pulse with the spectrum within 2.5 – 3.0 GHz, providing the following scattering parameters: $|S_{11}|^2 = 0.748$ and $|S_{21}|^2 = 0.156$. The first value corresponds to the power reflection coefficient of the 0th order, whereas the second value is understood as the power transmission coefficient from the 0th order mode to the 1st one. However, to assess the reliability of the obtained solution, the simulation of the same scenario

[8] See Appendix 3.

will be run in the already studied plane wave excitation model (see Fig.3.21). Fig.3.43 presents the obtained scattering pattern in a quadratic (power) scaling and, indeed, the ray of the 1st diffraction order can be observed. The comparison of the results obtained with both methods, shown in Table **3**.5, indicates that the discrepancy is about 0.4% and 1.1% for the 0th and the 1st order, respectively, with approximately the same computation time.

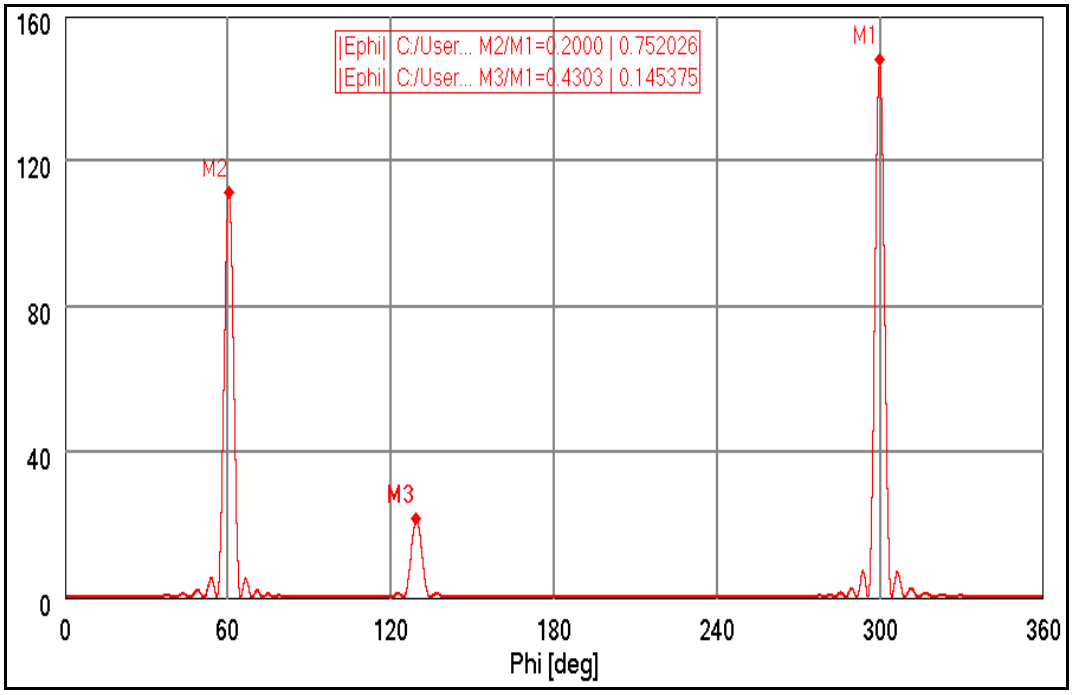

Fig.3.43. Angular scattering pattern (power scaling) for the dielectric coated PEC cross-shaped grating (*d* = 100 mm, α_{inc} = 30^0, *f* = 2.65GHz) obtained in a 17 periods model.

Table 3.5. Values taken from the angular scattering patterns shown in Fig.3.43.

$\|S_{11}\|^2$	$\|S_{21}\|^2$	R_{P0} (60^0/300^0)	R_{P1} (129^0/300^0)
0.748	0.156	0.752	0.145

The main advantage of the approach with PEC boundary conditions is 50% smaller computational effort as compared to the model with PBCs imposed. However, the major disadvantage of the first method is the necessity to match precisely the waveguide mode to the intended incidence angle, which can impose definition of a longer FDTD model.

In the aforementioned waveguide approach, a periodic structure has been extended to the whole length of the model. In principle, it refers to the case of an infinite spot over an infinite structure (see Section 4.5). It should be emphasized, however, that the waveguide approach

might be also applicable to the investigation of an infinite spot over a finite structure (see Fig.3.44). Practically, it refers to so-called isolated targets, composed of periodic structures separated from each other by the same distance. In such a scenario, a periodic structure is shorter than the whole waveguide model, which may be useful when investigating the impact of the diffraction on edges of the targets on the angular scattering pattern. However, since the concept of the FDTD model does not change at all in this case, a thorough investigation of this issue will be omitted here.

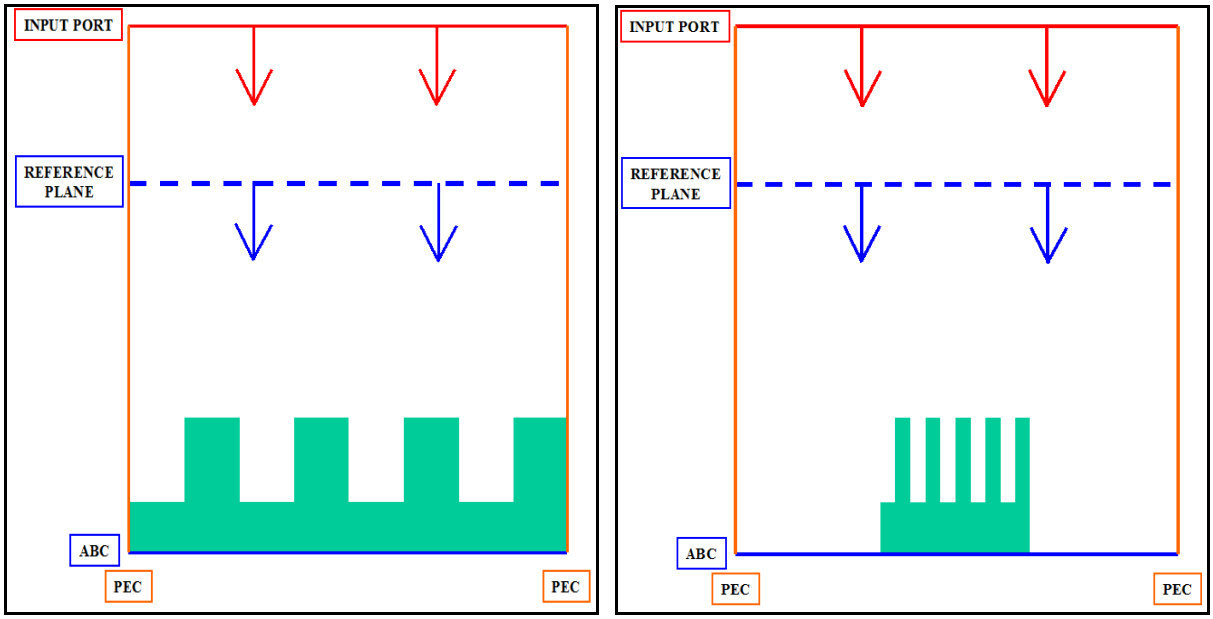

a) **b)**

Fig.3.44. Waveguide model with PEC sidewalls for the infinite spot size scattering of infinite (a) / finite (b) periodic structure.

So far, a few methods useful to the modeling of a plane wave scattering from periodic structures have been considered. First, an approximate approach was studied, which allows reducing the FDTD model to one or just a few fundamental periods of the structure, depending on the required computational precision. Two types of simulation models have been investigated in that case: a plane wave source and a waveguide port with periodic boundary conditions. Next, it was proposed to modify a waveguide approach exchanging PBCs with PEC to reduce computational effort, and to extend applicability of the model to higher diffraction orders. The summary of the advantages and limitations of these methods is presented in Table 3.6. The results prove the first statement of the thesis posed in Chapter 1. In the next Section, the attention will be focused on a Gaussian beam illumination of a periodic structure.

Table 3.6. Pros and cons of the methods introduced in Section 3.5.1.

Method	Pros	Cons
PLW & NTF &PBC	1. A possibility to reduce an FDTD model to one or few periods of a structure. 2. Simulation possible for an arbitrary angle of incidence and an arbitrary polarization. 3. Possible detection of higher diffraction orders.	1. Accuracy only at a single matching frequency. 2. Doubled memory occupation (two FDTD grids).
WG port & PBC	1. A robust technique taking advantage of well-established modal templates excitation and extraction.	1. Accuracy only at a single matching frequency. 2. Doubled memory occupation (two FDTD grids). 3. Accurate only for specular (mirror-like) reflection.
WG port & PEC	1. The most robust technique among those on the list (due to rigid boundary conditions). 2. Possible analysis of higher diffraction orders. 3. A single FDTD grid.	1. Accuracy strongly dependent on waveguide mode matching to the corresponding angle of incidence.

3.5.2 Gaussian Beam Illumination of Periodic Structures

In principle, the plane wave excitation considered so far is a simplified formalism used to approximate an electromagnetic wave propagating in a particular direction far from a radiation source. Such a specific approximation is often sufficient for the modeling of practical problems, although, in fact, an EM wave never maintains a plane wavefront when propagating in a linear medium. On the contrary, the wavefront always converges or diverges when receding from a source. The most popular approximation of such a case is known as a Gaussian beam.

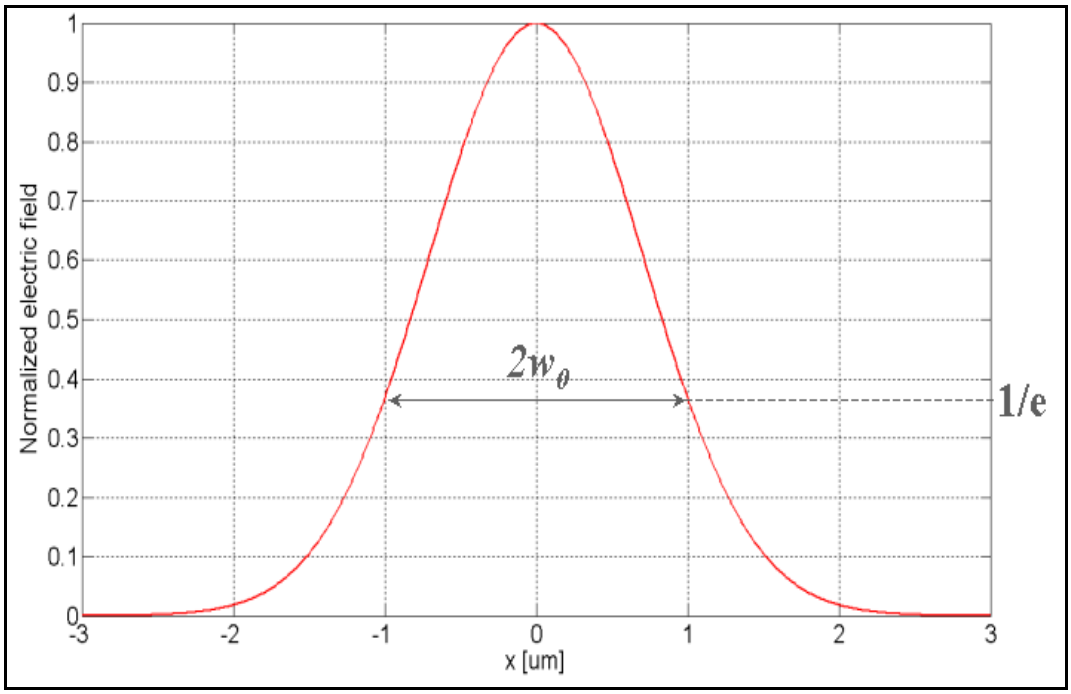

Fig.3.45. Shape of a Gaussian beam in a focal plane (y = 0).

The following formulae describe 3D and 2D Gaussian beams propagating along the y-axis [**63**], respectively:

$$E = E_0 \frac{w_0}{w(y)} \exp\left[-\frac{r^2}{w^2(y)} - j\left(\beta y + \beta y \frac{r^2}{2\left(y^2 + y_0^2\right)} - a\tan\left(\frac{y}{y_0}\right)\right)\right] \tag{3.46}$$

$$E = E_0 \sqrt{\frac{w_0}{w(y)}} \exp\left[-\frac{x^2}{w^2(y)} - j\left(\beta y + \beta y \frac{x^2}{2\left(y^2 + y_0^2\right)} - \frac{1}{2} a\tan\left(\frac{y}{y_0}\right)\right)\right] \tag{3.47}$$

where

$$r = \sqrt{x^2 + z^2}$$

$$w(y) = w_0 \sqrt{1 + \frac{y^2}{y_0^2}} \tag{3.48}$$

$$y_0 = \frac{\beta w_0^2}{2} \tag{3.49}$$

and w_0 stands for the beam's spot radius understood as the distance from the Gaussian beam axis in the focal plane where the amplitude decreases by 1/e (see Fig.3.45).

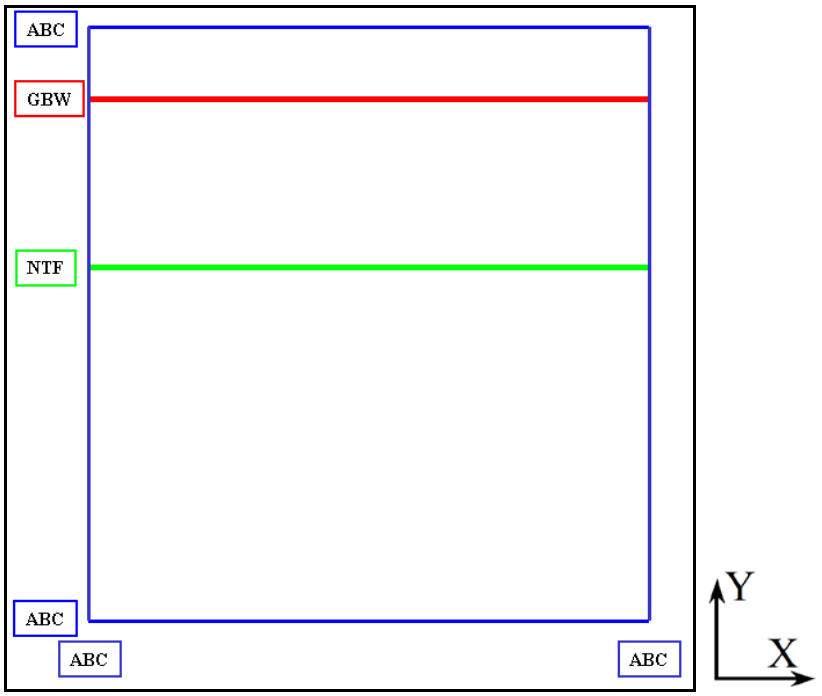

Fig.3.46. Scheme of the FDTD model for a Gaussian beam obliquely incident on the structure periodic along the *x*-axis.

In this thesis, without loss of generality, the attention will be focused on the 2D FDTD model of a Gaussian beam illumination of a periodic structure, taking advantage of the classic FDTD algorithm. Fig.3.46 shows the FDTD model which will be applied hereafter. In principle, it is very similar to the one shown in Fig.3.21. However, this time a plane wave wall (PLW) is substituted with a Gaussian beam wall (GBW). In principle, operation of a GBW source is similar to a PLW one in a sense that it divides the considered volume into total and scattered field regions (compare Fig.3.21). The only difference is in the shape of the beam. In this particular scenario shown in Fig.3.46, GBW excites a Gaussian beam propagating downwards, whereas the area above is filled only with scattered field (if such is generated). Moreover, periodic boundary conditions, originally placed at the sidewalls, are replaced with a Mur superabsorption, truncating the volume of the FDTD model. The model is long enough, as compared to the beam's spot radius, to avoid spurious diffraction of the EM field from the absorbing sidewalls. The definition of the TE/TM polarization, which will be used below, can be found in Fig.3.19.

Fig.3.47 shows an example of a TE polarized 2D Gaussian beam propagating obliquely in the empty air model and centered in the middle. The beam is incident at $\lambda_{inc} = 25^0$ and driven with

a sinusoidal excitation at $\lambda = 0.5\mu m$ (see Fig.3.20). It will be applied to illuminate the periodic structure placed below the NTF plane.

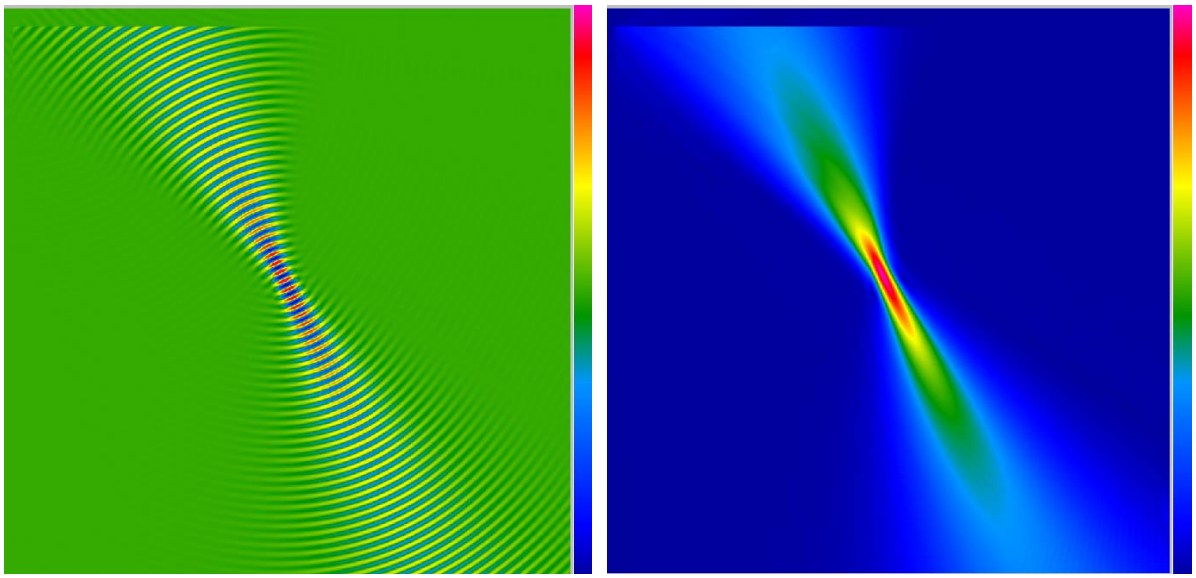

Fig.3.47. Snapshots of the electric field (left) and the envelope (right) for a TE polarized 2D Gaussian beam incident in the *xy*-plane ($\lambda = 0.5\mu m$, $w_0 = 1\mu m$, AOI = 25^0).

Let us consider the poly-to-active stack already shown in Fig.3.29. The initial results of the author's studies of this issue were published in [**64**]. Fig.3.30 depicts the spectrum of the reflection coefficient computed with the CL-FDTD algorithm. First, analysis of the scenario excited with a Gaussian beam of $w_0 = 20\mu m$ spot diameter will be executed and the obtained reflection coefficient will be compared to the one shown in Fig.3.30. Fig.3.48 shows the computational results of both methods and a good agreement can be noticed. It confirms that a plane wave illumination of an infinite structure can be a good method to overcome the computational limitations of the real scattering problem with a spatially finite illumination spot.

Once the agreement between infinite and finite approaches has been confirmed for a large beam diameter, it will be assessed how the finite solution diverges when the spot is getting smaller. For this purpose, let us perform several simulations to observe a deviation of the relevant reflection coefficient with diminishing spot size. It should be emphasized, however, that the sensitivity of the reflection coefficient on the spot size is scenario-dependent so the conclusions derived below cannot be understood as general.

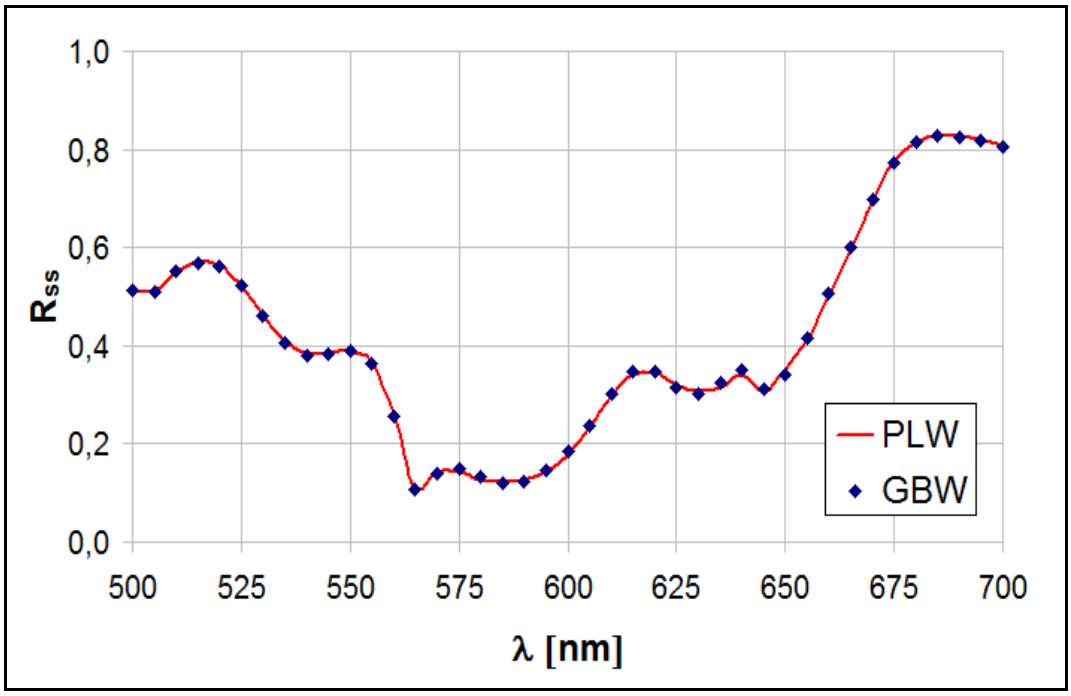

Fig.3.48. Reflection coefficient for a TE polarized 2D Gaussian beam incident at 25^0 on the target shown in Fig.3.29.

Fig.3.49,50 show the absolute deviation of TE and TM reflection coefficients as a function of diminishing spot size. The following formula has been applied to calculate the absolute deviation:

$$\Delta R_k \ [\%] = 100 \left(R_k - R_{ref} \right) \qquad (3.50)$$

where R_k stands for a considered reflection coefficient R_{ss} (R_{pp}) and R_{ref} denotes the reference value of R_{ss} (R_{pp}) obtained for the largest spot size.

The largest spot covers about 62 pitches of the considered poly-to-active stack, whereas the smallest one covers only two pitches. It can be noticed that sensitivity to the spot size is of the order of 0.3% and 0.1% for the TE and TM polarizations, respectively, down to a 2-3 micron spot size (6-10 pitches). It can also be noticed that the TM polarization is less sensitive to the spot size changes. However, below the level of 2-3 microns we observe rapid changes of the reflection coefficients.

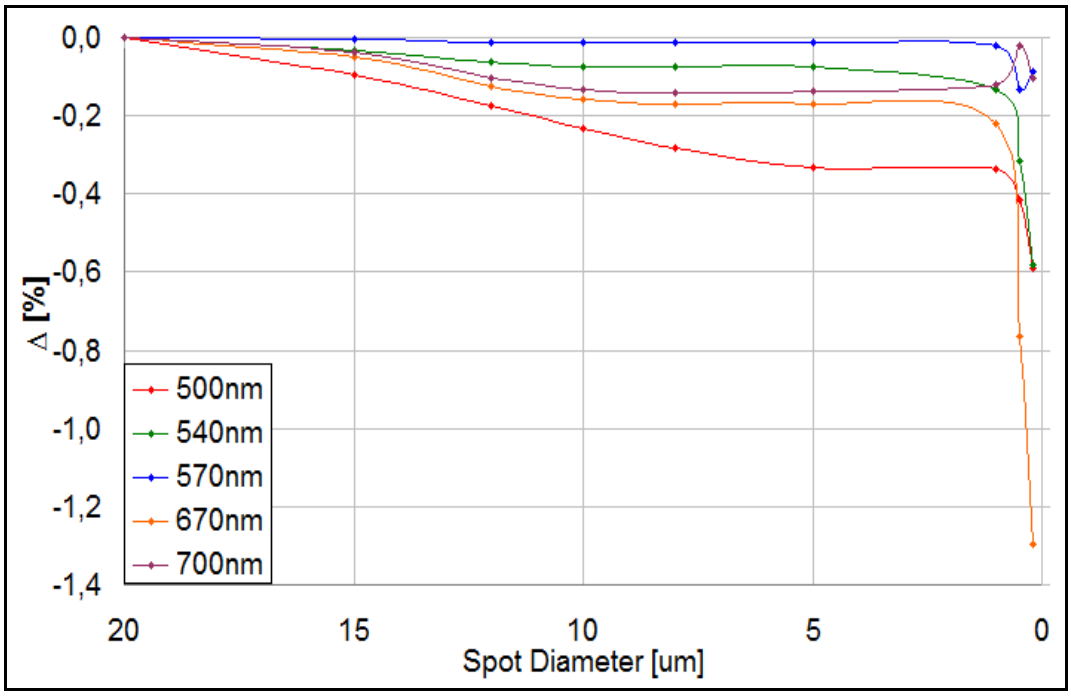

Fig.3.49. Absolute deviation of R_{ss} with a diminishing spot size for the poly-to-active stack (pitch = 320nm).

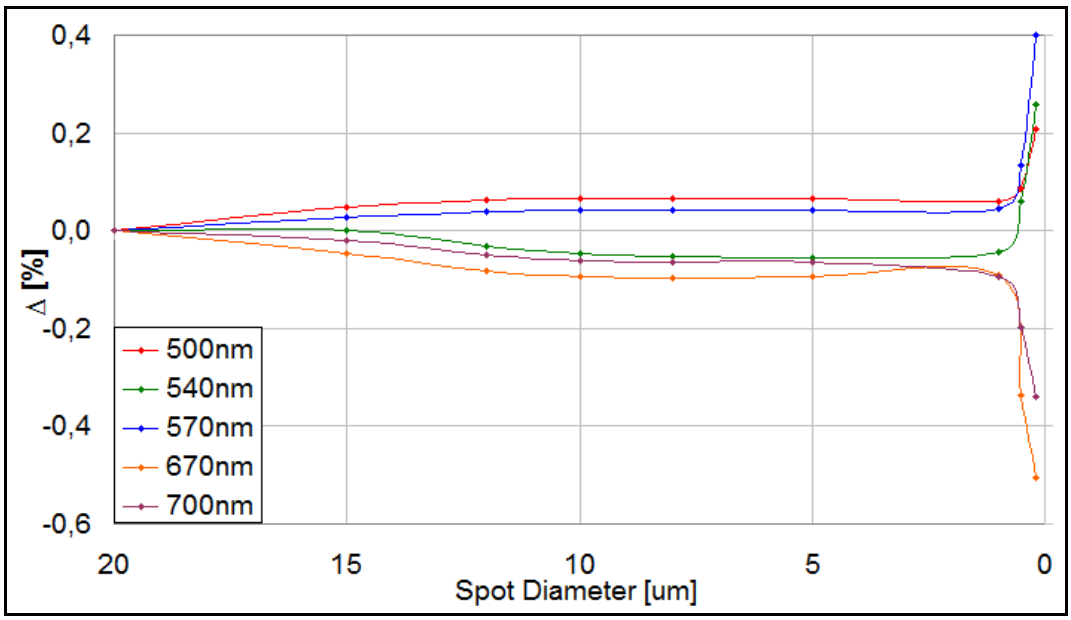

Fig.3.50. Absolute deviation of R_{pp} with a diminishing spot size for the poly-to-active stack (pitch = 320nm).

Summing up this Section, it has been confirmed that the approximate approach with a plane wave excitation of an infinitely long periodic structure can be a good alternative to the direct approach with a spatially finite scenario illuminated with a Gaussian beam. However, special

care as regards to the accuracy of the approximation must be taken if a spot is relatively small as compared to the number of illuminated periods.

3.6 Summary

The application of the partially analytical FDTD method dedicated to the modeling of electromagnetic wave scattering from periodic structures has been studied in this Chapter. A thorough insight into the procedure of looping periodic boundary conditions in the CL-FDTD algorithm extended by the author to 2D and 3D periodicity has been given. The author has also applied 1D and 2D PBCs in the V2D FDTD method. It has been shown that the implemented features allow simulating both eigenvalue and deterministic periodic problems. Special attention has been focused on the applicability to the modeling of plane wave scattering from infinite periodic structures. For that purpose, two types of modeling scenarios have been introduced and cross-compared, taking into account many modeling criteria, such as polarization, beam shape, diffraction orders and the size of the model. The first scenario takes advantage of a plane wave wall and a near-to-far transformation, which allow simulation and accurate extraction of the specular and higher diffraction orders. The second modeling scenario is based on the waveguide approach. In the first version of this approach, the periodic boundary conditions have been applied. It has been shown that the method is dedicated to the modeling of specular reflection only. However, by substituting periodic boundary conditions with a perfect electric conductor, it is possible to extend the applicability of the waveguide method to the higher diffraction orders, but at the expense of a mismatch of the incident angle. Finally, the last Section of this Chapter has been focused on a Gaussian beam illumination of a periodic structure as the most realistic case. The study presented in this Chapter fully proves the first statement of the thesis, formulated in Chapter 1.

Chapter 4

Hybrid FDTD Modeling of the Far-Field Microscopy Imaging

4.1 Introduction

This Chapter presents the original study of the author of this thesis on the applicability of the FDTD method to the modeling of imaging phenomenon, which plays an important role in optical microscopes. The phenomenon is well known and understood in modern optics. However, imaging techniques are still under development, pushing the resolution of methods for imaging complex geometrical structures down to a nanometer scale. These high requirements contribute to demand for an increasing accuracy of design and modeling tools. Yet, the popular approximate methods, such as the one based on Fresnel approximation [**65**], have inherent limitations and, thus, are not sufficiently accurate for modeling of a whole imaging path from a light source to an image plane. Hence, hybrid modeling taking advantage of various modeling methods might be preferable. The critical part of the imaging path is the diffraction of light from a target (specimen). The target can be of an arbitrary shape and composed of various materials. Under such circumstances, the approximate modeling methods may not be able to meet expected requirements with sufficient accuracy. By contrast, application of the FDTD method does not impose any specific limitations to the scenario, enabling to achieve a very fine solution if needed. The concept of employing the FDTD method to the modeling of imaging problems is not new and can be found in radar cross section (RCS) techniques [**66**] or near field optics [**67**]. However, it is hard to find comprehensive studies of possible application of the FDTD method to modeling of the classic far-field microscope imaging.

The limited interest in application of the FDTD method in this field follows from the fact that far-field microscope imaging is an optical problem with dimensions of the entire system measured in thousands of wavelengths, so its direct analysis with the FDTD method is not possible at the moment, even with the aid of modern supercomputers. It is generally

recognized that present computer systems allow 3D analysis of objects having linear dimensions not bigger than a few dozens of wavelengths. This is the main reason behind its narrow range of application in optics where the electrical size of objects is typically much bigger. However, the FDTD method as a full-wave approach has several advantages prompting us to apply it in a selected part of computational domain and to combine it with other methods typical for optics. Therefore, this Chapter addresses the issue of the potential application of the FDTD method coupled with a particular approximate optical approach to enhance capabilities of the overall algorithm of the far-field microscope imaging. Initial results of the author's work presented below have been published in [**68**],[**69**],[**70**].

The main goal of this study is to define an algorithm that takes advantage of the FDTD method in modeling of an imaging phenomenon exploited in the far-field microscope systems. These imaging methods have various practical applications, including the quality control of masks and reticles in the lithography process of integrated circuits or 3D imaging of biological tissues, to name just a few. First, a theoretical background - essential in the understanding of the chosen modeling method - will be provided. Then, a brief survey of the hybrid algorithms that take advantage of the FDTD method in the modeling of far-field optical imaging problems will be presented. Subsequently, wide-field microscopy will be considered as a basic concept exploited in optical microscopes [**71**]. Eventually, the study will be extended to confocal imaging systems [**71**] dedicated to the analysis of 3D geometry of a thick target (specimen). Since the main scope of this Chapter is strictly related to optical problems, notation usually applied in that field is used hereafter. In particular, the symbol *i* is used instead of *j* to denote a complex number. Moreover, it is assumed that a monochromatic plane wave has the following notation:

$$U = U_0 \, e^{ikr} e^{-i\omega t} \tag{4.1}$$

The difference as compared to the notation common in electronics and used in the previous Chapters of this thesis lies in the opposite sign of the argument in the exponent.

4.2 Theoretical Background

A brief historical review of how the formalism explaining a diffraction phenomenon was developed will precede the study of the optical imaging, as it plays a key role in the concept of imaging theory. Essentially, although there is a variety of imaging systems depending on the particular technology applied, a final image is always obtained by an appropriate processing of light diffracted from or transmitted through a target (specimen).

In 1678, a Dutch physicist, Christiaan Huygens, formulated the main concept that became a starting point for the further study in this field. He stated that each point of the advancing wavefront is a source of a new spherical radiation, and all the secondary waves reconstruct the wavefront. Subsequently, this concept had been independently developed by Thomas Young (1804) and Augustin-Jean Fresnel (1818). However, Gustav Kirchhoff (1882) was the first who formulated an explicit solution of the wave equation with well-defined boundary conditions [**72**].

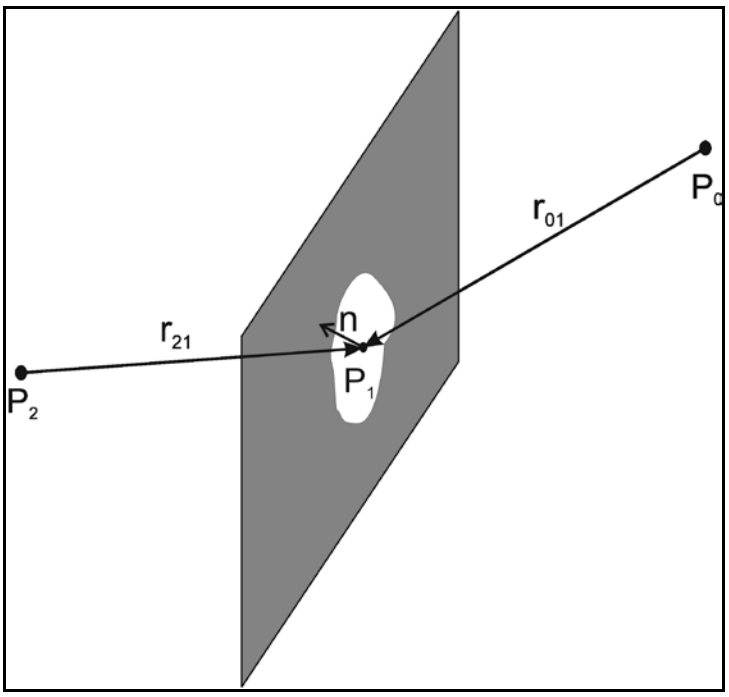

Fig.4.1. Point source radiation through the aperture.

Let us assume that a point source of electromagnetic radiation illuminates an air hole in an unbounded metal layer as shown in Fig.**4.1**. For the purpose of this study, the problem is reduced to the scalar one, neglecting the issue of source polarization. According to the

Fresnel-Kirchhoff diffraction principle, the field behind the wall is given by the following formula:

$$U(P_0) = \frac{U(P_2)}{i\lambda} \iint_S \frac{\exp[ik(r_{21} + r_{01})]}{r_{21}\, r_{01}} \left[\frac{\cos(\hat{n}, \vec{r}_{01}) - \cos(\hat{n}, \vec{r}_{21})}{2} \right] ds \qquad (\mathbf{4}.2)$$

Subsequently, assuming that the radiation source $U(P_2)$ is far from the air hole ($r_{21} >> \lambda$), the Rayleigh-Sommerfeld approach leads to a simplified integral with the integration over the air hole surface:

$$U(P_0) = \frac{1}{i\lambda} \iint_S U(P_1) \frac{\exp(ik\, r_{01})}{r_{01}} \cos(\hat{n}, \vec{r}_{01})\, ds \qquad (\mathbf{4}.3)$$

A brief look upon this equation allows us to recognize the Huygens principle since the field is integrated over each point within the air hole, as if it were a source of a spherical wave (modified by the cosine directional coefficient).

Subsequently, applying a paraxial Fresnel approximation ($\angle(n, r_{01}) \sim 0^0$), Eq.**4**.**3** can be simplified to the following one:

$$U(x, y) = \frac{e^{ikz}}{i\lambda z} \iint_S U(x', y') e^{\frac{ik}{2z}\left[(x - x'^2) + (y - y'^2)\right]} dx' dy' \qquad (\mathbf{4}.4)$$

It can be noticed (see Eq.**4**.**4**) that the field at the observation point $U(x,y)$ may be understood as a 2D convolution of the source field distribution $U(x',y')$ and the impulse response of a free space region given by:

$$h(x, y) = \frac{e^{ikz}}{i\lambda z} e^{\frac{ik}{2z}(x^2 + y^2)} \qquad (\mathbf{4}.5)$$

Appropriate rearrangement of Eq.**4.4** leads to the following expression:

$$U(x,y)=\frac{e^{ikz}}{i\lambda z}e^{\frac{ik}{2z}\left(x^2+y^2\right)}\iint_S U(x',y')e^{\frac{ik}{2z}\left(x'^2+y'^2\right)}e^{-i2\pi\left(\frac{x}{\lambda z}x'+\frac{y}{\lambda z}y'\right)}dx'dy' \quad (\mathbf{4}.6)$$

where one can recognize Fourier transform to an angular domain:

$$U(x,y)=\frac{e^{ikz}}{i\lambda z}e^{\frac{ik}{2z}\left(x^2+y^2\right)}\Im\left[U(x',y')e^{\frac{ik}{2z}\left(x'^2+y'^2\right)}\right] \quad (\mathbf{4}.7)$$

with the following definition of angular frequencies:

$$f_x=x/\lambda z;\qquad f_y=y/\lambda z \quad (\mathbf{4}.8)$$

Let us introduce the last approximation, known as Fraunhofer (or far field) approximation, assuming that the source is electrically small as compared to the distance to the observation point. Thus, the equation - well known in the antenna theory [**73**] - is obtained [**71**]:

$$U(x,y)=\frac{e^{ikz}}{i\lambda z}e^{\frac{ik}{2z}\left(x^2+y^2\right)}\iint_S U(x',y')e^{-i2\pi\left(\frac{x}{\lambda z}x'+\frac{y}{\lambda z}y'\right)}dx'dy' \quad (\mathbf{4}.9)$$

The above expression evidently depicts that the free space between the electromagnetic source and the observation point located in Fraunhofer region performs Fourier transform to the angular domain of the source field spatial distribution.

Each of the approximations outlined above reduces the computational effort when calculating field at the observation point. The Fresnel formula (see Eq.**4.4**) always converges to the Fraunhofer one (see Eq.**4.9**) with an increasing distance. Typically, in modeling of the far-field microscope imaging the Fresnel approach

is employed to avoid the risk of potential inaccuracy of the Fraunhofer approximation, although it needs to be mentioned that such an approach requires higher computer effort.

The Fourier transform allows substitution of a time consuming convolution appearing in the Fresnel formula (see Eq.**4**.**4**), with a much simpler multiplication in a Fourier domain:

$$U_i\left(f_x, f_y\right) = h\left(f_x, f_y\right) U_o\left(f_x, f_y\right) \tag{**4**.10}$$

where [**71**]:

$$h\left(f_x, f_y\right) = e^{ikd}\ e^{-0.5ikd\lambda^2\left(f_x^2 + f_y^2\right)} \tag{**4**.11}$$

and the subscripts ***o*** and ***i*** denote the image and object planes, respectively.

Regarding spherical lenses, the simplest approximation is a perfectly thin spherical lens described by the following phase transfer function [**71**]:

$$t_L\left(x, y\right) = e^{-i\frac{k}{2f}\left(x^2 + y^2\right)} \tag{**4**.12}$$

where *f* stands for the lens focal length.

Field distribution behind the lens is the product of the field in front of the lens and the lens transfer function:

$$U_2\left(x, y\right) = t_L\left(x, y\right)\ U_1\left(x, y\right) \tag{**4**.13}$$

It indicates that the Fourier transform is not preferable in this area since the spatial multiplication given by Eq.**4**.**13** would have been changed to time consuming convolution in a Fourier (angular) domain. Finally, field distribution behind the lens $U_2(x,y)$ can be processed to an image plane applying impulse response of an open air region between the lens and the image plane, in a similar way as in Eq.**4**.**10**.

To summarize, the part of diffraction theory important from the point of view of electromagnetic modeling of the far-field microscope imaging investigated hereafter has been recalled. The next Section is focused on applicability of the FDTD method to EM modeling of a classic wide-field microscope.

4.3 State-of-the-art

Due to the reason mentioned in the previous Section, the literature concerning applicability of the FDTD method to the modeling of the far-field imaging problems is very limited. One can find a lot of research done in the field of breast cancer detection [**74**], but it works with a different approach to the imaging concept (not utilizing focusing elements like lenses). In 2004 Hollmann et al. published a paper [**75**] about the hybrid FDTD-Fresnel imaging of living tissues (embryo). The authors applied the FDTD method in a close vicinity of the target, in order to expose it to plane wave illumination and to obtain scattered fields in the whole surrounding volume. These volume fields were further processed with 3D Green's function to get the fields at the lens plane. The rest of the imaging path was modeled with the aid of the Fresnel approximation. In principle, this is a slightly different approach from the one which is going to be developed in this Chapter since in real microscopes the target is never totally exposed to a scanning beam, but the beam is spatially restricted to the focal spot of a particular dimension.

Another notification about the hybrid FDTD-Fresnel modeling can be found on the website of the *PlanetQuest* project, led by Jet Propulsion Laboratory [**76**], where the FDTD method together with the so-called *Fresnel propagator* are applied to process measurement results of distant stars and planets with a real confocal optical system. However, there are no details provided about the modeling conditions.

The last paper that is going to be addressed is [**77**]. It refers to EM modeling of the confocal 3D imaging of subwavelength features. The authors proposed the FDTD model with a Gaussian beam illumination for the confocal characterization of 2D nanovoids fabricated inside a polymer volume. The scheme of the FDTD model looks similar to the one proposed by the author in Section 4.5, but [**77**] lacks comprehensive explanation how the final image is processed. The authors focused on application rather than on detailed description of the modeling issue.

4.4 Hybrid FDTD Modeling of the Wide-Field Microscopy

Historically, the wide-field microscopy was the first imaging concept applicable in the microscopes built of optical lenses. Although modern imaging tools are much more sophisticated, with specialized techniques applied to push the resolution down to the physical limits of the particular technology, the basic idea has remained the same. Therefore, without loss of generality of further conclusions, the study presented hereafter will be confined to a simple imaging scenario composed of one spherical lens, in order to concentrate only on the hybrid modeling of the imaging phenomenon. The goal is to assess whether the FDTD method can enhance capabilities of the modeling algorithms used in optics. Let us first introduce the investigated scenario and present its short theoretical description.

4.4.3 Introduction to Wide-Field Microscopy

Fig.**4.2** shows a lens-imaging scenario which will be studied in this Section. There are various types of wide-field microscopy systems, such as transmitted, reflected, etc. This study will be concentrated on the reflected light microscopy. Let us assume a perfectly thin lens approximation [**71**] to suppress an aberration issue. According to geometrical optics, the thin lens formula relates the object distance z_o with the image distance z_i in the following manner:

$$\frac{1}{f} = \frac{1}{z_o} + \frac{1}{z_i} \tag{4.14}$$

where f stands for the focal length of a lens.

The ratio between image and object distances determines the magnification factor M of a single lens system. The obtained image is inversed with respect to the object. However, although geometrical optics allows some estimation of the object plane and magnification, it does not quantitatively explain how the image is constructed. This is a role of the diffraction theory, already pointed out in Section **4.2**.

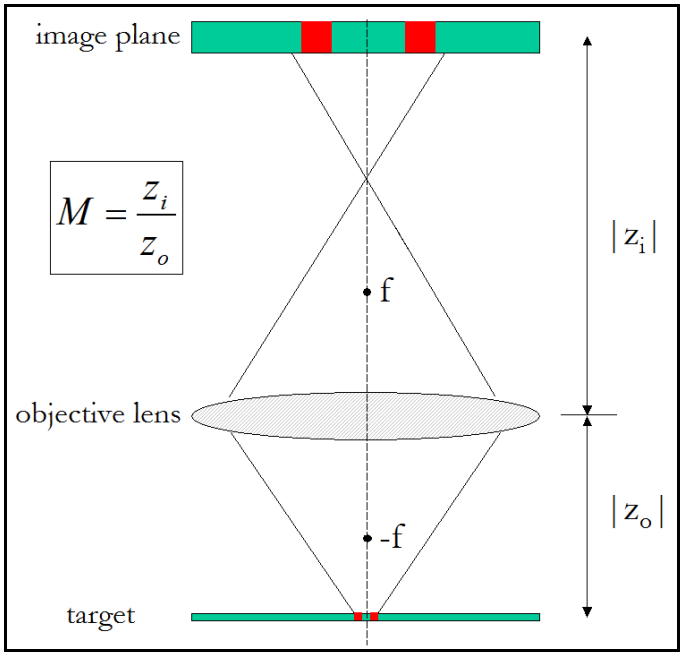

Fig.4.2. Single lens imaging scenario.

The target located at the object plane is illuminated with light focused by the objective lens. The major parameter of the objective lens is the numerical aperture (*NA*) associated with the half-angle θ of the focused light cone:

$$NA = n \sin(\theta) \tag{4.15}$$

where *n* stands for the refraction index of the medium between the objective lens and the target.

It should be emphasized that NA of the illumination beam can differ from the NA of the beam collected by the lens after diffraction from the target. The numerical aperture of the illumination beam determines the observation area, whereas NA of the collected beam implies the resolution limit. However, in many cases both NAs are the same. According to the Rayleigh criterion [**72**], the resolution of a simple imaging system can be approximated by the following formula:

$$R = \frac{\lambda}{2\ NA} \tag{4.16}$$

where NA corresponds to the cone of collected light.

Let us assume for a moment that the target is very thin, so the issue of finite depth of a focal point can be neglected. According to the Fresnel approximation (see Eq.**4.6**), the angular distribution of the light reflected from the target is its Fourier transform. Subsequently, the divergent wavefront of the scattered beam is transformed by the objective lens to a convergent beam (see Eq.**4.12**) and propagation from the objective plane further to the image plane performs the second Fourier transform. Eventually, if the object and image planes satisfy Eq.**4.14**, a magnified and inversed image of the target will be observed. Formally, the whole imaging path can be represented by the following formula:

$$U_i(x,y) = \left\{ \left[U_o(x,y) \otimes h_1(x,y) \right] t_L(x,y) \right\} \otimes h_2(x,y) \qquad (4.17)$$

where $h_1(x,y)$ and $h_2(x,y)$ denote impulse responses (see Eq.**4.5**) of the regions between the target and the objective lens, and between the objective lens and the image plane, respectively.

To summarize this Section, general outline of a simple reflected light microscope system has been presented. Investigation introduced in the next Section is the original contribution of the author of this thesis on the hybrid FDTD-Fresnel modeling of this particular imaging system.

4.4.4 Hybrid FDTD-Fresnel Modeling of the Wide-Field Microscope

Due to the computational limitations mentioned before, let us split the considered scenario, shown in Fig.**4.2**, into two parts, and compute each of them using a different method. The FDTD method will be applied in close vicinity of the target to model the illumination source and collect the field reflected from the target. The rest of the imaging path, through the objective lens to the image plane, will be computed using the Fresnel approximation. The FDTD method can be used to consider an arbitrary geometry of the target, and obtain accuracy that would never be achieved using the method based on the Fresnel approximate approach. However, the cost is in a higher computational effort, and thus the size of the scenario dedicated to the FDTD method should be as small as possible. By contrast, the Fresnel approximation is well suited to model large lens systems in a reasonable time. It provides sufficient accuracy in that kind of applications. The FDTD method brings additional advantage since it allows extraction of the needed properties of the considered target in a wide

spectrum range with only one simulation run. Thus, a single FDTD simulation can deliver input data for several runs of the Fresnel diffraction algorithm, and therefore lower the overall computing time.

Fig.**4.3** depicts the FDTD model defined to investigate the illumination of the target. The light focused by the lens is approximated with a spatially distributed Gaussian beam centered at the target level to obtain the plane wave illumination in the limited region. Hence, a Gaussian beam wall (GBW) is set at some distance above the target to generate a beam propagating downward, driven with a short pulse of a limited spectrum. In principle, the model is very similar to the one introduced in Section 3.5, where the scatterometry issue has been discussed.

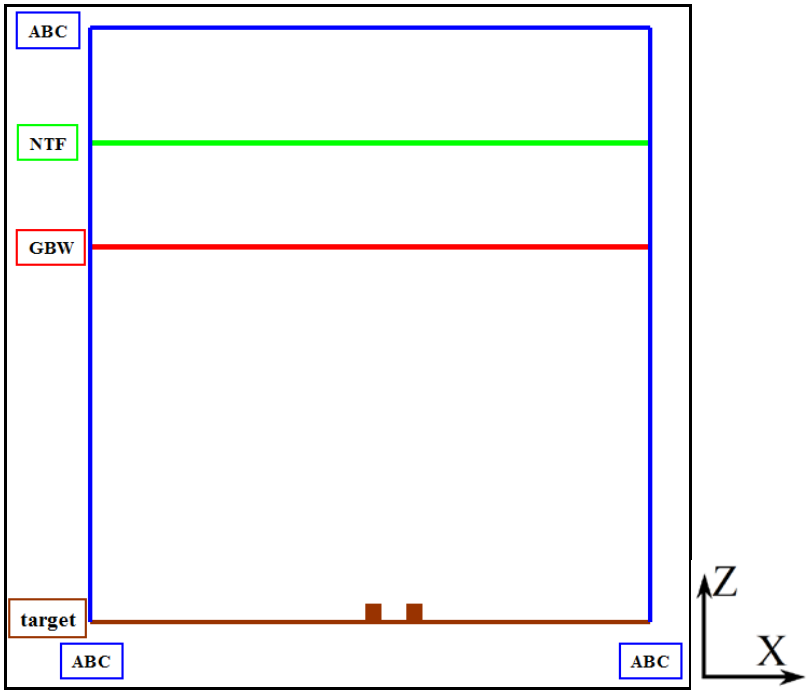

Fig.4.3. FDTD model of EM wave scattering from a target.

Slightly above the GBW, in the scattered field (SF) region, a near-to-far (NTF) transformation plane is set. The role of the NTF transformation is the same as in the case of scattering problems investigated in Section 3.5, as it calculates the angular scattering pattern (ASP) in a far-field zone. Bearing in mind that the objective lens is in the far-field zone of the target, it can be noticed that ASP can provide a field distribution right at the objective plane.

Regarding material properties of the target, there are no specific restrictions imposed by the FDTD method. It can be non-transparent (reflective or lossy) or semi-transparent. In the latter

case, absorbing boundary conditions should be applied also below the target. Any potential restrictions imposed on the target follow from principal limitations of the modeled imaging method.

Let us start the investigation assuming a scalar 2D problem, and thus, reducing the model to the plane shown in Fig.**4**.**2**. It requires shorter computing time and is simpler to interpret than the full 3D problem. In principle, the 2D approximation means that a spherical lens is substituted with a cylindrical one. Although a new wavefront has a different shape, it does not deteriorate formation of the image. Furthermore, the 2D approach implies no field variation perpendicular to the plane of the model, so a 2D Gaussian beam source has to be applied. If TE polarization is considered, the model should be limited to just one layer of FDTD cells placed in the *xz*-plane between two layers of perfect electric conductor (PEC). Alternatively, TM polarization can be investigated if the model is placed between two layers of perfect magnetic conductor (PMC).

The rest of the imaging path, including the lens and the distance to the image plane, is to be processed by an optical algorithm based on the scalar Fresnel approximation. Eq.**4**.**17**, which represents the whole imaging path can be now reduced to the following 2D formula:

$$U_i(f_x) = \Im\left[U_{NTF}(x)\, t_L(x)\right] h_2(f_x) \qquad (\mathbf{4}.18)$$

where $\Im$ denotes the Fourier transform.

The following four steps need to be performed to observe the final image:

1. multiplication of the field distribution $U_{NTF}(x)$ obtained from the FDTD simulation with the lens transfer function $t_L(x)$,
2. Fourier transform of the above product,
3. multiplication of the above with the free space transfer function $h_2(f_x)$,
4. inverse Fourier transform to get the final image.

Considering computational effort needed for execution of Eq.**4**.**18**, it can be noticed that multiplications in the first and the third steps listed above are not very time-consuming, as compared to the Fourier transform, which comprises many multiplication steps. However,

data vectors can be organized in a manner to fit with the FFT algorithm's requirements for efficient execution. At all events, computation time of the scalar Fresnel procedure is of the order of magnitude faster than the FDTD simulation.

4.4.5 Computational Tests

Three types of tests will be carried out to validate the proposed hybrid FDTD-Fresnel algorithm:

1. validation of the Fresnel-based algorithm,
2. tests of the FDTD model,
3. tests of the hybrid FDTD-Fresnel algorithm.

First, let us evaluate the Fresnel procedure implemented by the author of this thesis in Matlab environment[9]. The algorithm based on the Fresnel approach is dedicated to model an optical path in an imaging system from a target to an image plane. Similarly to electronic circuit theory, such a system can be described by its impulse response, which is understood as the image of the isotropic point source [**65**]. Alternatively, a transfer function can be defined, understood as the spatial Fourier transform of the impulse response. For that purpose, let us compute the squared impulse response, usually denoted as a point spread function (PSF) [**65**], of the whole imaging scenario shown in Fig.**4.2**. For the spherical lens applied in the 3D scenario, PSF has the shape of an Airy disc [**65**], due to axisymmetrical shape of the point source. By contrast, in the 2D case the point source is understood as the infinitely long rectangular slit, resulting in PSF having the shape of a sinc function (or a squared sinc function in the intensity scaling)[10].

Let us consider a 2D cylindrical lens of zero thickness (thin lens approximation), made of glass n_s = 1.5, with the focal length of f = 15mm. To obtain a real inverted magnified image, the target should be placed in front of the focal plane. Thus, if the target is set at z_o = 20mm, according to Eq.**4.14**, the image is expected at z_i = 60mm, magnified $|M|$ = 3 times. Let us also assume the operating wavelength of λ = 500nm.

[9] See the listing in Appendix 5.
[10] The intensity is hereafter understood as a square of the electric field intensity.

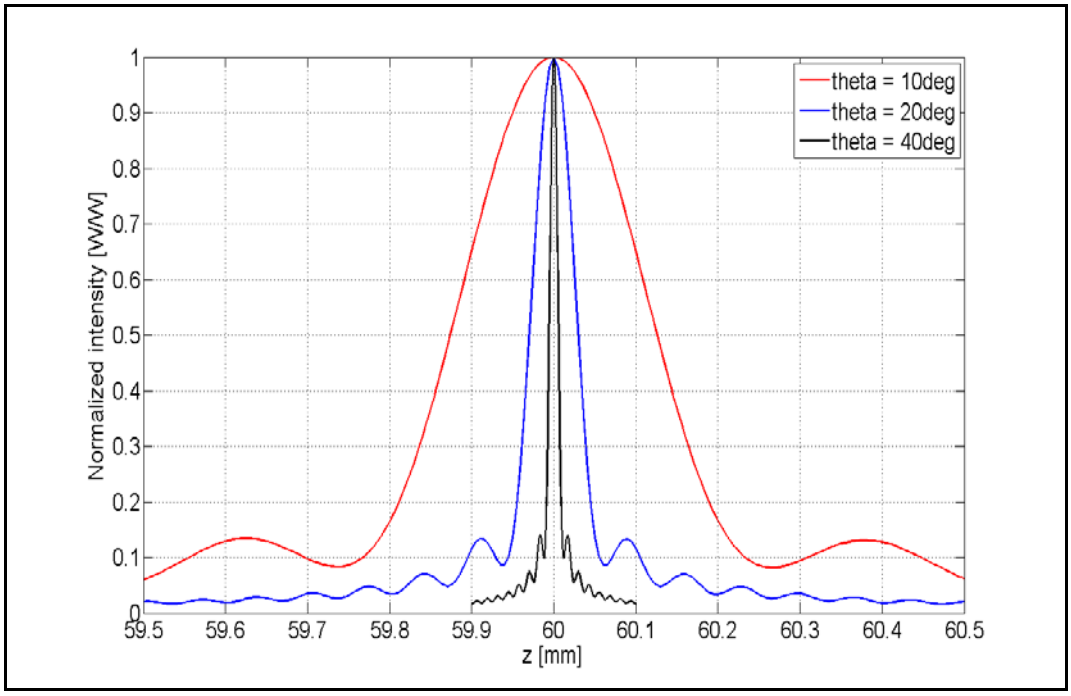

Fig.4.4. Axial distribution of the point spread function.

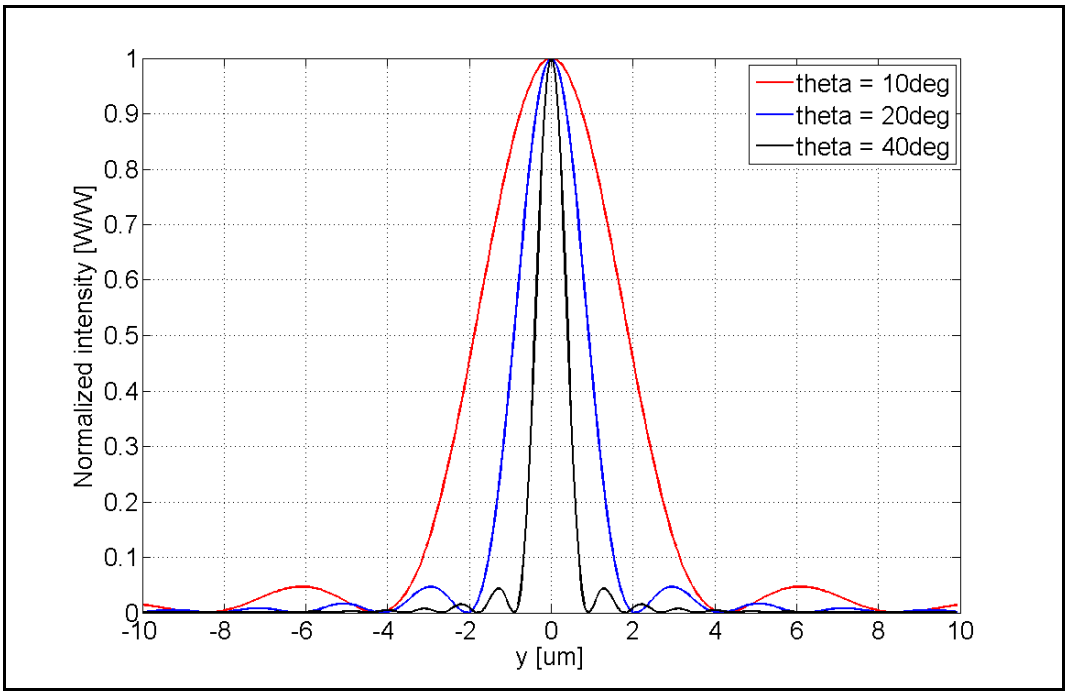

Fig.4.5. Lateral distribution of the point spread function.

In the first test, let us check whether the image is really at the theoretically expected distance from the objective lens, i.e. z_i = 60mm. Thus, the Fresnel algorithm with the isotropic point source placed at the target plane is executed, and the intensity of light along the symmetry axis is scanned. Fig.**4.4** shows the obtained intensity distribution for three values of the

numerical aperture. It can be noticed that the maximum is indeed at the expected distance, and that for increasing NA, the axial resolution of the system increases as well. It is the first validation test, passed successfully by the implemented algorithm. Subsequently, Fig.**4.5** depicts the lateral distribution of PSF at z_i = 60mm for the same set of NAs. As it might be expected, PSF is a squared sinc function. The comparison of both Figures indicates that the lateral resolution is of about one order of magnitude better than the axial one, which is a general property of the wide-field imaging systems.

Table 4.1. Resolution of the images shown in Fig.4.5 compared with theoretical estimations.

θ^0	R_{th} [μm]	R_{fr} [μm]
10	1.44	1.33
20	0.73	0.66
40	0.39	0.30

Table **4.1** presents the obtained resolution (R_{fr}) extracted from the PSF shown in Fig.**4.5** compared with theoretical estimations (R_{th}), calculated according to Eq.**4.16**. The resolution is understood here as the distance from the maximum of PSF to its first minimum, divided by the magnification factor ($|M|$ = 3). Quite a good agreement between both columns can be noticed, especially when bearing in mind that the theoretical resolution R_{th} is just a rough estimation, and it is common practice to add correction coefficients to Eq.**4.16**, depending on a particular imaging system.

As it has already been mentioned, the Fresnel algorithm was implemented with the aid of FFT, so that the length of data vectors has to be a multiple power of 2, in order to meet the requirements of the applied Cooley-Tukey FFT algorithm [**71**]. Additionally, it was assumed that the spatial discretization step should not be larger than 200nm, so as to satisfy the Nyquist's condition at λ = 500nm. Fig.**4.6** shows the measured computation time as a function of NA. As NA increases, the data vector has to be extended to take into account the larger lens diameter. However, it can be noticed that the computation time varies from 100ms for a small NA up to about 2 seconds for a large NA. Blue figures depict the lengths of data vectors, indicating that FFT operates with vectors of about one million samples in a reasonable time.

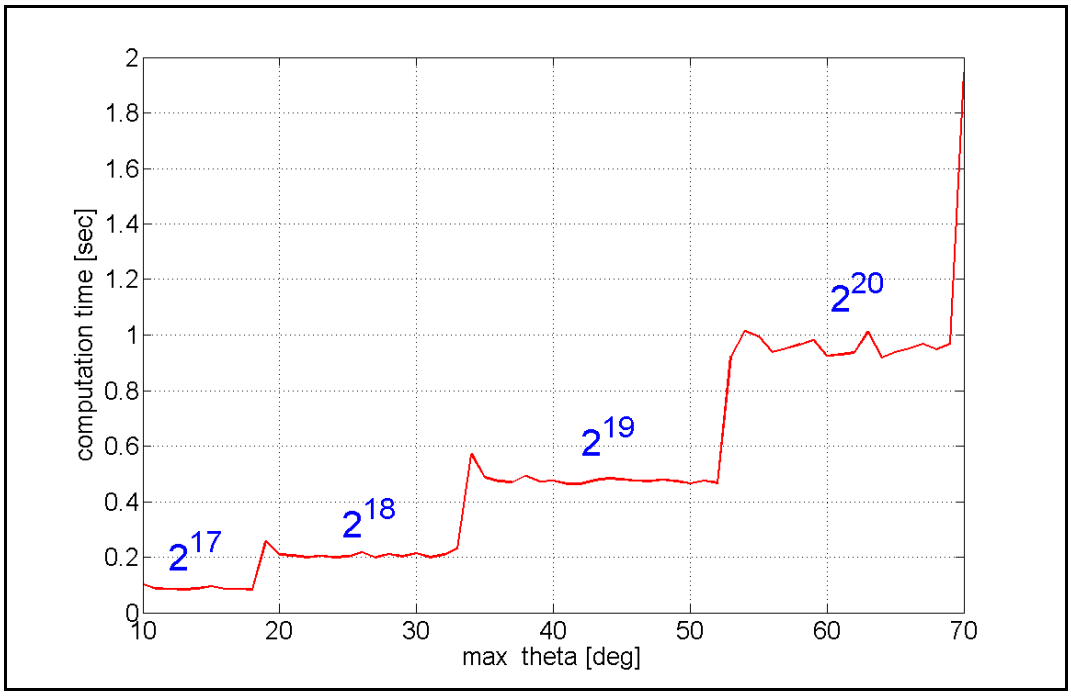

Fig.4.6. Computation time of the point spread function versus NA.

To summarize this part, the Fresnel algorithm has been successfully validated by observing the point spread function of the considered imaging system. Now, computational tests of the FDTD model will be performed.

Let us assume that the target is an isolated 16μm wide plate made of PEC, illuminated with E_z polarized light beam (λ = 500nm) focused by the lens. The beam is approximated with a Gaussian shape having 50μm spot diameter, centered at the target level and driven with a short pulse of even spectrum between 460nm and 540nm. Such a large spot is applied to expose the whole target to the illumination beam. Finite duration of the pulse allows application of the NTF transformation, in order to acquire ASP at the considered wavelength. The FDTD grid size is set to 20nm, to make sure that the numerical dispersion of the FDTD method would not deteriorate the final accuracy. Consequently, in order to satisfy the Courant stability criterion, a time step of 0.04fs is imposed.

The FDTD simulation needs about 2000 iterations to obtain convergent results, whereas the simulation speed reaches about 50 iter/sec[11]. It can also be noticed that the obtained angular scattering pattern, shown in Fig.**4.7**, has the shape of a *sinc* function. As it might be expected, it is the spatial Fourier transform of the field distribution at the target level. The singularities

[11] Intel Core™2 Duo CPU 3.00GHz, 4094MB RAM, 64-bit Windows Vista Business.

observed in the phase distribution are due to the ill-conditioned numerical computation of the phase at the minima of the ASP magnitude. Nevertheless, contribution of these singularities is negligible since the corresponding magnitude approaches zero.

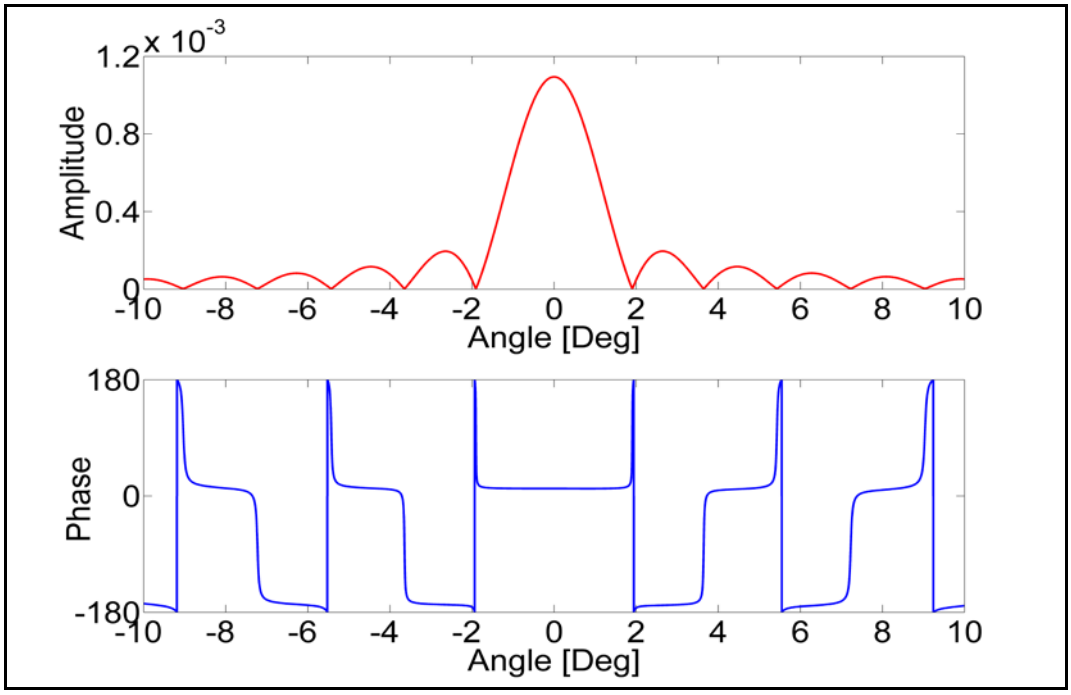

Fig.4.7. Angular scattering pattern of the PEC plate (w=16μm) illuminated at λ=500nm.

Extensive studies of the FDTD model are not necessary at this stage since the issue has already been addressed in Section 4.5. However, once the ASP for the considered target is acquired, it can be coupled with the Fresnel-based algorithm to process the final image.

Regarding the lens imaging scenario, the same values of parameters are chosen as depicted during the tests of the Fresnel algorithm carried before. Numerical aperture of the objective lens is set to NA = $\sin(10^0)$ = 0.1736, so, according to Eq.**4.16**, the resolution of the considered microscope system is expected to be about R = 1.44μm.

The angular scattering pattern is projected from the object plane (y_o = 20mm) onto the front plane of the lens by shifting the phase of ASP. Subsequently, the Fresnel algorithm is executed to calculate the intensity distribution at the image plane (y_i = 60mm). Spatial discretization is set to 107.621nm, so the length of the FFT data vector is N = 2^{16} = 65536. Computing-time is about 100ms, which is less than a percent of the total computing time for the whole hybrid FDTD-Fresnel procedure. Fig.**4.8** presents the obtained image intensity

distribution. Full width at half maximum (FWHM) of linearly scaled image is about 45.8μm, i.e. 2.2μm (4.6%) less than theoretically expected. However, as the physical resolution of the considered microscope system is approximately 1.44μm on the target side, the uncertainty of the FWHM measurement at the image plane is about ±3*1.44μm = ±4.32μm. It indicates that the obtained inaccuracy is within physical limits of the investigated optical system.

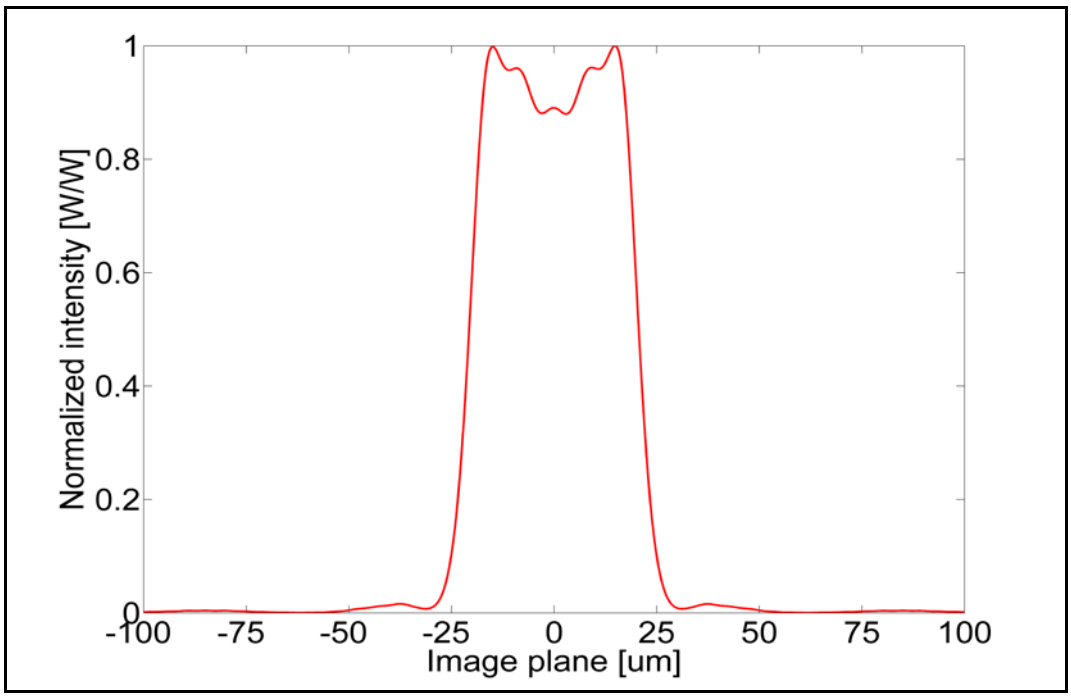

Fig.4.8. Image of the isolated PEC plate (w=16μm) at y_i = 60mm (intensity scaling).

Now, let us consider an image of two isolated PEC plates separated by the varying distance. This time, narrower PEC plates are defined (w = 8μm) to avoid ripples in their images, and the focus is only on the distance between the plates. It enables the comparison of the theoretical magnification and the obtained one. Fig.**4.9** depicts the results for the following set of separations between the plates: 4, 8, 12 and 16 μm. Table **4.2** presents the obtained magnification values, and it can be noticed that the inaccuracy amounts to –12.2, –4.2, –2.0 and 0.0%, respectively. Inaccuracy of the magnification factor has a tendency to decrease as the distance between PEC plates increases since the images of plates located very close to each other produce a disturbed image. Yet, the obtained inaccuracy is still close to the limit of resolving capabilities of the investigated microscope system.

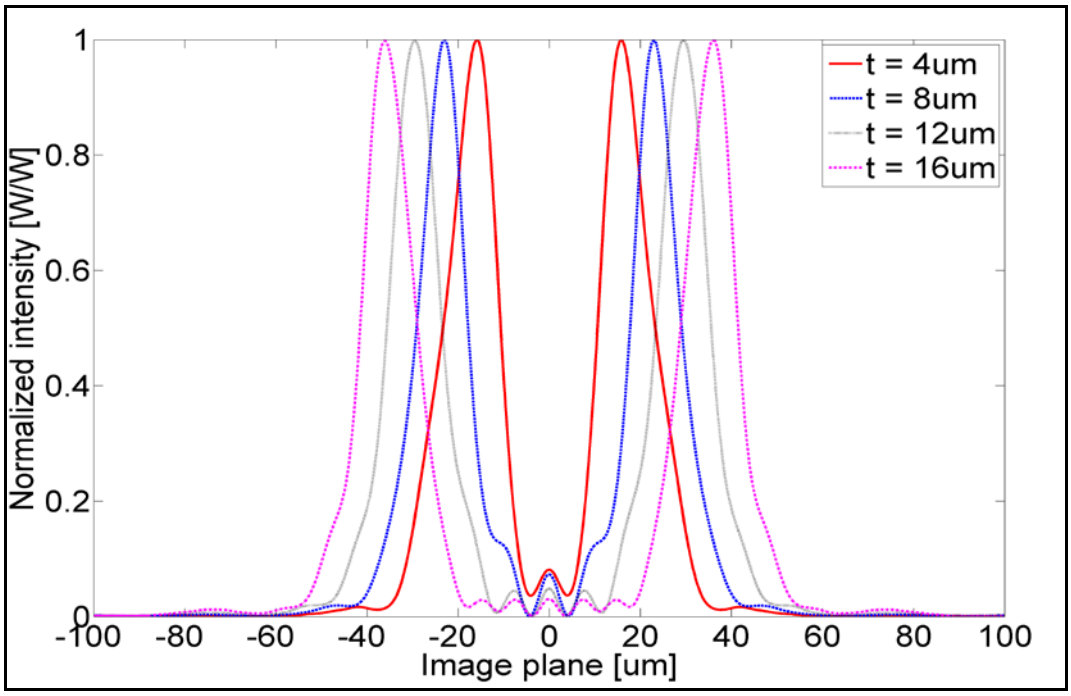

Fig.4.9. Images of two isolated PEC plates (w=8μm) at y_i = 60mm separated by a variable distance (t = 4, 8, 12, 16 μm).

Table 4.2. Magnification of the obtained images as shown in Fig.4.9.

t [μm]	t [μm] @ image plane	Magnicitation
4	10.54	2.635
8	22.99	2.874
12	35.28	2.940
16	48.00	3.000

In the current example, the FDTD cell size and the model size were similar to those in the previous case of an isolated PEC plate, so the computing time of the FDTD solver and the Fresnel procedure were approximately the same.

Let us now extend the problem, assuming that the goal is to collect an image of the PEC plate not at a single wavelength, but within a specified spectrum of visible light. The aim is to indicate advantageous applicability of the FDTD method, which enables collecting scattering patterns for an arbitrary set of discrete frequencies in a single simulation run. Consequently, the only change in the scenario is in the spectrum of the incident light, as shown in Fig.**4.10**, which is wider and can have a user-defined shape. Angular scattering patterns are collected from 450nm up to 750nm with 50nm step. Fig.**4.11** depicts the obtained image, calculated as

the light intensity averaged over the specified seven wavelength points. Width of the imaged plate is 6.75% more than theoretically expected, and ripples are more regular than in case of single wavelength imaging at λ = 500nm. The example indicates the possibilities to apply the presented approach to multi-frequency imaging. However, this subject will not be continued here since it is assumed to be outside the main subject of this thesis.

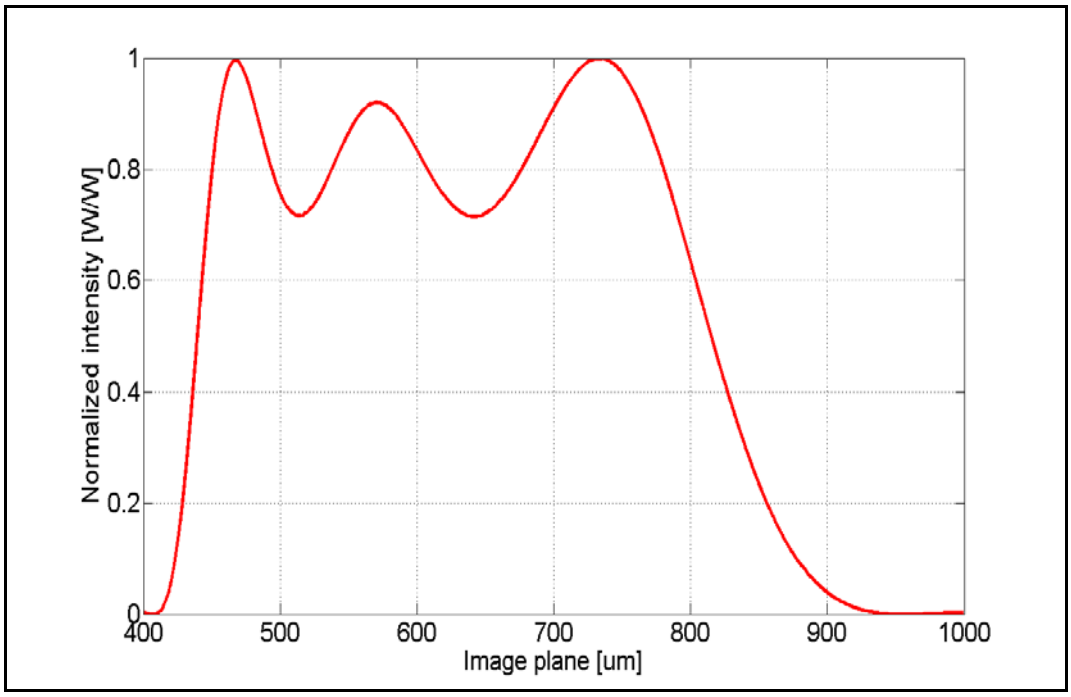

Fig.4.10. Normalized spectrum of the illumination plane wave (power scaling).

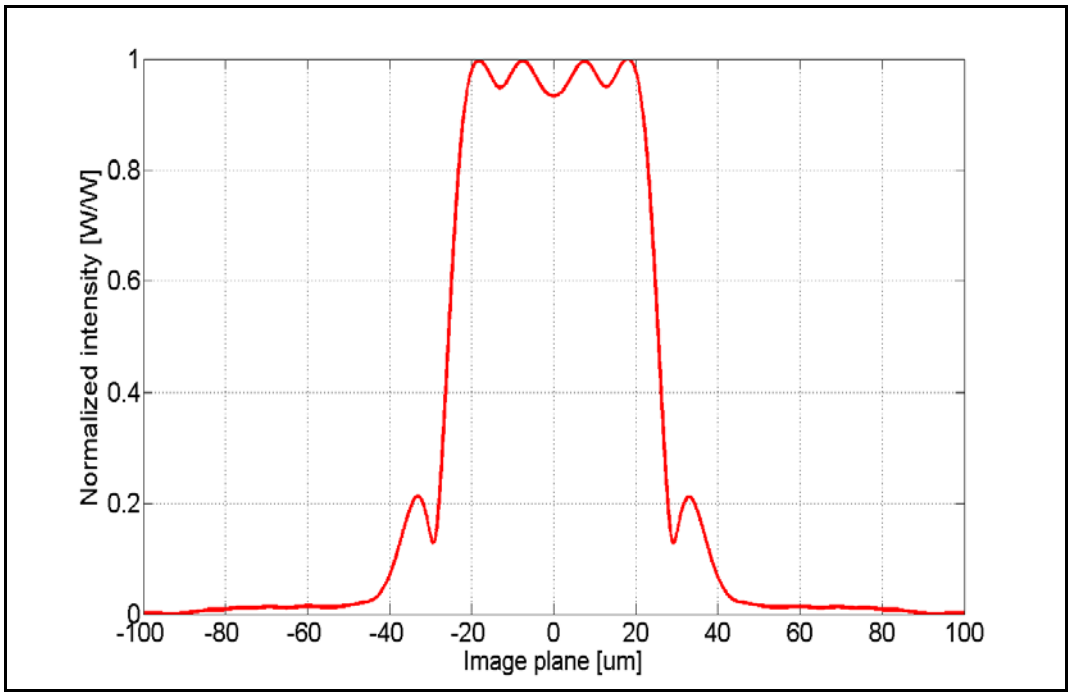

Fig.4.11. Image of the isolated PEC plate (w=16μm) at y_i = 60mm (λ = 450:50:750nm).

Major limitation of the wide-field microscope systems consists in a relatively large depth of focus (DOF), caused by a large illumination spot focused by the objective lens at the target level. In consequence, the axial resolution of the method is worse than the lateral one, which makes the tool rather incapable of resolving the shape of a thick target (specimen). The next Section concentrates on the extension of classic microscope system which provides an increased axial resolution. The confocal scanning microscopy will be considered.

4.5 Hybrid FDTD Modeling of the Confocal Microscopy

The concept of confocal microscope was originally introduced in 1957 by Marvin Minsky as he tried to increase the contrast of the conventional optical microscope by putting pinholes to eliminate out-of-focus light. It allowed him to construct a system which has gained a very wide applicability nowadays, especially to the inspection of biological tissues or semiconductor devices. There are several versions of the confocal scenarios but, without loss of generality of the conclusions, the study presented in this Section will be concentrated on the simplified scenario, in order to check the possibility of applying the FDTD method in the modeling of that concept. The author's work described hereafter has been originally published in [**69**]. Let us first introduce the investigated scenario with some essential comments.

4.5.1 Introduction to the Confocal Microscopy

The scenario of the confocal microscope is very similar to the wide-field one, shown in Fig.**4.2**. The major difference is in the image processing. Fig.**4.12** shows a schematic view of a typical confocal scanning microscope in the illumination (left view) and scanning (right view) modes. The light radiated by the source illuminates an input pinhole, which spatially restricts the amount of passing light, whereas the objective lens focuses the beam of light at the target plane. Since the input pinhole plane and the target plane are conjugate planes [**78**], an image of the pinhole is observed at the target plane. Thus, if the pinhole is getting smaller, the spot becomes - within diffraction limit – smaller as well. Subsequently, the light reflected from this small fraction of the target propagates back through the lens to the image plane, where another pinhole is set. Such a scenario has two major advantages. First, the input pinhole allows reducing the size of the spot at the target plane. Thus, the light diffracts only from a tiny part of the target, increasing the spatial contrast of the final image. Afterwards, reflected light is refocused by the objective lens onto the image plane (see red line in

Fig.**4.12**), where the output pinhole limits the amount of light collected by the detector. In consequence, the light scattered from different parts of the target or at different levels (see blue line in Fig.**4.12**) is focused outside the output pinhole, reducing the contribution of the out-of-focus light to the power collected by the detector. The aforementioned procedure implies that a whole confocal microscope operates like a scanner which selectively probes the target point by point. By performing several measurements for different positions of the target a 3D image can be acquired.

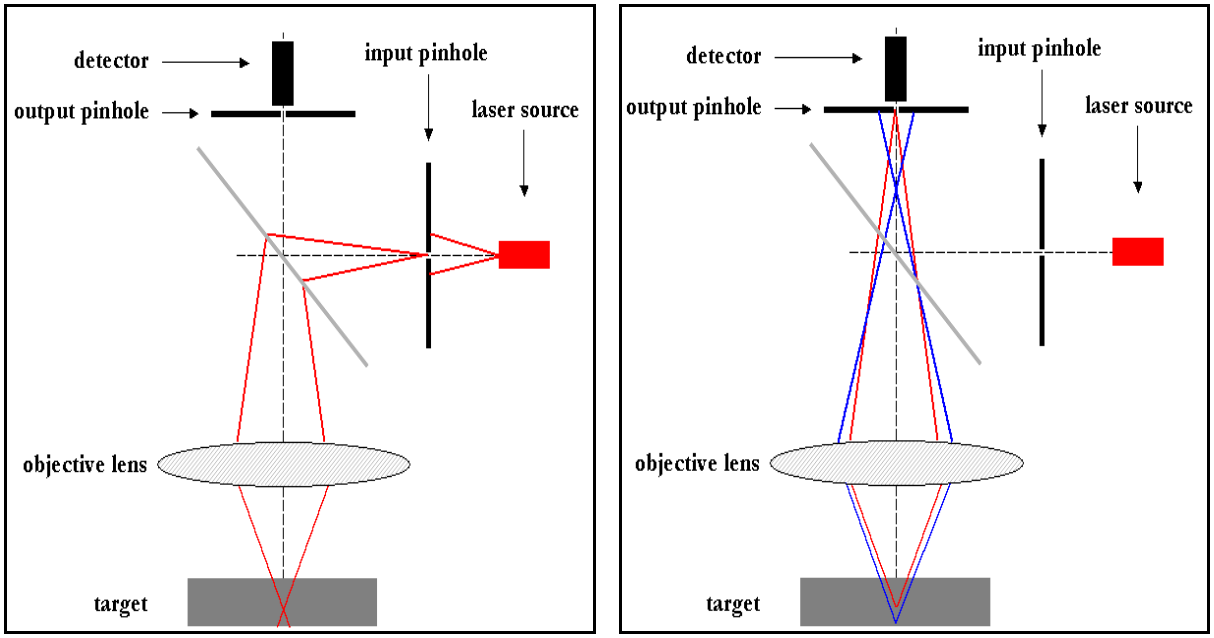

Fig.4.12. Scenario of confocal scanning microscope (illumination mode – left, scanning mode - right).

As opposed to the concept of wide-field microscope, both axial and lateral resolutions are of great interest in the confocal microscopy. They can be evaluated from the point spread functions of the illumination and detection paths (see Fig.**4.12**). Convolution of both PSFs gives a point-spread function of the whole system [**79**]. Topography and electric properties of the target also have an impact on the resolving capabilities, but it is usually assumed to be negligible. However, irrespective of the width of PSF_{ill} and PSF_{det}, the total PSF is always narrower. Assuming, for the sake of simplicity, that the output pinhole is larger than the input one, it can also be assumed that the final resolution depends mainly on the illumination path, as the PSF_{ill} dominates.

Similarly to the hybrid FDTD-Fresnel modeling of the wide-field microscope described in the previous Section, the FDTD model is reduced to the close vicinity of the target (see Fig.**4.3**) and a Gaussian shape is applied to approximate the illumination beam. In the 3D scenario, advantage of Eq.**4.16** is usually taken to calculate NA for the aimed lateral resolution. This time the procedure is a bit different since the radius of the Gaussian spot should be determined from the aimed axial resolution, rather than the lateral one. Axial and lateral resolutions are understood hereafter as a full width at half maximum (FWHM) of a 2D Gaussian beam in the axial and lateral planes, respectively. Let us then derive a relation between a 2D Gaussian beam spot radius w_0 and the numerical aperture *NA* of the represented light beam.

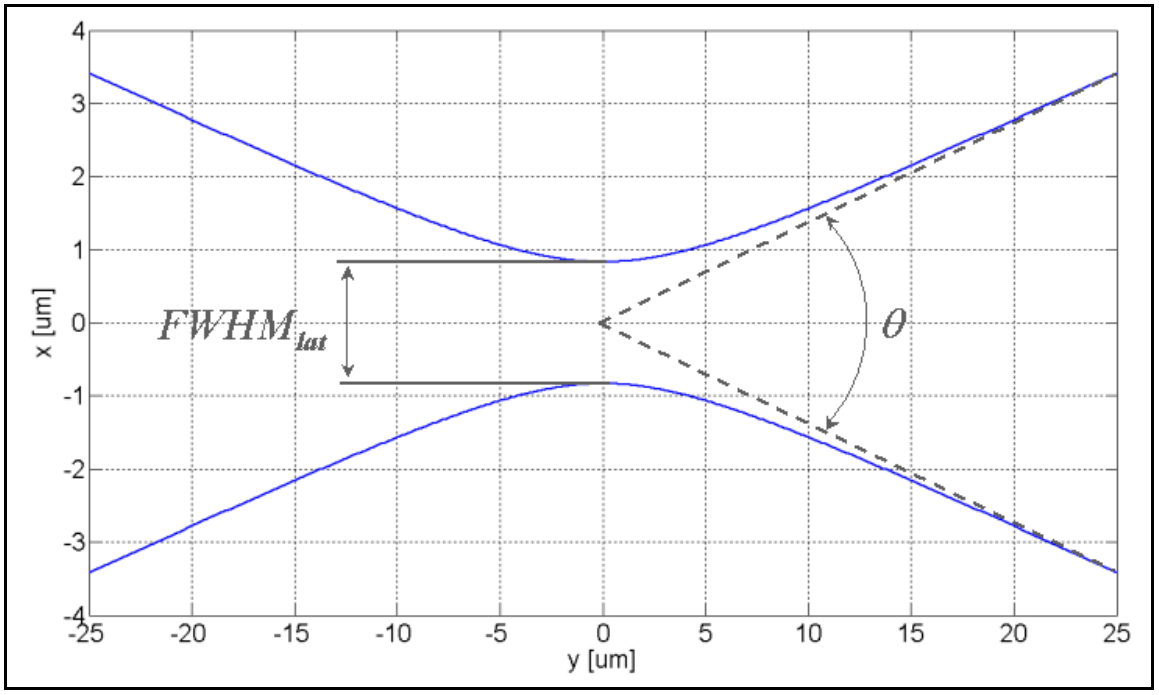

Fig.4.13. Divergence angle θ of a Gaussian beam.

Fig.**4.13** shows a 3D/2D Gaussian beam shape with the approximate divergence angle θ indicated. Following Eq.4.47, which describes a 2D Gaussian beam distribution, an approximate formula for a 2D Gaussian beam envelope valid far from the focal plane ($y >> y_0$) can be derived:

$$E_{FAR} \cong E_0 \sqrt{\frac{y_0}{y}} \exp\left[-\left(\frac{x}{w_0}\frac{y_0}{y}\right)^2\right] \qquad (\mathbf{4}.19)$$

Furthermore, let us derive from the above formula the lateral FWHM of a Gaussian beam far from the focal plane:

$$FWHM_{lat,FAR}(y) \cong w_0 \sqrt{\ln 2}\, \frac{y}{y_0} \tag{**4**.20}$$

Thus, the numerical aperture NA is given as follows:

$$NA \cong \sin\theta = \frac{0.5\, FWHM_{lat,FAR}(y)}{\sqrt{y^2 + 0.25\, FWHM_{lat,FAR}(y)}} = \left[1 + \left(\frac{y_0}{w_0}\right)^2 \frac{1}{\ln 2}\right]^{-0.5} \tag{**4**.21}$$

However, the aim is to relate NA with the axial resolution R_{ax} ($FWHM_{ax}$) of a 2D Gaussian beam, which is given as follows:

$$R_{ax} = FWHM_{ax} = 2\sqrt{15}\; y_0 \tag{**4**.22}$$

Introducing Eqs.4.48,49 and **4.22** into Eq.**4.21** leads to the following relations for the numerical aperture and spot radius, respectively (compare Eq.**4.15**):

$$NA = \left[1 + \frac{R_{ax}}{\lambda} \frac{\pi}{2\sqrt{15}\ln 2}\right]^{-0.5} \tag{**4**.23}$$

$$w_0 = \sqrt{\frac{R_{ax}\,\lambda}{2\pi\sqrt{15}}} \tag{**4**.24}$$

To summarize this Section, application of input and output pinholes allows achieving increased image contrast, especially in the axial plane, improving the determination of a 3D shape of the target. It should be emphasized, however, that confocal microscopy is a sequential image processing method, as it acquires the whole image pixel by pixel.

4.5.2 Hybrid FDTD-Fresnel Modeling of the Confocal Microscope

Hybrid FDTD-Fresnel modeling has already been discussed in Section **4**.**4**.**4**. Hence, the only modifications to the hybrid algorithm necessary to properly represent the investigated problem will be indicated below. The FDTD model is exactly the same as shown in Fig.**4**.**3**. Each simulation run provides, as an outcome, the angular scattering pattern, which is further processed by the Fresnel-based algorithm onto the image plane. The major discrepancy is in the different postprocessing of the data obtained from the FDTD simulations since the whole image is acquired from a pixel-by-pixel execution of several simulations for different centering of the illumination spot. Regarding illumination source, the Gaussian spot has to be much narrower than in the wide-field microscope model, so as to resemble the existence of the input pinhole, which is imaged at the target level.

4.5.3 Computational Tests

Let us consider two complementary targets: a trench and a line processed in a bulk of GaAs wafer (ε_r = 10.4976). The height and width of the trench (line) are the same and amount to 10μm, whereas the length of the trench (line) extends to infinity. An image will be processed at λ = 500nm. Assuming that the target is z_o = 2mm from the objective lens and the image plane is z_i = 200mm behind the lens, the focal length amounts to f = 1.98mm.

Since the FDTD model is exactly the same as for the wide-field imaging, basic tests of the imaging path will be abandoned here. It has been assumed that the spatial discretization step should not be larger than 200nm, so as to satisfy the Nyquist's condition at λ = 500nm.

Another step is to choose the expected axial resolution of the imaging system, which will further allow establishing the radius of the illumination spot (see Eq.**4**.**24**) and the width of the output pinhole. Hence, let us set axial resolution to R_{ax} = 2μm. Thus, according to Eq.**4**.**23**, numerical aperture amounts to NA = 0.547 ($\theta \approx 33^0$) and, consequently, the Gaussian beam radius is w_0 = 0.203μm. The same NA will be set for the detection mode.

Let us now compute a point spread function of the detection path (see Fig.**4**.**14**). The distance between the first minima of the PSF is about 108μm, and this value will be set as the width of the output pinhole.

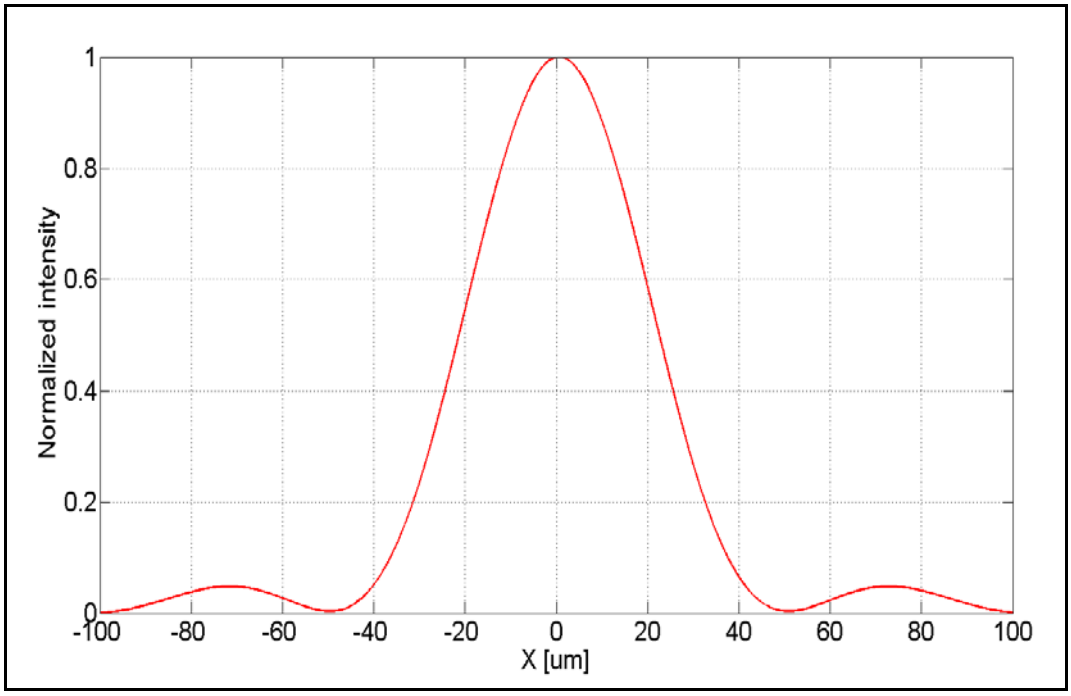

Fig.4.14. Point spread function of the detection path.

Regarding the FDTD model, it is two-dimensional and consists of one FDTD layer of the target's cross-section, assuming no field variation along the trench (line). It indicates that illumination plane is perpendicular to the trench (line). The analysis will be confined to the transverse electric (TE) polarization, with electric field perpendicular to the illumination plane. The minimum FDTD cell size is set to 10nm maintaining at least 15 FDTD cells per operating wavelength (λ = 500nm). The whole FDTD model is 40μm long, which ensures that the excited Gaussian beam and the scattered field do not exceed the computational area.

A single FDTD simulation takes about 5 minutes[12]. The whole image has been computed with a 1μm step, although, due to the symmetry of the targets, only a half of each image has been collected. Thus, the total FDTD computation time amounts to 286x5min ≅ 24h. Finally, all the obtained ASPs serve as the input to the Fresnel-based algorithm, which takes only several seconds, making a minor contribution to the total computational effort of the hybrid modeling method.

Fig.**4.15** shows the obtained images of the trench (left) and the line (right). It can be noticed that the image resembles target's shape, although, as might be expected, the axial resolution is a bit worse, resulting in blurred horizontal edges. Another interesting phenomenon can be

[12] Intel Core™2 Duo CPU 3.00GHz, 4094MB RAM, 64-bit Windows Vista Business.

seen at the sharp corners of the trench (line). Due to significant diffraction of the incident light at the corners of trench (line), dark vertical gaps can be observed in both images around x = -5μm and x = 5μm.

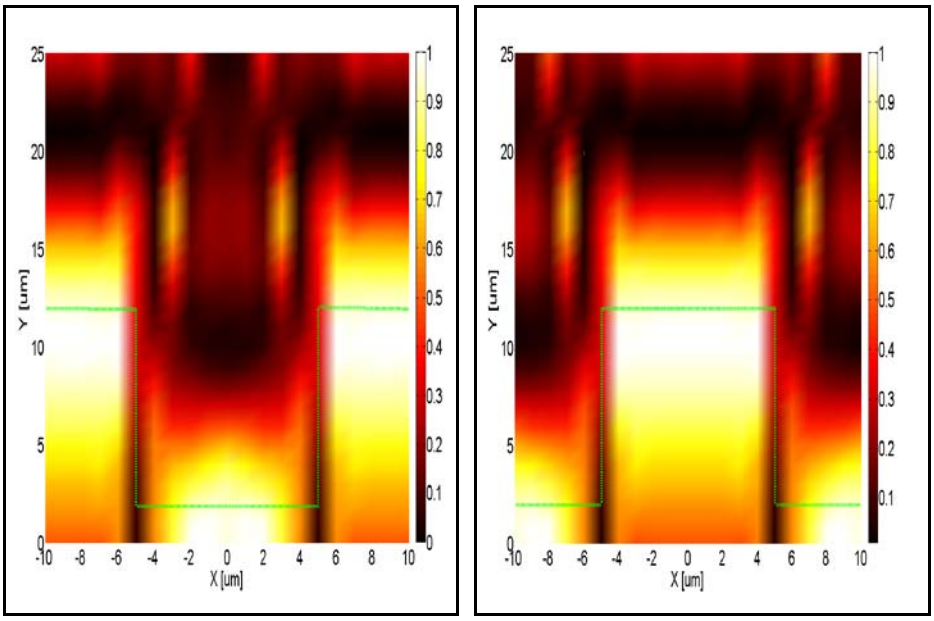

Fig.4.15. Image of the trench (left) and the line (right) with the green dotted line depicting the real shape of the target.

To sum up this Section, hybrid FDTD-Fresnel modeling was successfully validated and proved to be an advantageous technique in the modeling of the confocal microscope. It allows the acquisition of a 3D shape of the considered target.

4.6 Summary

Microscope imaging scenarios, investigated in this Chapter, were simplified in a large extent, as compared to the modern imaging tools, which are often very sophisticated. Nevertheless, the technique introduced in this Chapter can be easily extended to more advanced and complicated scenarios, both in the FDTD and Fresnel regions. It has been shown that the hybrid FDTD-Fresnel approach can be very advantageous in the modeling of the far-field optical imaging, where the first method cannot handle such computationally large problems, whereas the second one can fail when the target has a complicated shape. It can be concluded that the study presented in this Chapter fully proves the second statement of the thesis formulated in Chapter 1.

Chapter 5

Near-to-Near Transformation in Axisymmetrical Structures

5.1 Introduction

It is well known that a complicated radiating structure can be fully characterized by a set of electric and magnetic surface currents placed at a closed surface surrounding the structure (often called the Huygens surface). Knowledge of these currents (directly related to electric and magnetic fields tangential to the surface) is sufficient to calculate electromagnetic fields in any test point placed outside the Huygens surface. Most often that kind of approach is used to perform the so-called near-to-far (NTF) transformation, consisting in calculation of the fields in the far zone. In NTF transformation, it can be assumed that:

- all straight lines traced between the test point and any point of the Huygens surface are parallel,
- fields in the test point do not have radial field components, where "radial" relates to the spherical coordinate system[13] with the origin situated inside the Huygens surface,
- the distance between the surface current at the Huygens surface and the test point influences the phase but not the amplitude of the relative contribution of that current to the field in the test point.

The above assumptions simplify the calculation of the fields in the test point. However, if test point is relatively close to the Huygens surface, these assumptions cannot be accepted. In such a case, a much more complicated procedure of calculating fields in the test point has to be applied. In other words, the so-called near-to-near (NTN) transformation has to be applied.

[13] See Appendix 3.

In the case of axisymmetrical problems, denoted also as body of revolution (BOR) problems, the formulae for numerically effective application of NTF transformation are well known [**80**],[**81**],[**82**] and applied in commercial software for a long time. In the case of NTN transformation, the classic approach consists in applying a direct integration of contributions of the surface currents (placed on cylindrical Huygens surface) in a 3-D space. Such an approach takes no advantage of the analytically known angular dependence of the currents on that surface, so computation becomes numerically very ineffective.

This Section describes the new approach to the problem, leading to a very effective numerical algorithm. That approach is an original contribution of the author of this thesis. Its highlights were first presented in [**83**].

5.2 Basic Concept

Axisymmetrical antenna problems are of high importance in the engineering practice. For instance, corrugated circular waveguide horns or biconical antennas may be recalled. These horns are often employed as feeds of larger, but also axisymmetrical reflectors. In general, angular dependence of EM field in axisymmetrical structure may be decomposed into the following series, given in cylindrical coordinates[14]:

$$\vec{E}(\rho,\phi,z)=\sum_n \vec{E}_n(\rho,z)\sin(n\phi)+\vec{E}'_n(\rho,z)\cos(n\phi) \tag{5.1}$$

In most practical cases, BOR structures are excited by field patterns of a specific value of n. Typical example is the circular waveguide mode H_{11} with n=1. With such an excitation, all the field components inside a BOR structure are proportional to $\cos(n\phi + \phi_0)$, with ϕ_0 dependent on coordinates ρ and z. A 3D problem can be reduced to a 2D one with all EM components present. Such problems are usually referred to as vector 2D (V2D) in the cylindrical coordinate system [**6**], [**84**], [**85**].

The major advantage of V2D over 3D approach to BOR problems is that it is much faster and requires much less computer memory to solve the problem. The difference in both speed and memory requirements may reach even two orders of magnitude, which is why V2D enables to

[14] See Appendix 4.

handle designs that are out of reach for up-to-date 3D EM solvers. Its axisymmetrical version has been implemented in several methods, such as the Method of Moments (MoM) [**86**] or FDTD [**6**]. Numerical solvers based on such methods often support NTF transformation, which provides far field zone radiation pattern. If the 3D approach is considered, the antenna is surrounded by cylindrical NTF surface (Huygens surface), where EM field is recorded. Next, following the equivalence principle, all EM field components are replaced with electric and magnetic surface currents, which are subsequently used to obtain electric field in a far field test point. In the case of V2D BOR approach, it is sufficient to record the field distribution only in one specified cross-section of the structure since it can be analytically expanded to the entire NTF cylinder, using either $sin(n\phi)$ or $cos(n\phi)$ multiplication (see Fig.5.1). With the known analytical dependence on ϕ angle spanned from 0 to 2π, integration of electric (magnetic) current can be proceeded over Δz on the side of the NTF cylinder, or $\Delta\rho$ on the cylinder bottoms. It indicates that in V2D BOR FDTD algorithm, each surface element of NTF line expanded over the whole range of ϕ angle forms a circular loop. Thus, it makes the problem similar to the calculation of fields radiated by the current loop.

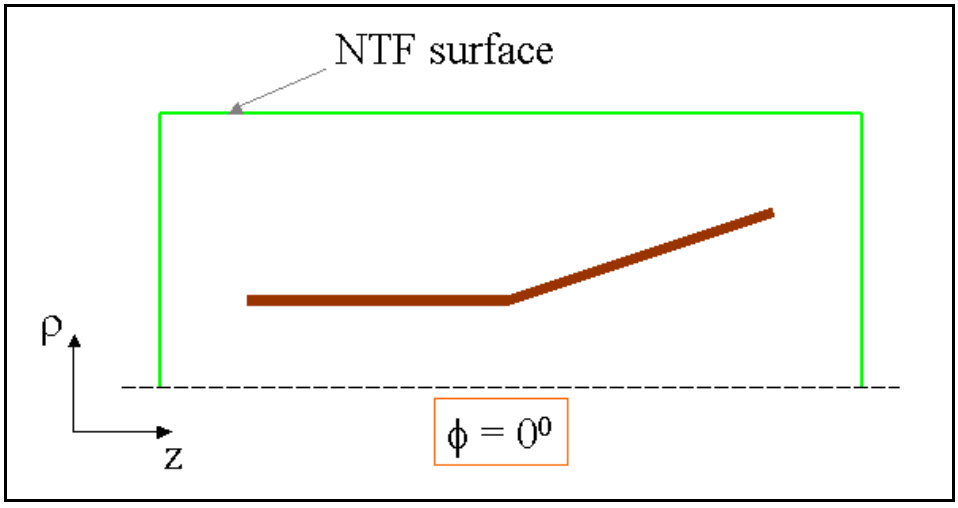

Fig.5.1. NTF surface surrounding V2D BOR FDTD model of axisymmetrical antenna.

NTF transformation is very useful and widely applicable in EM modeling of radiation problems. However, sometimes it is not sufficient if the observation point is still in the near field zone. For instance, parabolic antenna with off-axis axisymmetrical feed may be quoted. Since there is no common axis of symmetry, the whole antenna system cannot be modeled as a V2D model. Nevertheless, a model of the feeding antenna can be prepared to find the radiation pattern. Afterwards, a simulation of the reflector dish can be run, with illumination

signal derived from the previously obtained radiation pattern. However, sometimes it cannot be assumed that the reflector is in the far field zone of the feeding antenna. In such a case, NTN transformation may be applied in the feed model to obtain distribution of the field that illuminates reflector.

In principle, BOR NTN transformation can proceed in a similar manner to BOR NTF one with the Huygens surface reduced to just 3 segments (see Fig.5.1). However, NTN transformation is more complicated than NTF method since the latter one needs only two electric field components E_ϕ and E_θ to be calculated at the test point, as the radial component does not appear. Moreover, magnetic field is straightforward related to electric one by the free space impedance. As it has been pointed out earlier in this Chapter, in NTF transformation some additional approximations can be made, assuming that each point on the NTF surface is seen under the same angle at the observation point. On the contrary, NTN transformation imposes calculation of all 6 EM components, without any approximations allowed for NTF transformation.

Before moving on to the method proposed by the author of this thesis, let us discuss a straightforward approach to BOR NTN transformation. The concept consists in using BOR calculation results to collect surface currents on the pickup NTN surface that surrounds radiating antenna. Then, to obtain the appropriate field component at the test point, a direct integration of the contribution of these surface currents needs to be performed. However, although such an approach is robust, it requires a lot of computational effort. Hence, it is natural to look for a more effective BOR NTN transformation that takes the advantage of analytically known axial dependence of EM fields (see Eq.**5.1**). To the knowledge of the author of this thesis, his paper [**83**] was the first publicly available consideration of this issue.

Douglas Werner [**87**] introduced an exact integration procedure for vector potentials generated by current flowing in a thin circular loop antenna. He considered the current naturally oriented along ϕ angle, described by:

$$I(\phi') = I_{\phi n} \cos(n\phi') \tag{**5**.2}$$

where prime superscript denotes the source coordinates.

Werner's approach is valid in both near and far field zones, and for arbitrary radius a of the current loop antenna. Later, he extended these results to moderately thick cylindrical wire antennas [**88**]. Both solutions refer to the radiation of EM fields into unbounded free space. It should also be mentioned that Li et al. [**89**] presented an alternative approach, based on dyadic Green's function with separate solutions for regions, where $0 \le r \le a$ and $r > a$.

Let us note that in the BOR NTN transformation, in each of the observation points contributions of three electric I_ρ, I_ϕ, I_z and three magnetic K_ρ, K_ϕ, K_z current components, located at the pick-up surface surrounding radiating object, need to be calculated. Werner's formulas enable calculation of the contribution of $I_\phi(\phi')$ component for the specified (ρ, z) coordinates, and by virtue of duality this can also be extended to $K_\phi(\phi')$. To obtain a complete NTN solution, the method needs to be extended to the remaining components.

5.3 Theoretical Background

As it has already been mentioned, the theoretical background of the analysis below is based on the approach proposed by Werner [**87**]. Let us briefly address the relevant issues here. A view of the considered circular loop antenna is shown in Fig.5.2.

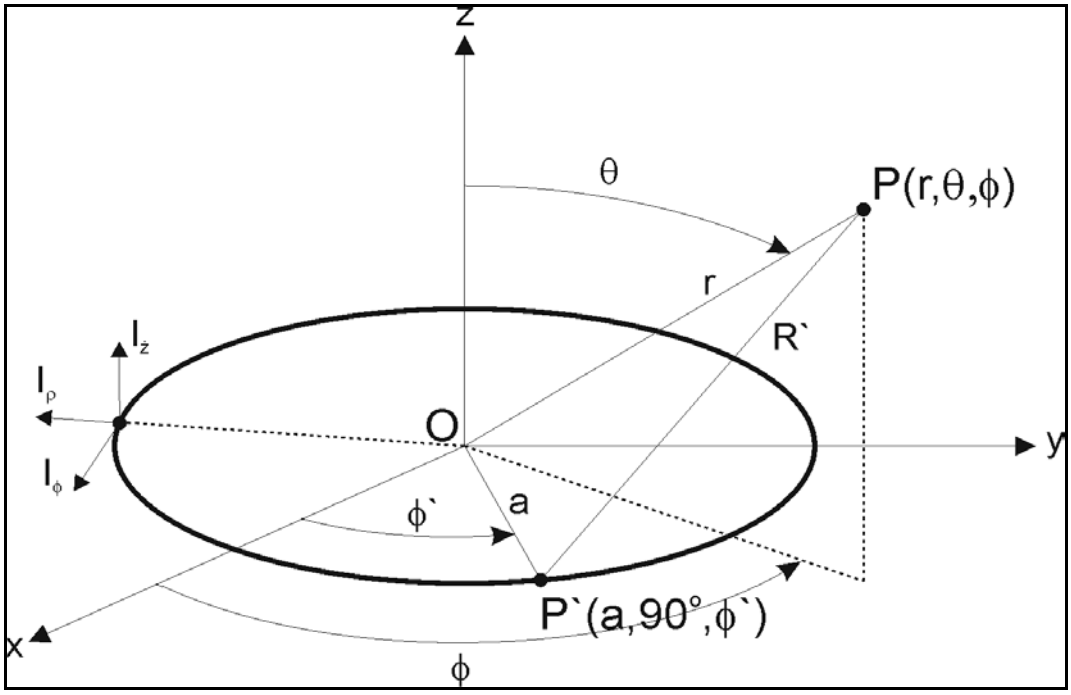

Fig.5.**2. Current loop antenna.**

First of all, a vector potential ***A*** is employed to describe EM field components:

$$\vec{H} = \frac{1}{\mu} \nabla \times \vec{A} \tag{5.3}$$

$$\vec{E} = \frac{1}{j\omega\varepsilon} \nabla \times \vec{H} \tag{5.4}$$

Let us recall that the vector potential ***A*** is related to the source current by the following formula [**73**]:

$$\vec{A} = \frac{\mu}{4\pi} \iiint_V \frac{\vec{J}(R')}{R'} dv' \tag{5.5}$$

Assuming spherical coordinates notation, magnetic and electric field components are related to the vector potential ***A*** via the following formulae:

$$H_r(r,\theta,\phi) = \frac{1}{\mu r \sin\theta} \left[\frac{\partial}{\partial\theta} (\sin\theta \, A_\phi) - \frac{\partial}{\partial\phi} A_\theta \right] \tag{5.6}$$

$$H_\theta(r,\theta,\phi) = \frac{1}{\mu r} \left[\frac{1}{\sin\theta} \frac{\partial}{\partial\phi} A_r - \frac{\partial}{\partial r} (r \, A_\phi) \right] \tag{5.7}$$

$$H_\phi(r,\theta,\phi) = \frac{1}{\mu r} \left[\frac{\partial}{\partial r} (r \, A_\theta) - \frac{\partial}{\partial\theta} A_r \right] \tag{5.8}$$

$$E_r(r,\theta,\phi) = \frac{\eta}{j\beta r \sin\theta} \left[\frac{\partial}{\partial\theta} (\sin\theta \, H_\phi) - \frac{\partial}{\partial\phi} H_\theta \right] \tag{5.9}$$

$$E_\theta(r,\theta,\phi) = \frac{\eta}{j\beta r} \left[\frac{1}{\sin\theta} \frac{\partial}{\partial\phi} H_r - \frac{\partial}{\partial r} (r \, H_\phi) \right] \tag{5.10}$$

$$E_\phi(r,\theta,\phi) = \frac{\eta}{j\beta r} \left[\frac{\partial}{\partial r} (r \, H_\theta) - \frac{\partial}{\partial\theta} H_r \right] \tag{5.11}$$

where η denotes intrinsic impedance of the surrounding medium (the air is assumed in this consideration).

Werner proposed to express this vector potential using the following integral:

$$\Im(r,\theta,\phi)=\frac{1}{2\pi}\int_0^{2\pi} I(\phi')e^{-j\beta R'}d\phi' \tag{5.12}$$

$$R'=\sqrt{R^2-2ar\sin(\theta)\cos(\phi-\phi')} \tag{5.13}$$

where: β is the free space phase constant, R' is the distance from the source point P`$(a,90^o,\phi')$ to the test point P(r,θ,ϕ) as shown in Fig.5.2 and:

$$R=\sqrt{r^2+a^2} \tag{5.14}$$

Subsequently, using Lommel's expansions and Euler's identity, Werner derived an exact series expansion of the integral (Eq.**5.12**) as follows:

$$\Im(r,\theta,\phi)=I_0e^{-j\beta R}+\sum_{m=1}^{\infty}\sum_{n=0}^{\infty}A_{mn}I_n\cos(n\phi)\frac{\left(\beta^2 ar\sin(\theta)\right)^m}{m!}\frac{h_{m-1}^{(2)}(\beta R)}{(\beta R)^{m-1}} \tag{5.15}$$

where

$$A_{mn}=\begin{cases}0 & m<n\\ \dfrac{1}{2^m}\binom{m}{k}, & m\geq n \quad and \quad m-n=2k\\ 0 & m>n \quad and \quad m-n=2k+1\end{cases} \tag{5.16}$$

and $h_m^{(2)}(\beta R)$ is the 2nd kind Hankel function of the mth order.

Afterwards, Werner applied this expansion to evaluate exact formulae for the vector potential components A_r, A_θ, A_ϕ, given in the spherical coordinates[15]. Eventually, electric and magnetic components can be evaluated at the test point using Eqs.**5.3**,**4**. Werner restricted his investigation to one polarization of the current. In the next Section, the contributions of other current components, i.e.:

[15] See Appendix 3.

$$I_\rho(\phi') = I_{\rho n}\cos(n\phi') \tag{5.17}$$

$$I_z(\phi') = I_{zn}\cos(n\phi') \tag{5.18}$$

will be thoroughly investigated.

5.4 Radial Current Component

Let us express radial current component (Eq.**5.17**) in the spherical coordinates by employing unit vectors at the test point P(r,θ,ϕ):

$$I_\rho(\phi') = \hat{a}_r I_\rho \sin(\theta)\cos(\phi-\phi') + \hat{a}_\theta I_\rho \cos(\theta)\cos(\phi-\phi') - \hat{a}_\phi I_\rho \sin(\phi-\phi') \tag{5.19}$$

If we substitute Eq.**5.19** to Eq.**5.5**, three components of the vector potential are obtained:

$$A_r(r,\theta,\phi) = \frac{\mu a \sin(\theta)}{4\pi}\int_0^{2\pi} I_\rho \cos(\phi-\phi')\frac{e^{-j\beta R'}}{R'}d\phi' \tag{5.20}$$

$$A_\theta(r,\theta,\phi) = \frac{\mu a \cos(\theta)}{4\pi}\int_0^{2\pi} I_\rho \cos(\phi-\phi')\frac{e^{-j\beta R'}}{R'}d\phi' \tag{5.21}$$

$$A_\phi(r,\theta,\phi) = -\frac{\mu a}{4\pi}\int_0^{2\pi} I_\rho \sin(\phi-\phi')\frac{e^{-j\beta R'}}{R'}d\phi' \tag{5.22}$$

Direct integration of these expressions seems to be extremely time-consuming. Thus, the problem is approached in a similar way as Werner did in the case of angular current component. It is presumed that the radial current component can also be expressed as a function of the integral given by Eq.**5.12**. Thorough comparison of Eq.**5.12** and Eqs.**5.20-22** leads to the following relations:

$$A_r(r,\theta,\phi) = \frac{\mu\tan(\theta)}{2j\beta r}\frac{d}{d\theta}\Im(r,\theta,\phi) \tag{5.23}$$

$$A_\theta(r,\theta,\phi)=\frac{\mu}{2j\beta r}\frac{d}{d\theta}\Im(r,\theta,\phi) \tag{5.24}$$

$$A_\phi(r,\theta,\phi)=\frac{\mu}{2j\beta r\sin(\theta)}\frac{d}{d\phi}\Im(r,\theta,\phi) \tag{5.25}$$

Finally, introducing series expansion of the integral (see Eq.**5.15**) into above formulae and employing Eqs.**5.3**,**4** expressed in spherical coordinates, the following set of expressions has been derived:

$$H_r(r,\theta,\phi)\equiv 0 \tag{5.26}$$

$$H_\phi(r,\theta,\phi)=\frac{\beta a\beta r\cos(\theta)}{2jR}I_n\cos(n\phi)\sum_{m=1}^{\infty}A_{mn}\frac{(\beta ar\sin\theta/R)^{m-1}}{(m-1)!}$$
$$\times\left(h_{m-2}^{(2)}(\beta R)+\frac{1-2m}{\beta R}h_{m-1}^{(2)}(\beta R)\right) \tag{5.27}$$

$$H_\theta(r,\theta,\phi)=\frac{(\beta a)(\beta r)}{2jR}nI_n\cos(n\phi)\sum_{m=1}^{\infty}A_{mn}\frac{(\beta ar\sin\theta/R)^{m-1}}{m!}$$
$$\times\left(h_{m-2}^{(2)}(\beta R)+\frac{1-2m}{\beta R}h_{m-1}^{(2)}(\beta R)\right) \tag{5.28}$$

$$E_r(r,\theta,\phi)=-\frac{Z_0\beta a^2 r}{2R^2}I_n\cos(n\phi)\sum_{m=1}^{\infty}A_{mn}\frac{(\beta ar\sin\theta/R)^{m-2}}{m!}$$
$$\times\left[m^2-n^2-m(m+1)\sin^2(\theta)\right]\left(\beta h_{m-2}^{(2)}(\beta R)+\frac{1-2m}{R}h_{m-1}^{(2)}(\beta R)\right) \tag{5.29}$$

$$E_\phi(r,\theta,\phi)=-\frac{aZ_0}{2R^2}nI_n\sin(n\phi)\sum_{m=1}^{\infty}A_{mn}\frac{(\beta ar\sin\theta/R)^{m-1}}{m!}$$
$$\times\left\{(\beta r)^2h_{m-3}^{(2)}(\beta R)+(1-2m)\left[(m+1)-\left(\frac{r}{R}\right)^2(1+2m)\right]h_{m-1}^{(2)}(\beta R)\right\} \tag{5.30}$$

$$E_\theta(r,\theta,\phi)=\frac{a\,Z_0\cos(\theta)}{2R^2}I_n\cos(n\phi)\sum_{m=1}^{\infty}A_{mn}\frac{(\beta ar\sin\theta/R)^{m-1}}{(m-1)!}$$

$$\times\left\{(\beta r)^2 h_{m-3}^{(2)}(\beta R)++\beta R\left[(m+1)+2\left(\frac{r}{R}\right)^2(1-2m)\right]h_{m-2}^{(2)}(\beta R)+\right.$$

$$\left.+(1-2m)\left[(m+1)-\left(\frac{r}{R}\right)^2(1+2m)\right]h_{m-1}^{(2)}(\beta R)\right\} \qquad (5.31)$$

Derivation of these expressions was very laborious and they look quite complicated. However, as it will be shown, due to the presence of factorial term *m!* in denominators, computation of the series quickly converges. For relatively small loops (up to about 4 wavelengths), usage of 20 series terms is usually sufficient. For larger loops, the required number of terms may be higher, but does not exceed 100 the for most practical situations.

5.5 Transverse Current Component

Now, let us present the solution for *z*-polarized electric current:

$$I_z(\phi')=\hat{a}_r I_z\cos(\theta)-\hat{a}_\theta I_z\sin(\theta) \qquad (5.32)$$

As previously, the vector potential is expressed as a function of the integral (see Eq.**5.15**):

$$A_r(r,\theta,\phi)=\frac{\mu a}{2j\beta r}\left[\frac{\sin(\theta)}{r}\frac{d}{d\theta}\Im(r,\theta,\phi)-\cos(\theta)\frac{d}{dr}\Im(r,\theta,\phi)\right] \qquad (5.33)$$

$$A_\theta(r,\theta,\phi)=-\frac{\mu a}{2j\beta r}\left[\frac{\sin(\theta)\tan(\theta)}{r}\frac{d}{d\theta}\Im(r,\theta,\phi)-\sin(\theta)\frac{d}{dr}\Im(r,\theta,\phi)\right] \qquad (5.34)$$

$$A_\phi(r,\theta,\phi)\equiv 0 \qquad (5.35)$$

Eventually, it leads to the following expressions for magnetic and electric components at the test point:

$$H_r(r,\theta,\phi)=\frac{(\beta a)^2\sin(\theta)}{2jR}nI_n\sin(n\phi)\sum_{m=1}^{\infty}A_{mn}\frac{(\beta ar\sin\theta/R)^{m-1}}{m!}$$
$$\times\left(h_{m-2}^{(2)}(\beta R)+\frac{1-2m}{\beta R}h_{m-1}^{(2)}(\beta R)\right) \quad (5.36)$$

$$H_\theta(r,\theta,\phi)=\frac{(\beta a)^2\cos(\theta)}{2jR}nI_n\sin(n\phi)\sum_{m=1}^{\infty}A_{mn}\frac{(\beta ar\sin\theta/R)^{m-1}}{m!}$$
$$\times\left(h_{m-2}^{(2)}(\beta R)+\frac{1-2m}{\beta R}h_{m-1}^{(2)}(\beta R)\right) \quad (5.37)$$

$$H_\phi(r,\theta,\phi)=\frac{\beta a^2}{2jR^2}I_n\cos(n\phi)\sum_{m=1}^{\infty}A_{mn}\frac{(\beta ar\sin\theta/R)^{m-1}}{m!}$$
$$\times\left\{(\beta r\sin(\theta))^2h_{m-3}^{(2)}(\beta R)+\beta R\left[m+2\left(\frac{r\sin(\theta)}{R}\right)^2(1-2m)\right]h_{m-2}^{(2)}(\beta R)\right.$$
$$\left.+(1-2m)\left[m-\left(\frac{r\sin(\theta)}{R}\right)^2(1+2m)\right]h_{m-1}^{(2)}(\beta R)\right\} \quad (5.38)$$

$$E_r(r,\theta,\phi)=-\frac{Z_0a^2r\sin(2\theta)}{4R^4}I_n\cos(n\phi)\sum_{m=1}^{\infty}A_{mn}\frac{(\beta ar\sin\theta/R)^{m-1}}{m!}(m+2)$$
$$\times\left\{(\beta R)^2h_{m-3}^{(2)}(\beta R)+2\beta R(1-2m)h_{m-2}^{(2)}(\beta R)-(1-2m)(1+2m)h_{m-1}^{(2)}(\beta R)\right\}$$
$$-\frac{Z_0\beta a^3\cos(\theta)}{2R^3}I_n\cos(n\phi)\sum_{m=2}^{\infty}A_{mn}\frac{(\beta ar\sin\theta/R)^{m-2}}{m!}$$
$$(m^2-n^2)\left[\beta R\,h_{m-2}^{(2)}(\beta R)+(1-2m)h_{m-1}^{(2)}(\beta R)\right] \quad (5.39)$$

$$E_\theta(r,\theta,\phi) = -\frac{a^2 r Z_0}{2R^4} I_n \cos(n\phi)$$

$$\sum_{m=1}^{\infty} A_{mn} \frac{(\beta a r \sin\theta / R)^{m-1}}{m!} \Big\{ -\beta R \left(\beta r \sin(\theta)^2\right) h_{m-4}^{(2)}(\beta R)$$

$$-(\beta R)^2 \left[\sin(\theta)^2 \left(3(1-2m)\left(\frac{r}{R}\right)^2 + (m+2) \right) + m \right] h_{m-3}^{(2)}(\beta R)$$

$$-\beta R (1-2m) \left[\sin(\theta)^2 \left(2(m+2) - 3(1+2m)\left(\frac{r}{R}\right)^2 \right) + 2m \right] h_{m-2}^{(2)}(\beta R)$$

$$+(1-2m)(1+2m) \left[\sin(\theta)^2 \left((m+2) - (2m+3)\left(\frac{r}{R}\right)^2 \right) + m \right] h_{m-1}^{(2)}(\beta R) \Big\}$$

$$-\frac{\beta a^3 Z_0 \sin(\theta)}{2R^3} I_n \cos(n\phi) \sum_{m=2}^{\infty} A_{mn} \frac{(\beta a r \sin\theta / R)^{m-2}}{m!}$$

$$\times \left(n^2 - m^2\right) \left[\beta R h_{m-2}^{(2)}(\beta R) + (1-2m) h_{m-1}^{(2)}(\beta R) \right] \qquad (5.40)$$

$$E_\phi(r,\theta,\phi) = -\frac{a^2 r Z_0 \cos(\theta)}{2R^4} n I_n \sin(n\phi) \sum_{m=1}^{\infty} A_{mn} \frac{(\beta a r \sin\theta / R)^{m-1}}{m!}$$

$$\left\{ (\beta R)^2 h_{m-3}^{(2)}(\beta R) + 2(1-2m)(\beta R) h_{m-2}^{(2)}(\beta R) \right.$$

$$\left. -(1-2m)(1+2m) h_{m-1}^{(2)}(\beta R) \right\} \qquad (5.41)$$

The above expressions are relatively complex but, as will be shown in the forthcoming example, they require much less computational effort than the direct integration procedure. Besides, let us note that although several Hankel functions appear in all the above expressions, they have the same argument, so the Hankel functions of different order may be effectively calculated using recursive algorithm.

5.6 Benchmark Tests

Three types of independent tests will be run to investigate the accuracy and convergence rate of Eqs.**5.26-31**,**36-41**. These tests can be grouped into the following categories:

1. convergence as a function of series terms (m = 1,2,…,M);
2. available speedup when compared to the direct integration procedure;
3. asymptotic convergence to the NTF transformation.

Formulae for the contribution of $I_\rho(\phi')$ and $I_z(\phi')$ to 6 EM components at the test point have been derived. All twelve formulae were thoroughly tested against direct numerical integration and in all cases convergence has been obtained. For the purpose of this Section, the focus is on the $I_z(\phi')$ contribution to the H_ϕ component (see Eq.**5.38**), as a representative case.

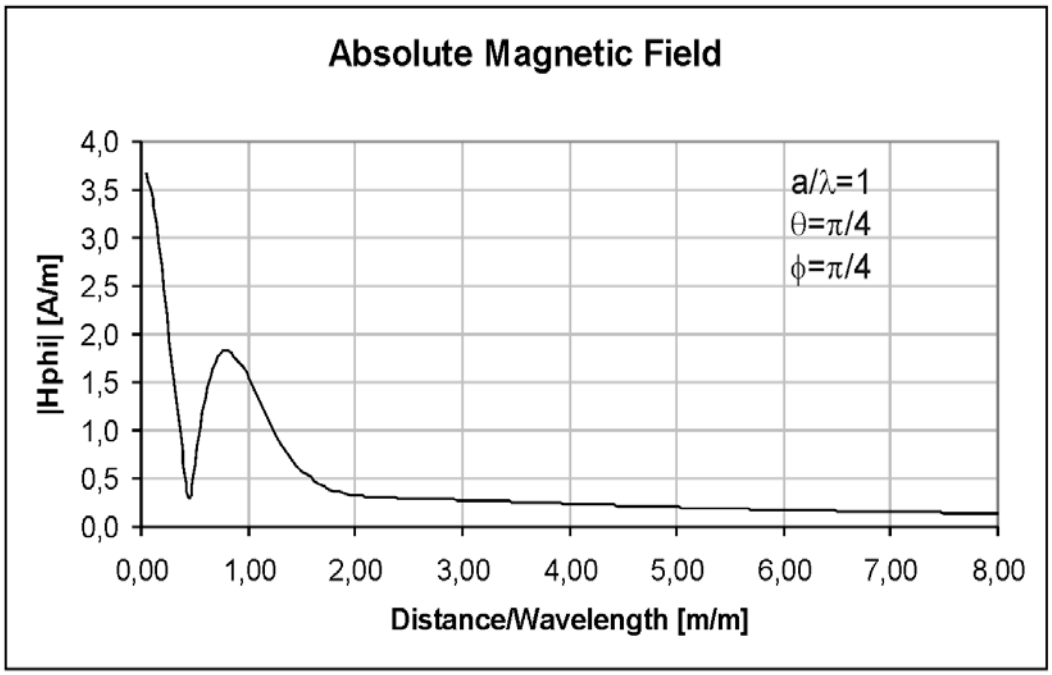

Fig.5.3. Magnitude of magnetic field $|H_\phi|$ as a function of relative distance *r* from the loop center (see Eq.5.38).

Fig.5.3 presents $I_z(\phi')$ contribution to H_ϕ component, computed using Eq.**5.38**, assuming the loop radius equals to the wavelength (a = λ). The results are drawn as a function of distance *r* from the loop center, assuming that the test point is seen at the angles θ=π/4 and ϕ=π/4. Next, computation with different number of summation terms *M* has been run, and the obtained results have been compared with the ones obtained using direct integration in 3D space, with

very high accuracy of 10^{-12}. Convergence tests have been performed on 160 samples taken from the curve of Fig.5.3 (with r varying from 0.05λ to 8λ). Fig.5.4 presents a histogram depicting how many of these 160 samples match a particular accuracy value. It can be seen that for M=15, most of the samples have an average error of about 0.02%. Furthermore, increasing M to 25 causes the average error drop to about 0.01%. It proves a quick convergence rate of the series computation, mainly due to the factorial $m!$ in denominator.

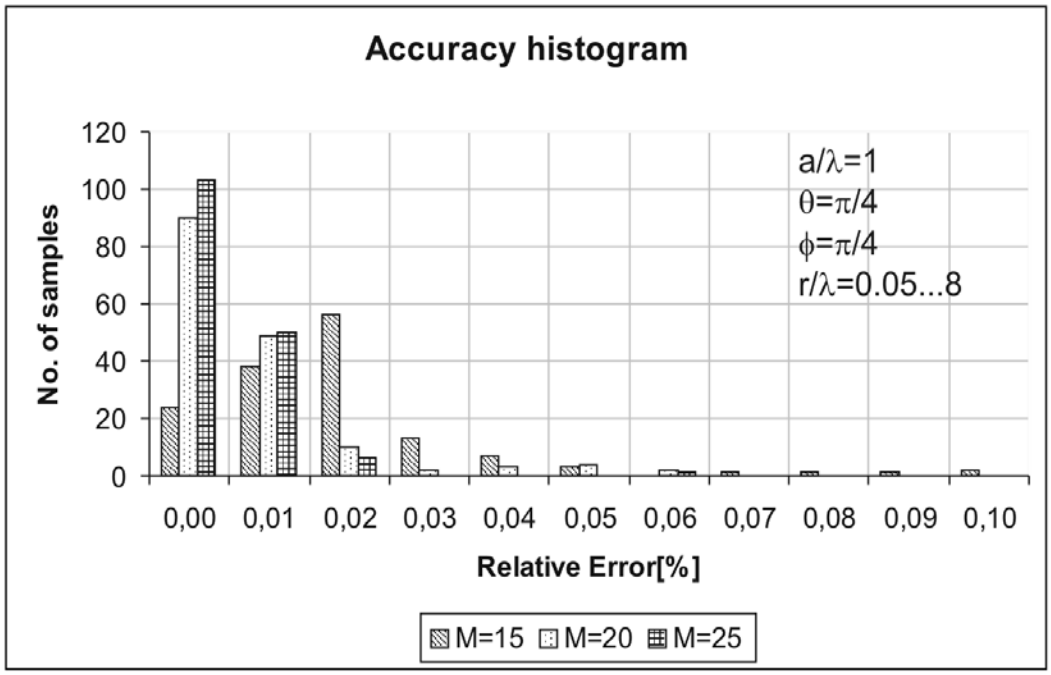

Fig.5.4. Accuracy histogram for points shown in Fig.5.3 for consecutive number of terms M in Eq.5.38.

Now let us move on to the speedup issue. The computing time of the above approach will be compared with the computing time of direct integration procedure, providing that the accuracy of both approaches is similar. This time, the investigation of all EM field components is presented. As a reference, direct integration results obtained with very high accuracy of 10^{-12} are used. Each of the compared algorithms had been running until the particular accuracy (1%, 0.1%) was reached, with respect to the reference. The computing time was compared for each of the considered 160 samples. Table 5.1 presents the average speedup factors, understood as the ratio of the computing time of direct integration procedure and the computing time of the introduced method. The results are shown separately for each of the EM field components. Additionally, since each of the components was calculated for 160 points, the average value and its standard deviation σ have been depicted. At least two

interesting observations can be made. First of all, if the accuracy needs to be enhanced, the computational effort rises slower in the presented method than for the direct integration one. It can be seen in the fourth column of the Table 5.1, where speedups corresponding to 0.1% accuracy are higher by about 10 to 20% as compared to the values depicted in the third column, corresponding to 1.0% accuracy. Second observation is that in most cases the speedups are significantly higher for electric field components. The source of the difference lies in a procedure of electric and magnetic components computation based on direct numerical integration. According to Eqs.**5.6-11**, each electric field component is computed from previously obtained two magnetic field components, imposing at least twice longer computational time of electric field components.

Table 5.1. Speedup factor for all of EM field components obtained from the contribution of $I_z(\phi')$ and $I_\rho(\phi')$.

Current comp.	EM comp.	Avg. speedup factor		Std. deviation of the speedup factor	
		Accuracy			
		1,0[%]	0,1[%]	1,0[%]	0,1[%]
$I_z(\phi')$	H_ϕ [A/m]	45	52	8	8
	H_θ [A/m]	31	38	5	7
	H_r [A/m]	31	39	5	7
	E_ϕ [V/m]	37	45	6	8
	E_θ [V/m]	80	92	19	17
	E_r [V/m]	102	121	15	14
$I_\rho(\phi')$	H_ϕ [A/m]	26	29	3	4
	H_θ [A/m]	30	36	5	7
	E_ϕ [V/m]	60	84	10	20
	E_θ [V/m]	52	60	7	10
	E_r [V/m]	86	114	17	15

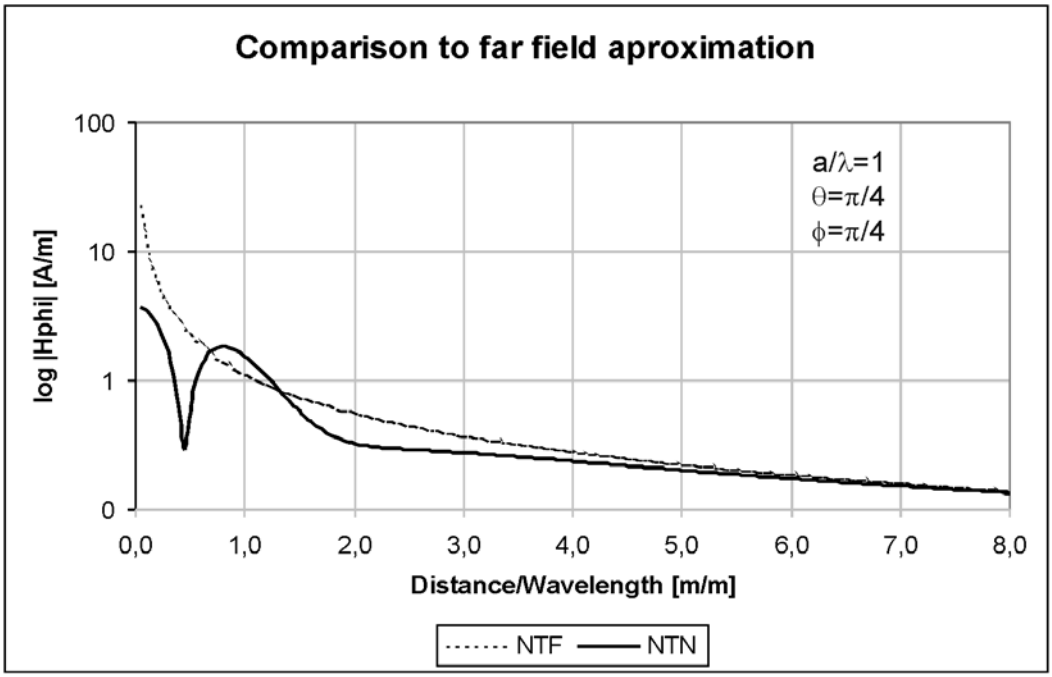

Fig.5.5. Comparison between Eq.5.38 and corresponding NTF solution.

The last investigation focuses on the asymptotic convergence of the NTN solution to the NTF one [**80**]. Fig.5.5 shows both curves in a logarithmic scale. It is clearly observable that the NTN transformation tends to the NTF one, and for the distance larger than about 6-7 wavelengths discrepancy is barely visible, which indicates that it is the far field zone limit.

5.7 Summary

Analytically preprocessed formulae for the effective near-to-near transformation of axisymmetrical problems have been presented. The obtained results show that a speedup by a factor of about 30 to 100 can be obtained, with respect to direct integration in 3-D space in practical cases of Huygens surfaces of the size of a few wavelengths. These results appear to be very attractive when practical applications are concerned. Thus, the third auxiliary thesis posed in Chapter 1 has been successfully proven.

Chapter 6

Conclusions and perspectives

This dissertation has been focused on extension of the finite-difference time-domain method and its computational capabilities, by supplementing the method with analytical formulations appropriate for specific electromagnetic problems. Three types of the problems have been considered in this thesis:

1. 1D, 2D, and 3D periodic structures;
2. far-field optical microscope imaging;
3. near-to-near electromagnetic field transformation in axisymmetrical structures.

The first issue is an extension of methods and algorithms already known from the literature. Considerations of the author of this thesis have been focused on CL-FDTD algorithm. Implementation of the algorithm has been extended from 1D to 2D and 3D periodicity, and successful validation has been performed. The method has been further applied to the analysis of eigenvalues problems in the infinitely periodic structures. It has been proved to be a useful technique for investigation of dispersive properties of photonic crystals. Afterwards, an extension of the CL-FDTD algorithm to the analysis of plane wave diffraction from infinitely periodic structure has been shown. For that purpose, three computational models have been proposed and thoroughly validated against other numerical methods, such as Finite Element Method, Plane Wave Expansion, Rigorous Coupled Wave Analysis, and analytical formulations. It has also been shown that approximate approach with an infinite plane wave over periodic structure is convergent to the real case with a finite spot of a Gaussian shape.

With growing interest in photonic crystals from optics, through millimeter wave technology, to microwaves, the scope of potential applications of the computational methods like CL-FDTD will be extending. However, it seems that more challenging will be another issue addressed in the context of periodic structures, i.e. scatterometry. First of all, single frequency operation in CL-FDTD models for a plane wave illumination of periodic structures is their major limitation. Additionally, it would be an interesting option to develop a source with an

arbitrary shape of a beam impinging on infinite periodic structure. As it has been pointed out in Chapter 3, some preliminary studies have already been published.

The second type of problems addressed in this dissertation deals with electromagnetic modeling of the far-field optical microscopes that utilize lenses as image-processing devices. A theoretical knowledge about an image formation in lens microscopes is very well established and thoroughly examined. However, imaging tools are still under development, driven by the science and industry's demand for still increasing resolution. It forces the modeling methods to improve their computational capabilities, as well as the achievable accuracy. This is a proper place for full-wave electromagnetic design, especially at the target level where subwavelength diffraction plays an important role. It has been proposed in this dissertation to couple the full-wave finite-difference time-domain technique with the optical method based on Fresnel approximation of the diffraction phenomenon. Such approach combines advantages of both methods, increasing the achieavable accuracy without a tremendous impact on the computation time. It has been proven to be useful in the modeling of wide field, as well as confocal optical microscopes.

There is a lot of perspectives for the finite-difference time-domain method, as well as for the other full-wave approaches to find new fields of application in the optical imaging. With growing capabilities of computing machines, it will be possible to extend the complexity of FDTD models and their computational volume. Another important issue that has already found some attention of researchers is the modeling of sources which properly represent time-dependent electromagnetic field distribution focused by a lens without loss of causality. Successful research in this field will help to improve appropriate represenation of electromagnetic field in the finite-difference time-domain schemes.

The last but definitely not least subject addressed in this thesis is strictly related to the modeling of axisymmetrical antennae. An efficient method for electromagnetic field transformations in a near zone of a radiating axisymmetrical object has been derived and validated with theoretical calculations. The method can be useful for the modeling of the axisymmetrical antenna systems with no common symmetry axis, like in the case of Cassegrain antenna with a feeding antenna shifted off the axis.

The method presented in this thesis waits for its implementation in the finite-difference time-domain scheme or other computational methods applied to axisymmetrical problems.

To summarize the whole dissertation, thesis posed in Chapter 1, claiming that the partially analytical FDTD method can improve computational efficiency of the overall method has been proven. The auxiliary statements regarding periodic structures, microscope imaging, and near-to-near field transformation for axisymmetrical problems have also been thoroughly investigated and confirmed.

Appendix 1

Periodic Boundary Conditions

A schematic flow of the FDTD algorithm for periodic boundary conditions is given below. Notation is based on C language.

```
for (FDTD_iteration==1; FDTD_iteration>0; FDTD_iteration++){
  //E calculation with FDTD algorithm
  ...
    switch (periodicity){
      case x:
        Ey_re(N-1,:,:) = Ey_re(1,:,:)*cos(ψx) - Ey_im(1,:,:)*sin(ψx);
        Ey_im(N-1,:,:) = Ey_im(1,:,:)*cos(ψx) + Ey_re(1,:,:)*sin(ψx);
        Ez_re(N-1,:,:) = Ez_re(1,:,:)*cos(ψx) - Ez_im(1,:,:)*sin(ψx);
        Ez_im(N-1,:,:) = Ez_im(1,:,:)*cos(ψx) + Ez_re(1,:,:)*sin(ψx);
        break;
      case y:
        Ex_re(:,M-1,:) = Ex_re(:,1,:)*cos(ψy) - Ex_im(:,1,:)*sin(ψy);
        Ex_im(:,M-1,:) = Ex_im(:,1,:)*cos(ψy) + Ex_re(:,1,:)*sin(ψy);
        Ez_re(:,M-1,:) = Ez_re(:,1,:)*cos(ψy) - Ez_im(:,1,:)*sin(ψy);
        Ez_im(:,M-1,:) = Ez_im(:,1,:)*cos(ψy) + Ez_re(:,1,:)*sin(ψy);
        break;
      case z:
        Ex_re(:,:,P-1) = Ex_re(:,:,1)*cos(ψz) - Ex_im(:,:,1)*sin(ψz);
        Ex_im(:,:,P-1) = Ex_im(;,:,1)*cos(ψz) + Ex_re(:,:,1)*sin(ψz);
        Ey_re(:,:,P-1) = Ey_re(:,:,1)*cos(ψz) - Ey_im(:,:,1)*sin(ψz);
        Ey_im(:,:,P-1) = Ey_im(;,:,1)*cos(ψz) + Ey_re(:,:,1)*sin(ψz);
        break;
      case xy:
        Ey_re(N-1,:,:) = Ey_re(1,:,:)*cos(ψx) - Ey_im(1,:,:)*sin(ψx);
```

Ey_im(N-1,:,:) = Ey_im(1,:,:)*cos(ψ_x) + Ey_re(1,:,:)*sin(ψ_x);

Ez_re(N-1,:,:) = Ez_re(1,:,:)*cos(ψ_x) - Ez_im(1,:,:)*sin(ψ_x);

Ez_im(N-1,:,:) = Ez_im(1,:,:)*cos(ψ_x) + Ez_re(1,:,:)*sin(ψ_x);

Ex_re(:,M-1,:) = Ex_re(:,1,:)*cos(ψ_y) - Ex_im(:,1,:)*sin(ψ_y);

Ex_im(:,M-1,:) = Ex_im(:,1,:)*cos(ψ_y) + Ex_re(:,1,:)*sin(ψ_y);

Ez_re(:,M-1,:) = Ez_re(:,1,:)*cos(ψ_y) - Ez_im(:,1,:)*sin(ψ_y);

Ez_im(:,M-1,:) = Ez_im(:,1,:)*cos(ψ_y) + Ez_re(:,1,:)*sin(ψ_y);

break;

case xz:

Ey_re(N-1,:,:) = Ey_re(1,:,:)*cos(ψ_x) - Ey_im(1,:,:)*sin(ψ_x);

Ey_im(N-1,:,:) = Ey_im(1,:,:)*cos(ψ_x) + Ey_re(1,:,:)*sin(ψ_x);

Ez_re(N-1,:,:) = Ez_re(1,:,:)*cos(ψ_x) - Ez_im(1,:,:)*sin(ψ_x);

Ez_im(N-1,:,:) = Ez_im(1,:,:)*cos(ψ_x) + Ez_re(1,:,:)*sin(ψ_x);

Ex_re(:,:,P-1) = Ex_re(:,:,1)*cos(ψ_z) - Ex_im(:,:,1)*sin(ψ_z);

Ex_im(:,:,P-1) = Ex_im(;,:,1)*cos(ψ_z) + Ex_re(:,:,1)*sin(ψ_z);

Ey_re(:,:,P-1) = Ey_re(:,:,1)*cos(ψ_z) - Ey_im(:,:,1)*sin(ψ_z);

Ey_im(:,:,P-1) = Ey_im(;,:,1)*cos(ψ_z) + Ey_re(:,:,1)*sin(ψ_z);

break;

case yz:

Ex_re(:,M-1,:) = Ex_re(:,1,:)*cos(ψ_y) - Ex_im(:,1,:)*sin(ψ_y);

Ex_im(:,M-1,:) = Ex_im(:,1,:)*cos(ψ_y) + Ex_re(:,1,:)*sin(ψ_y);

Ez_re(:,M-1,:) = Ez_re(:,1,:)*cos(ψ_y) - Ez_im(:,1,:)*sin(ψ_y);

Ez_im(:,M-1,:) = Ez_im(:,1,:)*cos(ψ_y) + Ez_re(:,1,:)*sin(ψ_y);

Ex_re(:,:,P-1) = Ex_re(:,:,1)*cos(ψ_z) - Ex_im(:,:,1)*sin(ψ_z);

Ex_im(:,:,P-1) = Ex_im(;,:,1)*cos(ψ_z) + Ex_re(:,:,1)*sin(ψ_z);

Ey_re(:,:,P-1) = Ey_re(:,:,1)*cos(ψ_z) - Ey_im(:,:,1)*sin(ψ_z);

Ey_im(:,:,P-1) = Ey_im(;,:,1)*cos(ψ_z) + Ey_re(:,:,1)*sin(ψ_z);

break;

case xyz:

Ey_re(N-1,:,:) = Ey_re(1,:,:)*cos(ψ_x) - Ey_im(1,:,:)*sin(ψ_x);

Ey_im(N-1,:,:) = Ey_im(1,:,:)*cos(ψ_x) + Ey_re(1,:,:)*sin(ψ_x);

Ez_re(N-1,:,:) = Ez_re(1,:,:)*cos(ψ_x) - Ez_im(1,:,:)*sin(ψ_x);

```
      Ez_im(N-1,:,:) = Ez_im(1,:,:)*cos(ψx) + Ez_re(1,:,:)*sin(ψx);
      Ex_re(:,M-1,:) = Ex_re(:,1,:)*cos(ψy) - Ex_im(:,1,:)*sin(ψy);
      Ex_im(:,M-1,:) = Ex_im(:,1,:)*cos(ψy) + Ex_re(:,1,:)*sin(ψy);
      Ez_re(:,M-1,:) = Ez_re(:,1,:)*cos(ψy) - Ez_im(:,1,:)*sin(ψy);
      Ez_im(:,M-1,:) = Ez_im(:,1,:)*cos(ψy) + Ez_re(:,1,:)*sin(ψy);
      Ex_re(:,:,P-1) = Ex_re(:,:,1)*cos(ψz) - Ex_im(:,:,1)*sin(ψz);
      Ex_im(:,:,P-1) = Ex_im(;,:,1)*cos(ψz) + Ex_re(:,:,1)*sin(ψz);
      Ey_re(:,:,P-1) = Ey_re(:,:,1)*cos(ψz) - Ey_im(:,:,1)*sin(ψz);
      Ey_im(:,:,P-1) = Ey_im(;,:,1)*cos(ψz) + Ey_re(:,:,1)*sin(ψz);
      break;
   }
   dt += dt/2;
//H calculation with FDTD algorithm
...
   switch (periodicity){
     case x:
       Hy_re(1,:,:) = Hy_re(N-1,:,:)*cos(ψx) + Hy_im(N-1,:,:)*sin(ψx);
       Hy_im(1,:,:) = Hy_im(N-1,:,:)*cos(ψx) - Hy_re(N-1,:,:)*sin(ψx);
       Hz_re(1,:,:) = Hz_re(N-1,:,:)*cos(ψx) + Hz_im(N-1,:,:)*sin(ψx);
       Hz_im(1,:,:) = Hz_im(N-1,:,:)*cos(ψx) - Hz_re(N-1,:,:)*sin(ψx);
       break;
     case y:
       Hx_re(:,1,:) = Hx_re(:,M-1,:)*cos(ψy) + Hx_im(:,M-1,:)*sin(ψy);
       Hx_im(:,1,:) = Hx_im(:,M-1,:)*cos(ψy) - Hx_re(:,M-1,:)*sin(ψy);
       Hz_re(:,1,:) = Hz_re(:,M-1,:)*cos(ψy) + Hz_im(:,M-1,:)*sin(ψy);
       Hz_im(:,1,:) = Hz_im(:,M-1,:)*cos(ψy) - Hz_re(:,M-1,:)*sin(ψy);
       break;
     case z:
       Hx_re(:,:,1) = Hx_re(:,:,P-1)*cos(ψz) + Hx_im(:,:,P-1)*sin(ψz);
       Hx_im(:,:,1) = Hx_im(:,:,P-1)*cos(ψz) - Hx_re(:,:,P-1)*sin(ψz);
       Hy_re(:,:,1) = Hy_re(:,:,P-1)*cos(ψz) + Hy_im(:,:,P-1)*sin(ψz);
       Hy_im(:,:,1) = Hy_im(:,:,P-1)*cos(ψz) - Hy_re(:,:,P-1)*sin(ψz);
```

break;

case xy:

Hy_re(1,:,:) = Hy_re(N-1,:,:)*cos(ψ_x) + Hy_im(N-1,:,:)*sin(ψ_x);

Hy_im(1,:,:) = Hy_im(N-1,:,:)*cos(ψ_x) - Hy_re(N-1,:,:)*sin(ψ_x);

Hz_re(1,:,:) = Hz_re(N-1,:,:)*cos(ψ_x) + Hz_im(N-1,:,:)*sin(ψ_x);

Hz_im(1,:,:) = Hz_im(N-1,:,:)*cos(ψ_x) - Hz_re(N-1,:,:)*sin(ψ_x);

Hx_re(:,1,:) = Hx_re(:,M-1,:)*cos(ψ_y) + Hx_im(:,M-1,:)*sin(ψ_y);

Hx_im(:,1,:) = Hx_im(:,M-1,:)*cos(ψ_y) - Hx_re(:,M-1,:)*sin(ψ_y);

Hz_re(:,1,:) = Hz_re(:,M-1,:)*cos(ψ_y) + Hz_im(:,M-1,:)*sin(ψ_y);

Hz_im(:,1,:) = Hz_im(:,M-1,:)*cos(ψ_y) - Hz_re(:,M-1,:)*sin(ψ_y);

break;

case xz:

Hy_re(1,:,:) = Hy_re(N-1,:,:)*cos(ψ_x) + Hy_im(N-1,:,:)*sin(ψ_x);

Hy_im(1,:,:) = Hy_im(N-1,:,:)*cos(ψ_x) - Hy_re(N-1,:,:)*sin(ψ_x);

Hz_re(1,:,:) = Hz_re(N-1,:,:)*cos(ψ_x) + Hz_im(N-1,:,:)*sin(ψ_x);

Hz_im(1,:,:) = Hz_im(N-1,:,:)*cos(ψ_x) - Hz_re(N-1,:,:)*sin(ψ_x);

Hx_re(:,:,1) = Hx_re(:,:,P-1)*cos(ψ_z) + Hx_im(:,:,P-1)*sin(ψ_z);

Hx_im(:,:,1) = Hx_im(:,:,P-1)*cos(ψ_z) - Hx_re(:,:,P-1)*sin(ψ_z);

Hy_re(:,:,1) = Hy_re(:,:,P-1)*cos(ψ_z) + Hy_im(:,:,P-1)*sin(ψ_z);

Hy_im(:,:,1) = Hy_im(:,:,P-1)*cos(ψ_z) - Hy_re(:,:,P-1)*sin(ψ_z);

break;

case yz:

Hx_re(:,1,:) = Hx_re(:,M-1,:)*cos(ψ_y) + Hx_im(:,M-1,:)*sin(ψ_y);

Hx_im(:,1,:) = Hx_im(:,M-1,:)*cos(ψ_y) - Hx_re(:,M-1,:)*sin(ψ_y);

Hz_re(:,1,:) = Hz_re(:,M-1,:)*cos(ψ_y) + Hz_im(:,M-1,:)*sin(ψ_y);

Hz_im(:,1,:) = Hz_im(:,M-1,:)*cos(ψ_y) - Hz_re(:,M-1,:)*sin(ψ_y);

Hx_re(:,:,1) = Hx_re(:,:,P-1)*cos(ψ_z) + Hx_im(:,:,P-1)*sin(ψ_z);

Hx_im(:,:,1) = Hx_im(:,:,P-1)*cos(ψ_z) - Hx_re(:,:,P-1)*sin(ψ_z);

Hy_re(:,:,1) = Hy_re(:,:,P-1)*cos(ψ_z) + Hy_im(:,:,P-1)*sin(ψ_z);

Hy_im(:,:,1) = Hy_im(:,:,P-1)*cos(ψ_z) - Hy_re(:,:,P-1)*sin(ψ_z);

break;

case xyz:

```
        Hy_re(1,:,:) = Hy_re(N-1,:,:)*cos(ψx) + Hy_im(N-1,:,:)*sin(ψx);
        Hy_im(1,:,:) = Hy_im(N-1,:,:)*cos(ψx) - Hy_re(N-1,:,:)*sin(ψx);
        Hz_re(1,:,:) = Hz_re(N-1,:,:)*cos(ψx) + Hz_im(N-1,:,:)*sin(ψx);
        Hz_im(1,:,:) = Hz_im(N-1,:,:)*cos(ψx) - Hz_re(N-1,:,:)*sin(ψx);
        Hx_re(:,1,:) = Hx_re(:,M-1,:)*cos(ψy) + Hx_im(:,M-1,:)*sin(ψy);
        Hx_im(:,1,:) = Hx_im(:,M-1,:)*cos(ψy) - Hx_re(:,M-1,:)*sin(ψy);
        Hz_re(:,1,:) = Hz_re(:,M-1,:)*cos(ψy) + Hz_im(:,M-1,:)*sin(ψy);
        Hz_im(:,1,:) = Hz_im(:,M-1,:)*cos(ψy) - Hz_re(:,M-1,:)*sin(ψy);
        Hx_re(:,:,1) = Hx_re(:,:,P-1)*cos(ψz) + Hx_im(:,:,P-1)*sin(ψz);
        Hx_im(:,:,1) = Hx_im(:,:,P-1)*cos(ψz) - Hx_re(:,:,P-1)*sin(ψz);
        Hy_re(:,:,1) = Hy_re(:,:,P-1)*cos(ψz) + Hy_im(:,:,P-1)*sin(ψz);
        Hy_im(:,:,1) = Hy_im(:,:,P-1)*cos(ψz) - Hy_re(:,:,P-1)*sin(ψz);
        break;
    }
}
```

Legend:

1) Indices of all components are written using E(m,n,p) notation, where (m,n,p) indicates the location of the component on the FDTD grid expanded in a Cartesian (x,y,z) space.
2) The maximum number of FDTD grid points is (N,M,P).
3) Suffixes _re and _im denote real and imaginary parts of EM component, respectively,.
4) The symbol ψ denotes the Floquet phase shift per period - a parameter of the CL-FDTD algorithm.
5) A symbol *dt* is the FDTD algorithm's time step.

Appendix 2

Brillouin zone

According to the Bloch's (or Floquet's) theorem, propagation of the electromagnetic wave in a periodic medium can be characterized in the following way:

$$\psi_k(\vec{r}) = u_k(\vec{r})\, e^{j k_0 r} \tag{1.1}$$

where $u_k(r)$ function has the same periodicity $\boldsymbol{L}$ as the periodic medium:

$$u_k\left(\vec{r} + \vec{L}\right) = u_k(\vec{r}) \tag{1.2}$$

and k_0 is the wavenumber.

It implies that the solution of $\psi_k(r)$ function is identical for all the integer multiples of the wavenumber:

$$k_n = k_0 + n\frac{2\pi}{L} \tag{1.3}$$

Thus, mode frequencies are also periodic in the wave vector space, so the analysis of the $k(\omega)$ dispersion can be limited to the region: $-\pi/L < k_n < \pi/L$, usually called the *first Brillouin zone* that characterizes primitive cell of the considered reciprocal lattice. Unique characterization of the dispersion characteristic $k(\omega)$ can be done considering only the so-called *irreducible Brillouin zone*, understood as the first Brillouin zone reduced by using all the possible symmetries. Brillouin zone is parameterized using critical points that refer to the characteristic points of the Brillouin zone.

Let us recall the most common lattice geometries addressed in this thesis:

1. **square lattice**

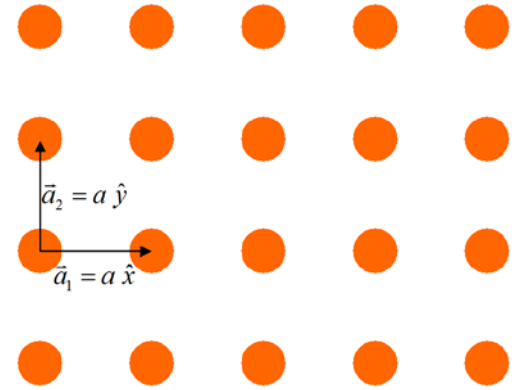

(a)

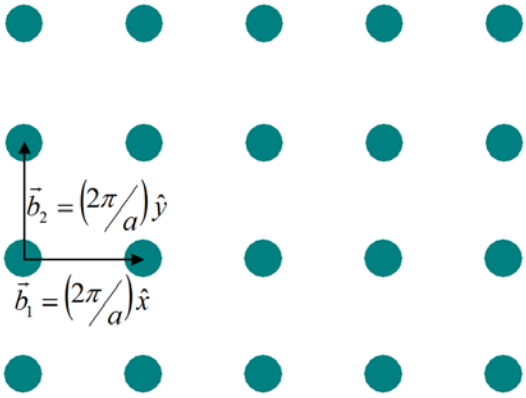

(b)

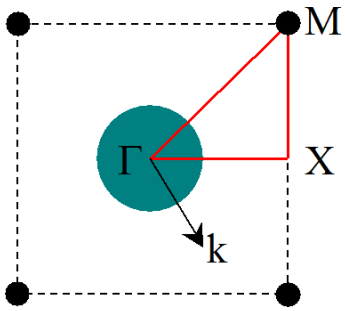

(c)

Fig.A2.1. Square lattice (a) and the corresponding reciprocal lattice (b) with the irreducible Brillouin zone (c).

Critical points:

Γ: $k_x = k_y = 0$.

X: $k_x = 2\pi/a$; $k_y = 0$.

M: $k_x = k_y = 2\pi/a$.

2. hexagonal lattice

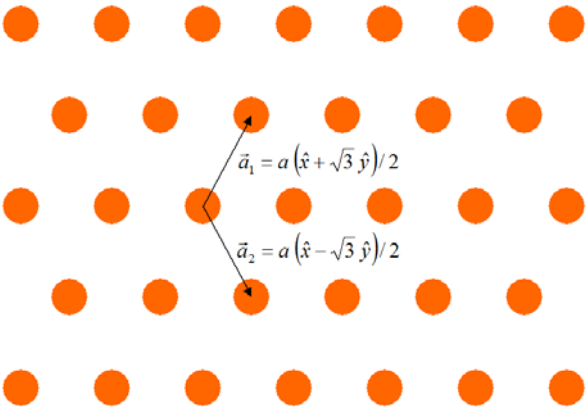

(a)

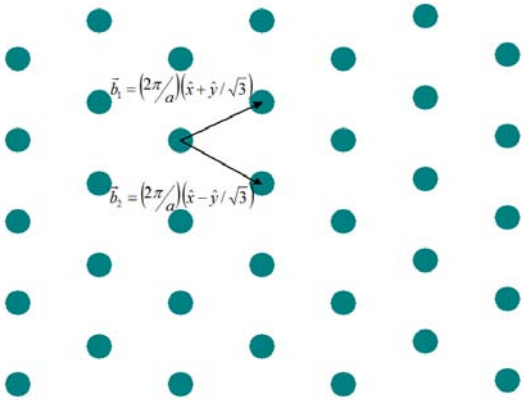

(b)

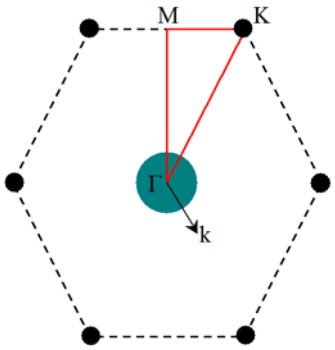

Fig.A2.2. Hexagonal lattice (a) and the corresponding reciprocal lattice (b) with the irreducible Brillouin zone (c).

Critical points:

Γ: $k_x = k_y = 0$.

M: $k_x = 0$; $k_y = 2\pi/\sqrt{3}a$.

K: $k_x = 2\pi/3a$; $k_y = 2\pi/\sqrt{3}a$.

3. Body centered cubic (bcc) lattice

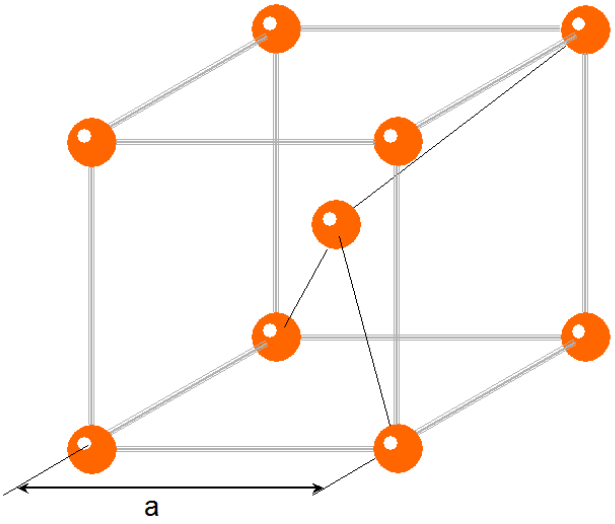

(a)

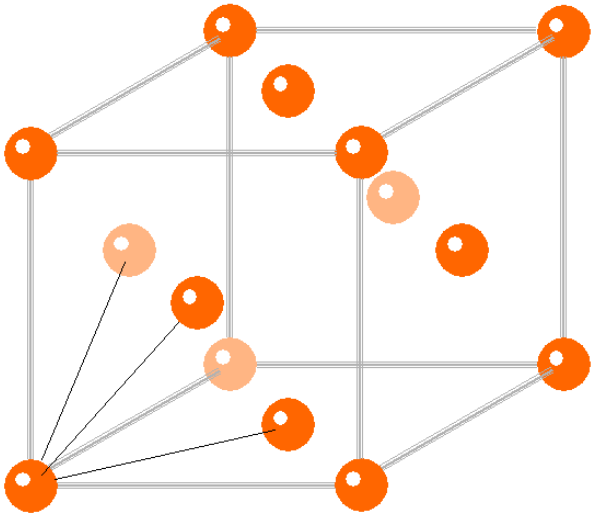

(b)

Fig.A2.3. Body centered cubic lattice (a) and the corresponding reciprocal face centered (fcc) lattice (b).

Critical points:

Γ: $k_x = k_y = k_z = 0$.

H: $k_x = 0$; $k_y = 2\pi/a$; $k_z = 0$.

N: $k_x = \pi/a$; $k_y = \pi/a$; $k_z = 0$.

P: $k_x = \pi/a$; $k_y = \pi/a$; $k_z = \pi/a$.

Appendix 3

Spherical coordinate system

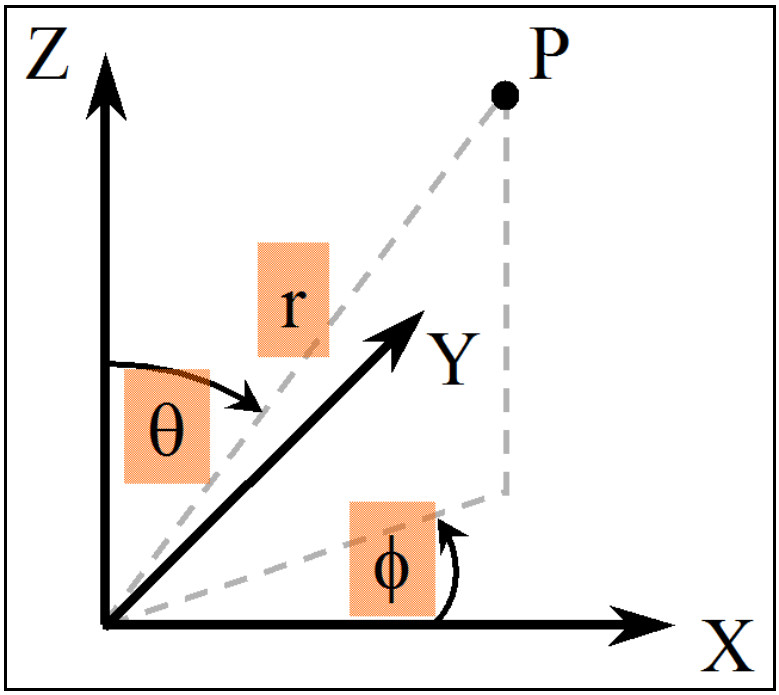

Fig.A3.1. Spherical coordinate system view.

Relation between rectangular and spherical coordinates:

$$x = r\,\sin(\theta)\cos(\phi) \tag{3.1}$$

$$y = r\,\sin(\theta)\sin(\phi) \tag{3.2}$$

$$z = r\,\cos(\theta) \tag{3.3}$$

Transition from rectangular to spherical components:

$$A_r = A_x\,\sin(\theta)\cos(\phi) + A_y\,\sin(\theta)\sin(\phi) + A_z\,\cos(\theta) \tag{3.4}$$

$$A_\theta = A_x\,\cos(\theta)\cos(\phi) + A_y\,\cos(\theta)\sin(\phi) + A_z\,\sin(\theta) \tag{3.5}$$

$$A_\phi = -A_x\,\sin(\phi) + A_y\,\cos(\varphi) \tag{3.6}$$

Transition from spherical to rectangular components:

$$A_x = A_r \sin(\theta)\cos(\phi) + A_\theta \cos(\theta)\cos(\phi) - A_\phi \sin(\phi) \quad (3.7)$$

$$A_y = A_r \sin(\theta)\sin(\phi) + A_\theta \cos(\theta)\sin(\phi) + A_\phi \cos(\phi) \quad (3.8)$$

$$A_z = A_r \cos(\theta) - A_\theta \sin(\theta) \quad (3.9)$$

Appendix 4

Cylindrical coordinate system

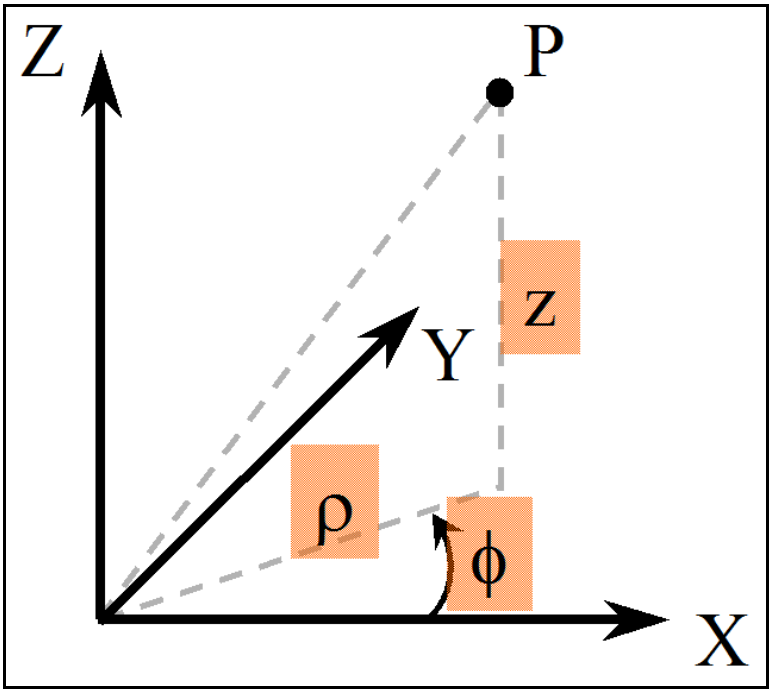

Fig.A4.1. Cylindrical coordinate system view.

Relation between rectangular and cylindrical coordinates:

$$x = \rho \cos(\phi) \tag{4.1}$$

$$y = \rho \sin(\phi) \tag{4.2}$$

$$z = z \tag{4.3}$$

Transition from rectangular to cylindrical components:

$$A_\rho = A_x \cos(\phi) + A_y \sin(\phi) \tag{4.4}$$

$$A_\phi = -A_x \sin(\phi) + A_y \cos(\phi) \tag{4.5}$$

$$A_z = A_z \tag{4.6}$$

Transition from cylindrical to rectangular components:

$$A_x = A_\rho \cos(\phi) - A_\phi \sin(\phi) \tag{4.7}$$

$$A_y = A_\rho \sin(\phi) + A_\phi \cos(\phi) \tag{4.8}$$

$$A_z = A_z \tag{4.9}$$

Appendix 5

Lens imaging algorithm

Below, the procedures for lens imaging based on the Fresnel approximation are given. The code of those scripts was written by the author of this thesis in Matlab environment.

```
function Eo = lens_imaging(fname,frequency,start_angle,stop_angle,ref_angle,ds,di,f)
% Eo = lens_imaging(fname,frequency,start_angle,stop_angle,ref_angle,ds,di,f)
% calculates an image processed by a single cylindrical lens
% upon angular scatterring pattern provided by the user in (fname) file.
%
% Input data should consist of three columns with an angle (degrees),
% and corresponding electric field intensity magnitude and phase (degrees).
%
% frequency - operating frequency, GHz
% start_angle -
% stop_angle - these two values define numerical aperture of a considered
%              beam taken from the file, degrees
% ref_angle - reference angle, degrees
% ds - distance from object plane to the lens, mm
% di - distance from the lens to image plane, mm
% f - focal length of the lens, mm

format long g
deg2rad = pi/180;
rad2deg = 180/pi;

%read data from file
A = load(fname);
%wavenumber
```

```
k = 2*pi*frequency/299.792458; %[1/mm]

ys=0; %[mm] - radiation from the focal point
dang=0.00001;% angular resolution
start_angle_ind = find((A(:,1)>=(start_angle-dang))&(A(:,1)<=(start_angle+dang)));
stop_angle_ind = find((A(:,1)>=(stop_angle-dang))&(da3_data(:,1)<=(stop_angle+dang)));

%electric field at source plane
Es=A(start_angle_ind:stop_angle_ind,2) .*
exp(j*deg2rad.*A(start_angle_ind:stop_angle_ind,4));
%find maximum angle...
alfa_max=A(stop_angle_ind)-ref_angle;%[deg]
%calculate numerical aperture
NA = sin(deg2rad*alfa_max);
%calculate spatial range at the lens
ys_max = tan(deg2rad*alfa_max)*ds;%[mm]

% space vector discretization for a given resolution...
pow=10;
N=2^pow;
dys_min = pi*ds/(k*ys_max);
dys = (2*ys_max/(N-1));%[mm]
while dys>=dys_min
   pow=pow+1;
   N=2^pow;
   dys = (2*ys_max/(N-1));%[mm]
end
ys=-ys_max:dys:ys_max;
fy = -(N-1)/(2*N*dys):1/(N*dys):(N-1)/(2*N*dys);

% interpolation of electric field at newly discretized spatial vector
alfa_p=rad2deg.*atan(ys./ds);
Es_abs=interp1(da3_data(start_angle_ind:stop_angle_ind,1)-
ref_angle,abs(Es),alfa_p,'linear');
```

```
Es_angle=interp1(da3_data(start_angle_ind:stop_angle_ind,1)-
ref_angle,angle(Es),alfa_p,'linear');
Us_FT = Es_abs.*exp(j.*Es_angle);

%impulse response of space between source and lens planes
hfr = h_fr_air(k,ds,ys);
HFR = (1/N)*fft(hfr);
HFR = fftshift(HFR);
% lens contribution
tfl = t_lens(k,f,ys);
%impulse response of space between lens and image planes
hfr1 = h_fr_air(k,di,ys);
HFR1 = (1/N)*fft(hfr1);
HFR1 = fftshift(HFR1);
%transformation from source plane to lens plane
Elens = N*ifft(Us_FT.*HFR);
%transformation through the lens
Elens = Elens.*tfl;
Elens_FT = (1/N)*fft(Elens);
%transformation from lens plane to image plane
Eo_FT = Elens_FT.*HFR1;
%transformation from angular space to Cartesian space
Eo = N*ifft(Eo_FT);
Eo = fftshift(Eo);

**************************

function h = h_fr_air(k,d,y)
% Fresnel approximation of the open air impulse response
%
% k – wavenumber, 1/mm
% d – distance, mm
% y – shift distance from the lens axis, mm
```

```
format long g
h = k.*exp(j*k*d).*exp( 0.5.*j.*k.*y.^2./d )./(2*pi*j*d);

**************************

function U = t_lens(k,f,y)
% thin lens approximation
%
% k – wavenumber, 1/mm
% f – focal length of the lens, mm
% y – shift distance from the lens axis, mm

format long g
U = exp( -0.5.*j.*k.*y.^2./f );
```

Bibliography

[1] K. Yee, “Numerical Solution of Initial Boundary Value Problems Involving Maxwell's Equations in Isotropic Media”, *IEEE Trans. on Antennas and Propagation*, Vol.14, May 1966.

[2] A. Taflove, S. C. Hagness, *Computational Electrodynamics: The Finite-Difference Time-Domain Method*, (Artech House Publishers, 2005).

[3] G. Mur, “Absorbing Boundary Conditions for the Finite-Difference Approximation of the Time-Domain Electromagnetic-Field Equations,” *IEEE Trans. Electromagnetic Compatibility*, vol. EMC-23, no.4, pp. 377-382, Nov. 1981.

[4] J. P. Berenger, “A perfectly matched layer for the absorption of electromagnetic waves,” *J. Comput. Phys.*, vol. 114, no. 2, pp. 185-200, Oct. 1994.

[5] K. K. Mei., J. Fana. "Superabsorption - A Method to Improve Absorbing Boundary Conditions," *IEEE Trans. Antennas & Propagat.*, vol. AP-40, pp. 1001-1010, Sept. 1992.

[6] W. K. Gwarek, T. Morawski, C. Mroczkowski, “Application of the FDTD Method to the Analysis of the Circuits Described by the Two-Dimensional Vector Wave Equation,” *IEEE Trans. Microwave Theory Tech.*, vol. 41, no. 2, pp. 311-316, Feb. 1993.

[7] W. K. Gwarek, M. Celuch-Marcysiak, “A differential method of reflection coefficient extraction from FD-TD simulations,” *IEEE MicrowaveGuided Wave Lett.*, vol. 6, pp. 215–217, May 1996.

[8] A. Kreczkowski, M. Mrozowski, “Multimode analysis of waveguide discontinuities using the concept of generalized scattering matrix and power waves,” *Proc. 13th Int. MIKON Conf.*, Wroclaw, Poland, May 2000, pp. 569–572.

[9] D. E. Merewether, R. Fisher, F. W. Smith, “On Implementing a Numeric Huygen’s Source Scheme in a Finite Difference Program to Illuminate Scattering Bodies”, *IEEE Trans. Nuclear Science*, vol. 27, no. 6, Dec. 1980, pp.1829-1833.

[10] L-C. Ma, R. Mittra, “Implementation of Gaussian Beam Sources in FDTD for Scattering Problems”, *IEEE Trans. Electromagnetic Compatibility*, vol. EMC-24, no. 4, Nov. 1982, pp.397-405.

[11] I. R. Capoglu, A. Taflove, V. Backman, “Generation of an incident focused light pulse in FDTD,” *Optics Express*, vol. 16, no. 23, pp. 19208–19220, Nov. 2008.

[12] K. Umashankar, A. Taflove, “A Novel Method to Analyze Electromagnetic Scattering of Complex Objects”, *IEEE Trans. Electromagnetic Compatibility*, vol. EMC-24, no. 4, Nov. 1982, pp.397-405.

[13] R. J. Luebbers, K. S. Kunz, M. Schneider, F. Hunsberger, “A Finite-Difference Time-Domain Near Zone to Far Zone Transformation”, *IEEE Trans. Antennas and Propagation*, vol. 39, no. 4, April 1991, pp.429-433.

[14] W. K. Gwarek, “Analysis of an arbitrarily-shaped planar circuit - a time-domain approach”, invited paper, *IEEE Trans. Microwave Theory Tech.*, vol. MTT-33, No.10, Oct.1985, pp.1067-1072.

[15] M. Celuch-Marcysiak, W. K. Gwarek, “Implicit incorporation of nonlinear elements for unconditionally stable FDTD analysis at coarse time-steps”, *IEEE MTT-S International*, vol. 3, June 1996, pp.1381-1384.

[16] M. Fujii, M. Tahara, I. Sakagami, W. Freude, P. Russer, “High-Order FDTD and Auxiliary Differential Equation Formulation of Optical Pulse Propagation in 2-D Kerr and Raman Nonlinear Dispersive Media”, *IEEE Journal of Quantum Electronics*, vol. 40, No.2, Feb.2004, pp.175-182.

[17] M. Celuch, “A method of analysis of planar circuits incorporating nonlinear elements,” M.Sc. Thesis, Warsaw University of Technology, 1988.

[18] F. Kung, H. T. Chuah, “A study on the stability of bipolar-junction-transistor formulation in finite-difference time-domain framework”, *IEEE Trans. Microwave Theory Tech.*, vol. 53, No.4, April 2005, pp.1189-1196.

[19] A. Moryc, “Finite difference time domain electromagnetic modeling applied to dispersive and anisotropic media,” Ph.D. Thesis, Institute of Radioelectronics, Warsaw University of Technology, 2006.

[20] M. Celuch-Marcysiak, W. K. Gwarek, “Effective time domain analysis of periodic structures,” in *Proc. 23rd Euro. Microwave Conf.*, pp. 293-295, Madrid, 1993.

[21] W. L. Ko, R. Mittra, “Implementation of Floquet boundary condition in FDTD for FSS analysis,” in *IEEE APS Int. Symp. Dig.*, vol. 1, pp. 14-17, July 1993.

[22] M. Celuch-Marcysiak, W. K. Gwarek, “Spatially looped algorithms for time-domain analysis of periodic structures”, *IEEE Trans. Microwave Theory Tech.*, vol. MTT-43, No. 4, April 1995, pp. 860-865.

[23] M. E. Veysoglu, R. T. Shin, J. A. Kong, “A Finite-Difference Time-Domain Analysis of Wave Scattering from Periodic Surfaces: Oblique Incidence Case,” *J. of Electromagnetic Waves and Applications*, Vol. 7, No. 12, pp. 1595-1607, 1993.

[24] W. K. Gwarek, “Analysis of Arbitrarily Shaped Two-Dimensional Microwave Circuits by Finite-Difference Time-Domain Method”, *IEEE Trans. Microwave Theory Tech.*, vol. 36, No.4, April 1988, pp.738-744.

[25] M. Celuch-Marcysiak, W. K. Gwarek, “On the nature of solutions produced by finite difference schemes in time domain”, *International Journal of Numerical Modelling – Electronic Networks, Devices and Fields*, vol. 12, no. 1/2, January-April 1999, pp.23-40.

[26] W. L. Ko, R. Mittra, “A Combination of FD-TD and Prony’s Methods for Analyzing Microwave Integrated Circuits”, *IEEE Trans. Microwave Theory Tech.*, vol. 39, No. 12, Dec. 1991, pp.2176-2181.

[27] M. Mrozowski, “Criteria for building Prony models for time domain CAD”, *Antennas and Propagat. Society Intl. Symp.*, vol. 4, June 1998, pp.2306-2309.

[28] M. Okoniewski, E. Okoniewska, M. A. Stuchly, “Three-dimensional subgridding algorithm for FDTD”, *IEEE Trans. Antennas and Propagation*, vol. 45, no. 3, March 1997, pp.422-429.

[29] C. Mroczkowski, W. K. Gwarek, “Microwave circuits described by two-dimensional vector wave equation and their analysis by FD-TD method”, *Proc. 21st European Microwave Conf.*, Stuttgart, Sept. 1991, pp. 199-204.

[30] M. Celuch-Marcysiak, “A Generalized Approach to the FDTD and TLM Algorithms Applied to the Modelling of Microwave Circuits”, Ph.D. Thesis, Institute of Radioelectronics, Warsaw University of Technology, 1995.

[31] M. Celuch-Marcysiak, W. K. Gwarek, “On the Aspects of Selecting the Symmetrical Condensed Node or the Expanded Node Modelling for Electromagnetic Simulations”, XXII Eur. Microwave Conf., Helsinki 1992.

[32] W. K. Gwarek, “Application of time domain methods to calculation of dispersion characteristics of transmission lines of arbitrary cross-section”, *European Conference on Numerical Methods in Electromagnetics NUMELEC’92*, Grenoble, France, March 1992.

[33] A. Asi, L. Shafai, “Dispersion analysis of anisotropic inhomogeneous waveguides using compact 2D-FDTD”, *Electronics Letters*, vol.28, No.15, July 1992, pp.1451-1452.

[34] F. Arndt, V. J. Brankovic, D. V. Krupezevic, “An improved FD-TD full wave analysis for arbitrary guiding structures using a two-dimensional mesh”, *IEEE MTT Symp. Digest*, Albuquerque, 1992.

[35] S. Xiao, R. Vahldieck, H. Jin, "Full-wave analysis of guided wave structures using a novel 2-D FDTD," *IEEE Microwave Guided Wave Lett.*, vol. 2, No. 5, pp. 165-167, May 1992.

[36] W. Tsay, D. Pozar, "Application of the FDTD Technique to Periodic Problems in Scattering and Radiation," *IEEE Microwave Guided Wave Lett.*, vol. 3, No. 8, pp. 250-252, Aug. 1993.

[37] Y-C. A. Kao, R. G. Atkins, "A finite difference-time domain approach for frequency selective surfaces at oblique incidence," in *Proc. IEEE AP-S Int. Symp.*, vol. 2, pp. 1432–1435, Baltimore, MD, July 1996.

[38] Y-C. A. Kao, "Finite-Difference Time-Domain Modeling of Oblique Incidence Scattering from Periodic Structures," MSc Thesis, MIT, April 1997.

[39] J. Roden, S. Gedney, M. Kesler, J. Maloney, P. Harms, "Time-Domain Analysis of Periodic Structures at Oblique Incidence: Orthogonal and Nonorthogonal FDTD Implementations," *IEEE Trans. Microwave Theory Tech.*, vol. 46, no. 4, pp. 420-427, April 1998.

[40] M. Kesler, J. Maloney, P. Harms, J. Roden, "Incorporating Lossy Materials and PML into the Split-Field Update FDTD Method," *Proc.1998 IEEE-AP-S International Symp.*, vol. 1, pp. 554-557, June 1998.

[41] A. Aminian, Y. Rahmat-Samii, "Spectral FDTD: A Novel Technique for the Analysis of Oblique Incident Plane Wave on Periodic Structures," *IEEE Trans. Antenna Propagat.*, vol.54, no.6, pp.1818-1825, June 2006.

[42] R. Qiang, J. Chen, "ASM-FDTD: A Technique for Calculating the Field of a Finite Source in the Presence of an Infinite Periodic Artificial Material," *IEEE Microwave and Wireless Component Letters*, vol.17, no.4, pp.271-273, April 2007.

[43] R. Qiang, J. Chen, F. Yang "FDTD Modeling of Finite Electromagnetic Source over Periodic Structure via a Spectral Expansion Method," *IEEE Microwave Symp. MTT-S*, pp.887-890, June 2007.

[44] B. A. Munk, G. A. Burrell, "Plane-wave expansion for arrays of arbitrarily oriented piecewise linear elements and its application in determining the impedance of a single linear antenna in a lossy half-space," *IEEE Trans. Antennas Propagat.*, vol. 27, pp.331–343, May 1979.

[45] M. Wegener, Lecture on *Photonic crystal and Metamaterials*, available on http://www.aph.uni-karlsruhe.de/wegener/

[46] S. G. Johnson, J. D. Joannopoulos, “Block-iterative frequency-domain methods for Maxwell’s equations in a planewave basis,” *Opt. Express*, vol. 8, no. 3, pp.173–190, Jan. 2001.

[47] Z. Lu, S. Shi, C. A. Schuetz, J. A. Murakowski, D. W. Prather, “Three-dimensional photonic crystal flat lens by full 3D negative refraction,” *Opt. Express*, vol. 13, no. 15, pp.5592–5599, July 2005.

[48] QuickWave-3D, QWED Sp. z o.o. Available: http://www.qwed.com.pl.

[49] P. Leray, S. Cheng, D. Kandel, B. Dinu, M. Vasconi, B. Salski, “Diffraction Based Overlay Metrology: Accuracy and Performance on Front end Stack,” *SPIE 2008*, Vol. 6922.

[50] B. A. Monk, "Frequency Selective Surfaces, Theory and Design," Wiley-Interscience, 2000.

[51] L. E. R. Petersson, J.-M. Jin, “A Two-Dimensional Time-Domain Finite Element Formulation for Periodic Structures,” *IEEE Microwave Guided Wave Lett.*, vol. 53, No. 4, pp. 1480-1488, April 2005.

[52] W. Lee, F. L. Degertekin, “Rigorous coupled-wave analysis for multilayered grating structures,” *Proc. of SPIE*, vol. 4987, pp. 264-273, 2003.

[53] Y. Cai, C. Mias, ”Fast Finite Element Time Domain – Floquet Modal Absorbing Boundary Condition Modelling of Periodic Structures Using Recursive Convolution,” *IEEE Trans. Antenna Propagat.*, vol.55, no.9, pp.2550-2558, Sept. 2007.

[54] B. Salski, M. Celuch, W. Gwarek, "Enhancements to FDTD modeling for optical metrology applications", *SPIE Optical metrology - 18th Intl. Congress on Photonics in Europe*, Munich, June 2007.

[55] *private correspondence* with KLA-Tencor, Israel.

[56] E. D. Palik, “Handbook of Optical Constants of Solids”, *Academic Press*, 1985.

[57] http://www.st.com/stonline/company/projects/socot/index.htm

[58] B. Salski, M. Celuch, W. K. Gwarek, "Evaluation of FDTD regimes for scattering from periodic structures", 23rd Annual Review of Progress in Applied Computational Electromagnetics, Verona, March 2007, pp.1815-1822.

[59] B. Salski, W. K. Gwarek, M. Celuch, "Comparison of FDTD excitation models for scatterometry of periodic reticles", 2007 IEEE AP-S Intl. Symp., Honolulu, June 2007, pp. 1673-1676.

[60] B. Salski, M. Celuch, W. K. Gwarek, "Review of Complex Looped FDTD and its new applications", 24th Annual Review of Progress in Applied Computational Electromagnetics, Niagara Falls, March - April 2008.

[61] R. Collin, "Field Theory Of Guided Waves", *McGraw-Hill Book Company, Inc.*, 1960.

[62] W. K. Gwarek, M. Celuch-Marcysiak, "Wide-Band S-Parameter Extraction From FD-TD Simulations for Propagating and Evanescent Modes in Inhomogeneous Guides," *IEEE Trans. Microwave Theory Tech.*, vol. 51, no. 8, pp. 1920-1928, Aug. 2003.

[63] S. Ramo, J. R. Whinnery, T. Van Duzer, "Fields and Waves in Communication Electronics", 3rd ed., Toronto, *John Wiley & Sons*, 1994.

[64] B. Salski, M. Celuch, W. Gwarek, "FDTD modelling of finite spot scatterometry", *17th International Conference on Microwaves, Radar and Wireless Communications: MIKON 2008*, Wroclaw, May 2008.

[65] J. Goodman, "Introduction to Fourier Optics", *Roberts & Company Publishers*, 2004.

[66] L. Sevgi, "Complex Electromagnetic Problems and Numerical Simulation Approaches", New York, *IEEE Press/John Wiley & Sons*, 2003.

[67] K. Sawada, M. Sakai, Y. Kahashi, T. Saiki and H. Nakamura, "FDTD modeling of a polarization near-field scanning optical microscope", *Journal of Plasma Physics*, vol.72, 2006, pp.1019-1023.

[68] B. Salski and W. K. Gwarek, "Hybrid FDTD-Fresnel Modeling of Microscope Imaging", International Conference on *Recent Advances in Microwave Theory and Applications* MICROWAVE-08 in Jaipur, Rajastan, India, November 21-24, 2008.

[69] B. Salski and W. K. Gwarek, "Hybrid FDTD-Fresnel Modeling of the Scanning Confocal Microscopy ", SPIE Scanning Microscopy 2009, Monterey CA, 4-7 May 2009.

[70] B. Salski and W. K. Gwarek, "Hybrid finite-difference time-domain Fresnel modeling of microscopy imaging", *Applied Optics*, vol.48, Issue 11, pp.2133-2138, April 2009.

[71] O. K. Ersoy, "Diffraction, Fourier Optics and Imaging", *John Wiley & Sons*, 2007.

[72] M. Born, E. Wolf, "Principles of Optics", *Cambridge University Press*, 1999.

[73] C. A. Balanis, "Antenna Theory, Analysis and Design", *John Wiley & Sons*, pp. 620, 1997.

[74] M. M. Ney, A. M. Smith and S. S. Stuchly, "A solution of Electromagnetic Imaging Using Pseudoinverse Transformation," *IEEE Trans. Medical Imaging.*, vol. MI-3, no.4, pp. 155-162, Dec. 1984.

[75] J. L. Hollmann, A. K. Dunn and C. A. DiMarzio, “Computational microscopy in embryo imaging,” *Optics Letters*, vol. 29, no.19, pp. 2267-2269, Oct. 2004.

[76] Website: planetquest1.jpl.nasa.gov/TPFDarwinConf/proceedings/posters/p076.pdf.

[77] K. Choi, J. W. M. Chon, M. Gu and B. Lee, “Characterization of a subwavelength-scale 3D void structure using the FDTD-based confocal laser scanning microscopic image mapping technique,” *Optics Express*, vol. 15, no.17, pp. 10767-10781, Aug. 2007.

[78] Website: http://www.microscopyu.com/articles/formulas/formulasconjugate.html.

[79] Website: http://www.hopkinsmedicine.org/micfac/refman/Zeiss/LSM510Meta/ Principles_of_Confocal_Microscopy.pdf.

[80] C. Mroczkowski, “Vector two-dimensional microwave structures and their analysis by the FD-TD method,” Ph.D. Thesis, Institute of Radioelectronics, Warsaw University of Technology, 1995.

[81] C. Mroczkowski, M. Celuch-Marcysiak, W. K. Gwarek, “Joint Application of Superabsorption and Near-To-Far Field Transform to FDTD Analysis of Axisymmetrical Antennas,” European Microwave Conference, 1994.

[82] C. Mroczkowski, W. K. Gwarek, “Effective Analysis of Axisymmetrical Dielectric Rod Antennas Using Vector 2-D FD-TD Method,” IEEE MTT Symp. Digest, June 1994.

[83] B. Salski, W. Gwarek, ”Near-to-Near Transformation in Axisymmetrical Antenna Problems,” IEEE Trans. Antenna Propagat., vol.55, no.8, pp.2157-2162, Aug. 2007.

[84] C. Mroczkowski, M. Celuch-Marcysiak, W. K. Gwarek, "Joint application of superabsorption and near-to-far field transform to FDTD analysis of axisymmetrical antennas", Proc. 24th European Microwave Conf., Cannes, Sept. 1994, pp.899-904.

[85] C. Mroczkowski, W. K. Gwarek, “Effective Analysis of Axisymmetrical Dielectric Rod Antennas Using Vector 2-D FD-TD Method,” IEEE Antennas & Propagat. Symposium, vol. 3, pp. 1794-1797, June 1994.

[86] S. D. Gedney, R. Mittra, “The Use of the FFT for the Efficient Solution of the Problem of Electromagnetic Scattering by a Body of Revolution,” IEEE Trans. Antennas and Propagat., vol.38, no.3, pp. 313-322, 1990.

[87] D. H. Werner, “An exact integration procedure for vector potentials of thin circular loop antennas,” *IEEE Trans. Antennas Propagat.*, vol. 44, pp. 157-165, Feb. 1996.

[88] D. H. Werner, "A method of moments approach for the efficient and accurate modeling of moderately thick cylindrical wire antennas," *IEEE Trans. Antennas Propagat.*, vol. 46, pp. 373-382, 1998.

[89] L. W. Li, M. S. Leong, P. S. Kooi, T. S. Yeo "Exact solutions of electromagnetic fields in both near and far zones radiated by thin circular-loop antennas: A general representation," *IEEE Trans. Antennas Propagat.*, vol. 45, pp. 1741-1748, Dec. 1997.